Kinetic Simulation of Nonlinear Kink Instabilities

E. G. Zaidman

Institute for Fusion Studies
The University of Texas at Austin
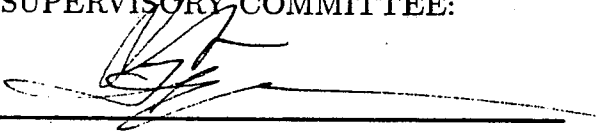Austin, Texas 78712-1060

August 1986

Kinetic Simulation of Nonlinear Kink Instabilities

E.G. Zaidman

The history of the building of a base of understanding in plasma physics may be examined by categorizing our efforts into the divisions of linear or nonlinear physics, and by the use of fluid (usually magnetohydrodynamic) or kinetic models as illustrated in Table 1.1, which summarizes when the major thrust of effort took place. Our basic understanding of the linear physics using a fluid model arose primarily in the 50's with the efforts connected through Project Sherwood and on into the 60's. The fluid model has since been extended into the nonlinear regime in the 70's and 80's. A recent article by R.B. White reviews both the linear and nonlinear theory of MHD modes including resistive effects. Accompanying the analytical advances were advances in computer simulation techniques with applications to nonlinear evolution of the resistive mode and using sophisticated techniques. For some phenomena the fluid treatment remains inadequate. The consideration of the velocity distribution function for each species as well as transport phenomena leads to treatment of the plasma in a kinetic model. The kinetic model in the linear regime developed throughout the 60's to the 80's. The inclusion of nonlinear effects into the kinetic model is only recently appearing in the theoretical picture. The technique of particle simulation enables the study of nonlinear effects in a kinetic model in detail.

KINETIC SIMULATION OF NONLINEAR KINK INSTABILITIES

APPROVED BY SUPERVISORY COMMITTEE:

Swadesh M Mahajan

A D Vajeltine

Clark R. Wilson

Daniel C. Barnes

Wendell Horton, Jr.

KINETIC SIMULATION OF NONLINEAR KINK INSTABILITIES

by

ERNEST GARY ZAIDMAN, B.S., M.A.

DISSERTATION

Presented to the Faculty of the Graduate School of

The University of Texas at Austin

in Partial Fulfillment

of the Requirements

for the Degree of

DOCTOR OF PHILOSOPHY

THE UNIVERSITY OF TEXAS AT AUSTIN

August, 1986

ACKNOWLEDGEMENTS

TABLE OF CONTENTS

Chapter

Page

LIST OF FIGURES

CHAPTER 1.
INTRODUCTION

The history of the building of a base of understanding in plasma physics may be examined by categorizing our efforts into the divisions of linear or nonlinear physics and by the use of fluid (usually magnetohydrodynamic) or kinetic models as illustrated in Table 1.1 which summarizes when the major thrust of effort took place. Our basic understanding of the linear physics using a fluid model arose primarily in the 50's with the efforts connected through Project Sherwood[1] and on into the 60's. The fluid model has since been extended into the nonlinear regime in the 70's and 80's. A recent article by R.B. White[2] reviews both the linear and nonlinear theory of MHD modes including resistive effects. Accompanying the analytical advances were advances in computer simulation techniques with applications to nonlinear evolution of the resistive mode[3] and using sophisticated techniques[4]. For some phenomena the fluid treatment remains inadequate. The consideration of the velocity distribution function for each species as well as transport phenomena leads to treatment of the plasma in a kinetic model. The kinetic model in the linear regime developed throughout the 60's to 80's. The inclusion of nonlinear effects into the kinetic model is only recently appearing in the theoretical picture[5]. The technique of particle simulation[6] enables the study of nonlinear effects in a kinetic model in detail.

The tools of particle simulation of plasmas have become more sophisticated over the past twenty-five years[6] enabling more complex physical processes to be studied. The necessity for these complications in the simulation process occurs because of the multiple spatial and temporal scales on which plasma phenomena occur. The lack of sufficient speed and memory to economically simulate large scale, low frequency phenomena, such as

	LINEAR PHYSICS	NONLINEAR PHYSICS
FLUID (MHD) MODEL	50'S - 60'S	70'S - 80'S
KINETIC MODEL	60'S - 80'S	80'S -

kink modes, using realistic models forces us to examine techniques which avoid direct confrontation with these obstacles. One such approach, that of a three- dimensional magnetoinductive particle code with guiding center electrons is described herein and its application to kink and twist-kink modes is presented.

One of the fastest time scales associated with a plasma is that due to the gyromotion of the electrons in a magnetic feld. A guiding center model may be appropriately employed when the motion consists of a fast oscillatory motion plus another slower motion. The electron motion may then be separated into a gyromotion with characteristic frequency, Ω_c, plus a slower $\mathbf{E} \times \mathbf{B}$ drift of the guiding center[7], or center of the gyro-orbit and other drifts including higher order motions. However, one crucial drift is the $\mathbf{E} \times \mathbf{B}$ drift which retains the self consistency. (The other is the polarization drift in the higher order, which is not discussed in the present work.) Such a model was developed as a $2\frac{1}{2}$-dimensional electrostatic particle code in a slab geometry by W. W. Lee and H. Okuda[8].

The inclusion of electromagnetic effects in addition to electrostatic introduces a wider range of processes available to more realistically simulate a plasma system. In particular, the inclusion of light wave propagation introduces a fast time scale. This time scale which must now be included when Maxwell's equations appear is of the temporal scale, $\Delta t \approx (kc)^{-1}$, where k is the wavenumber describing the spatial scale used and c is the speed of light. Since the speed of light is so large while the required spatial scale length is so small, the resolution in time must be quite small. Thus even though the physics we may wish to study is on a large time scale, the simulation becomes uneconomical or impossible to do with an electromagnetic model. The elimination of light wave propagation in the plasma model could

then greatly extend the range of the tools of particle simulation. This can be done by dropping the transverse displacement current term in Ampere's equation. Such a magnetoinductive or Darwin[9] model can provide greater computational efficiency for the study of subluminous waves in plasmas. Implementations of this model have been done by Nielson and Lewis[10] and by Busnardo-Neto, et el.[11]

Plasma phenomena are often simulated by models which only utilize one or two spatial dimensions. As we look at more complex systems, the inclusion of all three dimensions becomes important. The inclusion of the additional degree of freedom provided by this inclusion enables more realistic modelling of plasma configurations. For some studies the full three dimensions are not only desired but necessary, for example, the nonlinear kink modes. The straightforward extension of two dimensional models by just doing the same process in the third direction as done in the first two makes excessive if not impossible demands on the computational facilities. In a magnetied plasma, generally the dynamics along one direction parallel to the magnetic field and that along the other two directions are quite distinct. For example, the typical wavelengths in the parallel direction and in the perpendicular directions are distictively different. For the typical gridded models which are extended into three dimensions, a stretching of the grid in the third direction along with a higher order particle-grid interpolation scheme becomes necessary. Another approach is an eigenfunction expansion in the third direction as in a spectral code. This hybrid[12] allows very disparate length differences between the two gridden dimensions to the third dimension. For a small number of modes, say $N < 20$, this code may be more efficient to use than a fully gridded model.

Combining the two techniques of the magnetoinductive and

guiding center electron approximations in a simulation code has been applied to the long time scale process of Alfvén wave heating by Geary et. al.[13] The inclusion of a third dimension into this model via mode expansion allows the study of long time scale processes in inherently three dimensional systems. Such a model is described in chapter two. Examples of such processes are tandem mirrors and coronal loops.

The impulsive phase of some solar flares occur on a time scale much faster than the typical resistive instabilities, explosively releasing energy stored in the lower corona. Direct observations of emitted soft x-rays[14] show the existence of multiple coronal loops in the active regions. These loops may carry plasma currents. It was noted in 1964[15,16] that the high intensity and short life of the impulsive solar flare indicates that it is caused by a nonlinear instability. The processes of reconnection of magnetic field lines is believed to take place due to a small but finite resistivity. In order to rapidly convert magnetic energy into kinetic by a substantial amount that is accountable for the observed flare phenomena, it seems necessary that the bulk of the magnetic energy has to participate in the conversion process: the resistive heating at the x-point alone is too meager. This is because the available magnetic energy at the x-point is small by itself. On the other hand, the ideal MHD instabilities such as the kink instability and the coalescense instability are the processes that involve the bulk current redistribution on the order of the Alfvén time scale. Simulation of the tearing and coalescense instabilities presented in chapter three present essentially a two-dimensional picture that still exposes fast reconnection processes. The inclusion of a third dimension allows for the possiblity of kink instabilities which are also discussed in chapter three.

In the preflare stage active regions exhibit photospheric shear

motion along the magnetic neutral line several hours prior to the onset of the flare. The photospheric shear motion induces plasma currents along the potential magnetic field of the sunspots near the active region. As the shear motion proceeds, the current density increases and the current loops move up. A recent computer simulation by Wu[17] suggests that in the modeling of arcade-like preflare stage the current tends to localize. With increasing current density the current constriction takes place toward the center of the loop. If the current density continues to increase further, the poloidal field becomes sufficiently large so that the field line azimuthally rotates more than one revolution within the length of the loop plasma. then the kink modes may develop and induce multiple currents. These intertwining current filaments can coalesce with each other, leaving a current filament with different helicity. Mirror confinement of plasma is one of the oldest concepts in fusion. To overcome the fundamental leakage of plasma from a mirror, the tandem mirror concept was introduced[18,19]. This concept introduces additional magnetic mirrors at the ends of a central mirror cell to electrostatically plug the ends. An ambipolar potential barrier is thus introduced. The axial variation of the potential profile leads to a differential twisting of the plasma column. Poloidal rotation of the plasma in tokamaks also occurs[20]. Although explicit applications have not been sought, twist-kink modes may play a role in plasmas of reverse field pinches, spheromacs, and in the formative stages of tokamaks. A simulation study of the twist-kink mode is presented in chapter four. Chapter five presents conclusions.

CHAPTER 2.

SIMULATION MODEL

2.1 General Remarks

Simulation techniques have enabled us to extend our understanding of physical systems by complementing the knowledge we have gained through analytical and experimental methodologies. In this approach, a computer is programmed with an algorithm based upon a mathematical model describing the physical system. The computer is then instructed to perform numerical experiments utilizing this algorithm. Associated diagnostics can examine in total detail the progress of this experiment. The behavior of plasmas may be fruitfully studied by this approach.

Plasma simulation algorithms may be considered to consist of two groups, particle models and fluid models. A fluid model uses a set of fluid equations to describe the physical system while in a particle model, a large number of charged particles are followed in their self consistent electromagnetic fields. The approach we have utilized is a type of particle model. Particle simulation techniques are reviewed by Hockney and Eastwood[21], Birdsall and Langdon[22], and by Dawson[6] who give a good overview of the particle simulation way of thinking.

Particle simulation techniques have both advantages and limitations. The primary characteristic of particle techniques is that it directly models the many-body system whose distribution function obeys the Liouville equation

$$\frac{\partial F}{\partial t} + \sum_i \left(\frac{\partial F}{\partial \mathbf{x}_i} \cdot \mathbf{v}_i + \frac{\partial F}{\partial \mathbf{v}_i} \cdot \mathbf{a}_i^T \right) = 0 \qquad (2.1)$$

where $\mathbf{v}_i = \dot{\mathbf{x}}_i$ and $\mathbf{a}_i^T$ is the total acceleration acting on the i'th particle. On the other hand, the fluid models deal with quantities, the moments of

a one-body distribution function ,derived by integrating the Liouville equation over all but one particle, thus largely eliminating kinetic effects. Thus we retain more detailed information of the system evolution in the particle simulation. This advantage accompanies disadvantages at the same time. Because of the constraints of finite computational speed and memory, the number of particles which we can follow is limited. The particles interact via the intermediary of the fields which are only defined at a limited number of locations. Accuracy is lost in the interpolation of physical quantities between particle locations and field locations.

An outline of an electrostatic particle simulation is as follows. The initial positions and velocities of the simulation particles are assigned so as to give the desired density and velocity profiles appropriate for the phenomenon to be studied. The time step cycle then begins by interpolation of the particle positions via charge weighting to the grid locations. The potential or electric field is then solved for only on the mesh. The resultant force used to accelerate the particles is interpolated back to the particle location from this gridded representation. The particle velocities can thus be extrapolated forward in time by use of the finite difference form for the force equation. The particles may then be stepped forward to their new positions. The time step cycle is then repeated (perhaps thousands of times) as the simulation plasma evolves.

By following far fewer particles than the actual physical system the particle representation overemphasizes the kinetic or individual aspect of plasmas as compared to the fluid aspects of plasmas. For example, the particle method gives rise to a high level of collisions. The effect of collisions may be decreased by the use of particles which have finite size and can interpenetrate each other. For particle separations larger than the particle size

the interaction force is similar to that of point particles, but as they overlap their interaction force decreases. Since the collective effects are primarily determined by long range forces, collisionless plasma phenomenon may be accurately simulated by relatively few computational particles through this method.

The efficiency of a particle simulation is enhanced by the use of the intermediary of electromagnetic fields defined on a spatial mesh or grid rather than directly calculating interactions between particles. Once the particle quantities are interpolated to a grid, several methods are available to solve for the fields defined on the grid. One of the most efficient and convenient for the grids we use is the Fast Fourier Transform (FFT) technique. In this technique, the spatial differential operations become simply algebraic operations; the overhead cost is in the transform to and from Fourier space.

Particle simulations have other limitations which are harder to ameliorate. The time scale of the physical system which we wish to describe may have much lower frequencies than our computational algorithm can provide economically. The spatial scale of the physical system may not be able to be accomodated within the available memory of the current generation of computers. The simulation technique discussed in this dissertation makes some progress in extending the accessible range of temporal and spatial scales we can study in the particle simulation.

In a particle simulation model the time scales which can be modeled are constrained by the maximum time step for which the system is numerically stable. For the typical electromagnetic codes with a relativistic Lorentz particle motion and the full set of Maxwell's equations, this time step is determined by the electron plasma frequency via, $\omega_{pe}\Delta t < 1$, the electron cyclotron frequency via, $\Omega_e \Delta t < 1$, and by light propagation across the grid

via $kc\Delta t < 1$, where k is the relevant wavenumber. For phenomenon with frequencies in the range of typical Alfvén waves, this restriction makes it uneconomical as well as too "noisy" for study with such a code. The typical particle simulation code are constrained in spatial scales by the combination of the limited number of grid points which can be contained in memory and by the need to satisfy the stability condition, $k_{max}v_{max}\Delta t < 1$ so that the particle moves less than one grid spacing per time step.

2.2 The Hybrid Spatial Model

The spatial scales in plasmas with a magnetic field can vary greatly between phenomenon along the field and perpendicular to it. The important collective oscillations along the field lines are of comparatively longer wavelength. This indicates that a hybrid model, which uses the standard grid methods perpendicular to the magnetic field combined with a spectral expansion method which uses only the long wavelength oscillations along the magnetic field, is appropriate to many topics of current interest because of its accuracy and numerical stability. An electrostatic model of this type has been used by Cheng and Okuda[12] to study drift instabilities in cylindrical and toroidal models.

Let us consider an electrostatic rectangular cylindrical model. The finite size particle is given a Gaussian shape factor

$$S\left(\mathbf{x} - \mathbf{x}_j\right) = \frac{1}{(2\pi)^{3/2}a_x a_y a_z} exp\left[-\left(\frac{(x - x_j)^2}{2a_x{}^2} + \frac{(y - y_j)^2}{2a_y{}^2} + \frac{(z - z_j)^2}{2a_z{}^2}\right)\right]$$

(2.2)

where (x_j, y_j, z_j) is the particle center location and $a_x, a_y,$ and a_z are the characteristic length scales for the particle shape. The charge density is therefore

given by

$$\rho(x, y, z) = \sum_j q_j S(\mathbf{x} - \mathbf{x}_j). \qquad (2.3)$$

The normal mode expansion is applied to both the charge density and the longitudinal electric field.

$$\rho(x, y, z) = \sum_{n=-N}^{N} \rho_n(x, y) exp\left(\frac{i2\pi z n}{L_z}\right) \qquad (2.4)$$

and

$$\mathbf{E}_L(x, y, z) = \sum_{n=-N}^{N} \mathbf{E}_{Ln}(x, y) exp\left(\frac{i2\pi z n}{L_z}\right) \qquad (2.5)$$

for a system length in the z direction of L_z. Since the number of modes required is typically small ($N < 10$), the computer memory required for the simulation is less than that required for a typical three dimensional grid type of code. Another advantage is that the mode number expression is readily interpreted by theory.

Poisson's equation,

$$\nabla \cdot \mathbf{E}_L = 4\pi\rho, \qquad (2.6)$$

may be solved by a superposition of solutions for each mode number, n. The method of solution is, for each n, to first Fourier transform the two dimension grid using standard FFT methods. The solution for each $\mathbf{E}_{Ln}(\mathbf{k})$ is obtained. The inverse transform is then applied. The field may then be interpolated to the particle position by summing over the contributions of each mode, n.

The necessity of interpolating the charge of the finite size particles from each $\mathbf{x}_j$ to a regular lattice, is accomplished by a Taylor expansion on the two dimensional grid about the nearest grid point,

$$\sum_j q_j S(\mathbf{x} - \mathbf{x}_j) exp(-ik_z z_j)$$

$$= \sum_j q_j \left[S(\mathbf{x} - \mathbf{x}_g) + \Delta \mathbf{x}_g \cdot \nabla_g S(\mathbf{x} - \mathbf{x}_g) \right] exp(-ik_z z_j)$$

$$= M(\mathbf{x}_g) S(\mathbf{x} - \mathbf{x}_g) + \mathbf{D}(\mathbf{x}_g) \cdot \nabla_g S(\mathbf{x} - \mathbf{x}_g), \qquad (2.7)$$

keeping only through the dipole terms. This is often a resonable approximation when finite size particles are used. To obviate the need to perform additional Fourier transforms to evaluate the dipole term, the derivative is replaced by it's finite difference representation,

$$S'(\mathbf{x} - \mathbf{x}_g) = \frac{S(x_{g+1}) - S(x_{g-1}) + S(y_{g+1}) - S(y_{g-1})}{2}. \qquad (2.8)$$

The charge density of the nth mode accumulated to the grid may then be expressed

$$\rho_n(x_g, y_g) = \frac{1}{2\pi a_x a_y} \frac{exp\left(\frac{-a_x^2 k_x^2}{2}\right)}{L_z} S(\mathbf{x} - \mathbf{x}_g)[M(x_g) +$$

$$D_x(x_{g+1}) - D_x(x_{g-1}) + D_y(y_{g+1}) - D_y(y_{g-1})]. \quad (2.9)$$

In Fourier space,

$$\rho_n(k_x, k_y) = \frac{1}{2\pi a_x a_y} \frac{exp\left(\frac{-a_x^2 k_x^2}{2}\right)}{L_z} \frac{S(k_x, k_y)}{L_z} \sum_{l=0}^{N_x - 1} \sum_{m=0}^{N_y - 1} [M(x_g) +$$

$$D_x(x_{g+1}) - D_x(x_{g-1}) + D_y(y_{g+1}) - D_y(y_{g-1})]exp(i\mathbf{k} \cdot \mathbf{x}_g). \quad (2.10)$$

In Fourier space, Poisson's equation,

$$\mathbf{E}_{Ln}(k_x, k_y) = -i \frac{4\pi \mathbf{k}}{k^2} \rho_n(k_x, k_y) \qquad (2.11)$$

determines the longitudinal electric field which is then inverse transformed to give $\mathbf{E}_{Ln}(x, y)$.

Both the finite particle size and the fact that the particle is not necessarily located directly at a grid position must be accounted for again. The force on a finite size particle due to the longitudinal electric field

$$\mathbf{F}(x_j, y_j, z_j) = q_j \int \mathbf{E}_L(x, y, z) S(x - x_j, y - y_j, z - z_j) dx dy dz \qquad (2.12)$$

is known to us on the two dimensional grid

$$\mathbf{F}(x_g, y_g, z_j) = \frac{q_j}{2\pi a_x a_y} \sum_{n=-N}^{N} exp\left(\frac{-k_z^2 a_z^2}{2}\right) exp\left(ik_z z_j\right)$$

$$\int \mathbf{E}_{Ln}(x, y) exp\left[-\frac{(x - x_j)^2}{2a_z^2} + \frac{(y - y_j)^2}{2a_y^2}\right] dx\,dy. \quad (2.13)$$

A multipole expansion about the particle position of the force is similarly kept up to the dipole terms using finite difference approximations for the derivatives to yield

$$\mathbf{F}_n(x_j, y_j) = \mathbf{F}_n(x_g, y_g) + \Delta x_j \frac{\delta}{\delta x} \mathbf{F}_n(x_g, y_g) + \Delta y_j \frac{\delta}{\delta y} \mathbf{F}_n(x_g, y_g). \quad (2.14)$$

The force may be interpolated to the particle position by summing over the contributions of each mode

$$\mathbf{F}(x, y, z) = \sum_{n=-N}^{N} \mathbf{F}_{Ln}(x, y) exp\left(\frac{i2\pi zn}{L_z}\right). \quad (2.15)$$

The equations of motion are then used to advance the particle positions.

2.3 Advancing the Particles

The temporal scales which can be treated in a particle simulation code are limited by the characteristic frequencies of the dynamics included in the model. In a magnetized plasma, the frequency of the electron gyromotion often determines one of the shortest time scales. Since we wish to treat much longer time scales, it is useful to approximate the electron motion in the direction perpendicular to the magnetic field by a guiding center model (Alfvén[7]).

Consider the nonrelativistic Lorentz equation of motion for a charged point particle of species α in a magnetic field

$$m_\alpha \frac{d\mathbf{v}}{dt} = q_\alpha \left(\mathbf{E} + \frac{\mathbf{v}_\alpha}{c} \times \mathbf{B}\right). \quad (2.16)$$

Assuming that the spatial scale lengths of electromagnetic fields felt by the particle are much larger than the the gyroradius ($k\rho_e \ll 1$) and that the frequencies of interest are low in comparison to the gyrofrequency ($\omega/\Omega_e \ll 1$). To lowest order, the electron motion breaks into multiple time scales, the fast gyro motion with characteristic frequency, Ω_e, and the slower $\mathbf{E} \times \mathbf{B}$ drift of the guiding center obtained by time averaging over a cyclotron period. The electron motion is then decoupled into components perpendicular and parallel to $\mathbf{B}$,

$$\frac{d\mathbf{x}_{\perp\,e}}{dt} = \mathbf{v}_{\perp\,e} = c\frac{\mathbf{E} \times \mathbf{B}}{B^2}, \tag{2.17}$$

$$\frac{d\mathbf{x}_{\parallel\,e}}{dt} = \mathbf{v}_{\parallel\,e} = \frac{q}{m}\mathbf{E}_{\parallel}. \tag{2.18}$$

The computational solution of the particle equations of motion are contrasted below for the ions and electrons. The full ion dynamics are kept, thus keeping ion inertial effects required for Alfvén waves. The standard time centered leap frog method[23] is used to approximate equation (2.16).

$$\frac{\mathbf{v}_i^{n+1} - \mathbf{v}_i^n}{\Delta t} = \frac{q_i\mathbf{E}^{n+1/2}}{m_i} + \frac{\mathbf{v}_i^{n+1} + \mathbf{v}_i^n}{2} \times \frac{q_i\mathbf{B}}{m_i}, \tag{2.19}$$

$$\frac{\mathbf{x}_i^{n+3/2} - \mathbf{x}_i^{n+1/2}}{\Delta t} = \mathbf{v}_i^{n+1}, \tag{2.20}$$

where the superscripts indicate the time step at which the quantity is known. Equation (2.19) may be rewritten in a form which displays the cyclotron time scale more explicitly

$$\mathbf{v}_i^{n+1} - \mathbf{v}_i^{n+1} \times \omega_{ci}\frac{\Delta t}{2} = \mathbf{v}_i^n - \mathbf{v}_i^n \times \omega_{ci}\frac{\Delta t}{2} + \frac{q_i\mathbf{E}^{n+1/2}}{m_i}\Delta t, \tag{2.21}$$

or,

$$\mathbf{v}_i^{n+1} = \mathbf{v}_i^n \cdot \mathbf{R}\left(\omega_{ci}\Delta t\right) + \frac{q_i\mathbf{E}^{n+1/2}}{m_i}\Delta t \cdot \mathbf{R}\left(\omega_{ci}\frac{\Delta t}{2}\right). \tag{2.22}$$

This indicates that the new velocity is obtained by rotating the old velocity through an angle, $(\omega_{ci}\Delta t)$, around $\mathbf{B}$, and adding the velocity change due to $\mathbf{E}$ rotated through $(\omega_{ci}\frac{\Delta t}{2})$. The new ion position can then be advanced,

$$\frac{\mathbf{x}_i^{n+3/2} - \mathbf{x}_i^{n+1/2}}{\Delta t} = \mathbf{v}_i^{n+1}. \tag{2.23}$$

The electron guiding center motion parallel to $\mathbf{B}$ may also be advanced by the leapfrog technique

$$\frac{\mathbf{v}_e^{n+1} - \mathbf{v}_e^n}{\Delta t} = \frac{q_e \mathbf{E}^{n+1/2}}{m_e}. \tag{2.24}$$

If a leap frog is attempted for the perpendicular direction,

$$\frac{\mathbf{x}_{\perp e}^{n+3/2} - \mathbf{x}_{\perp e}^{n+1/2}}{\Delta t} = \mathbf{v}_{\perp e}^{n+1} = c\frac{\mathbf{E}_\perp\left(\mathbf{x}^{n+1/2}\right) \times \mathbf{B}}{B^2}, \tag{2.25}$$

a numerical instability occurs due to the lack of time centering. A different technique is required to push $\mathbf{x}_\perp$, a predictor-corrector method is used. For an equation of the form

$$\frac{d\mathbf{x}_\perp}{dt} = \Gamma(t, \mathbf{x}_\perp), \tag{2.26}$$

the simplest form of the predictor-corrector can be expressed as

$$\mathbf{x}_{\perp\ pred}^{n+1} = \mathbf{x}_\perp^n + \Delta t \Gamma^n, \tag{2.27}$$

$$\mathbf{x}_{\perp\ corr}^{n+1} = \frac{1}{2}\left[\mathbf{x}_{\perp\ pred}^{n+1} + \mathbf{x}_\perp^n\right]. \tag{2.28}$$

The disadvantage of this technique is that it requires the field equations to be solved twice per time step. On the other hand, however, the time scale of Ω_e is eliminated as a restriction on the size of the time step.

2.4 Magnetoinductive Model

The magnetoinductive model uses Darwin's approximation for Maxwell's equations which neglects the transverse component of the displacement current. To obtain a Lagrangian description of a field-particle system as a function of instantaneous velocities and coordinates (as required in the conventional formalism), Darwin[24] neglected retardation effects. This has the effect of removing radiation from consideration in the system.

Maxwell's equations may be written in the form

$$\nabla \times \mathbf{E} = -\frac{1}{c}\frac{\partial \mathbf{B}}{\partial t} \qquad (2.29)$$

$$\nabla \times \mathbf{B} = \frac{4\pi}{c}\mathbf{J} + \frac{1}{c}\frac{\partial \mathbf{E}}{\partial t} \qquad (2.30)$$

$$\nabla \cdot \mathbf{E} = 4\pi\rho \qquad (2.31)$$

$$\nabla \cdot \mathbf{B} = 0. \qquad (2.32)$$

Let L denote the curl-free (longitudinal) and T denote the divergence-free (transverse) components. Equation (2.30) may then be written

$$\nabla \times \mathbf{B} = \frac{4\pi}{c}\mathbf{J}_T + \frac{1}{c}\frac{\partial \mathbf{E}_T}{\partial t} \qquad (Ampere's\ law)(2.33)$$

$$0 = 4\pi\mathbf{J}_L + \frac{1}{c}\frac{\partial \mathbf{E}_L}{\partial t} \qquad (conservation\ of\ charge)(2.34)$$

The neglect of $\partial \mathbf{E}_T/\partial t$ in Ampere's law

$$\nabla \times \mathbf{B} = \frac{4\pi}{c}\mathbf{J}_T \qquad (2.35)$$

removes the explicit time dependent particle-field coupling and thus removes retardation and radiation effects. The explicit time dependent field-field coupling of Faraday's law is kept and inductive effects are therefore retained. Thus the model is denoted as magnetoinductive.

The modification by neglect of this one term in Maxwell's equations alters the numerical form of the equation set from hyperbolic to elliptic. The time derivatives in the full set of Maxwell's equations

$$\frac{\partial \mathbf{E}}{\partial t} = c\nabla \times \mathbf{B} - 4\pi\mathbf{J} \tag{2.36}$$

$$\frac{\partial \mathbf{B}}{\partial t} = -c\nabla \times \mathbf{E} \tag{2.37}$$

are readily advanced in time in a time-centered fashion. Neglecting $\partial \mathbf{E}_T/\partial t$ removes the symmetry and thus the stability due to the time centeredness. The solution uses the coupling of the particles to the fields to determine $\mathbf{E}_T$ in terms of $\partial \mathbf{J}_T/\partial t$ via

$$\nabla^2 \mathbf{E}_T = \frac{4\pi}{c}\frac{\partial \mathbf{J}_T}{\partial t} \tag{2.38}$$

where $\partial \mathbf{J}_T/\partial t$ is expressed only in terms of present values of particle positions and velocities.

The solution of the longitudinal electric field has already been discussed in section 2.2 to illustrate the mode expansion technique. The solution of the magnetic field is obtained from the modified Ampere's law

$$\nabla \times \mathbf{B} = \frac{4\pi}{c}\mathbf{J}_T \tag{2.39}$$

with

$$\mathbf{J}(\mathbf{x}) = \sum_j q_j \mathbf{v}_j S(\mathbf{x} - \mathbf{x}_j). \tag{2.40}$$

The application of the normal mode expansion to the current density and the magnetic field gives the expressions,

$$\mathbf{J}(x,y,z) = \sum_{n=-N}^{N} \mathbf{J}_n(x,y) exp\left(\frac{i2\pi zn}{L_z}\right), \tag{2.41}$$

and

$$\mathbf{B}(x,y,z) = \sum_{n=-N}^{N} \mathbf{B}_n(x,y) exp\left(\frac{i2\pi zn}{L_z}\right). \tag{2.42}$$

Formal substitution for q_j in Eq. (2.7) with $q_j \mathbf{v}_j$) gives an expression for the current density which upon substitution into Eq. (2.40) in terms of grid values for the n-th mode

$$\mathbf{J}_n(x_g, y_g) = \frac{1}{2\pi a_x a_y} \frac{exp\left(-a_z^2 k_z^2/2\right)}{L_z} S(\mathbf{x} - \mathbf{x}_g)[\mathbf{M}_v(x_g) +$$
$$\mathbf{D}_{vx}(x_{g+1}) - \mathbf{D}_{vx}(x_{g-1}) + \mathbf{D}_{vy}(y_{g+1}) - \mathbf{D}_{vy}(y_{g-1})] \quad (2.43)$$

The Fourier representation of Ampere's law is

$$i\mathbf{k} \times \mathbf{B}(\mathbf{k}) = \frac{4\pi}{c} \mathbf{J}_T(\mathbf{k}). \quad (2.44)$$

Upon taking the cross product with $\mathbf{k}$ and using $\mathbf{k} \cdot \mathbf{B} = 0$, the magnetic field may be expressed as

$$\mathbf{B}_n(k_x, k_y) = i\frac{4\pi}{c} \frac{\mathbf{k} \times \mathbf{J}_n(k_x, k_y)}{k^2}. \quad (2.44)$$

The solution for the transverse component of the electric field $\mathbf{E}_T$ is to be obtained from

$$\nabla^2 \mathbf{E}_T = \frac{4\pi}{c} \frac{\partial \mathbf{J}_T}{\partial t}. \quad (2.45)$$

The removal of the explicit time dependent particle field coupling to neglect retardation effects is also to be applied here since solving for $\partial \mathbf{J}_T/\partial t$ by time extrapolation of $\mathbf{J}$ is numerically inconsistent with our elliptic set of equations and unstable[10]. The path as shown by Busnardo-Neto, et. al [11] around this difficulty is to express $\partial \mathbf{J}_T/\partial t$ in terms of particle quantities given at the time step of the solution.

The Vlasov equation for a given particle species α,

$$\frac{\partial f_\alpha}{\partial t} + \frac{\mathbf{v} \cdot \partial f_\alpha}{\partial \mathbf{x}} + \frac{q_\alpha}{m_\alpha} \left\langle \mathbf{E} + \frac{\mathbf{v}}{c} \times \mathbf{B} \right\rangle \cdot \frac{\partial f_\alpha}{\partial \mathbf{v}} = 0 \quad (2.46)$$

can be used to express the time derivative of the current density due to species α,

$$\frac{\partial \mathbf{J}_\alpha}{\partial t} = \int q_\alpha \mathbf{v} \left(\frac{\partial f_\alpha}{\partial t} \right) d\mathbf{v}$$

$$= -\int q_\alpha \mathbf{v} \left(\mathbf{v} \cdot \frac{\partial f_\alpha}{\partial \mathbf{x}} \right) d\mathbf{v} + \frac{q_\alpha^2}{m_\alpha} n_\alpha \mathbf{E} + \frac{q_\alpha}{m_\alpha c} \mathbf{J}_\alpha \times \mathbf{B}. \quad (2.47)$$

Let

$$\mathcal{V}_\alpha = -\int q_\alpha \mathbf{v} \left(\mathbf{v} \cdot \frac{\partial f_\alpha}{\partial \mathbf{x}} \right) d\mathbf{v}$$

$$- \frac{\partial}{\partial \mathbf{x}} \int q_\alpha \mathbf{v}\mathbf{v} f_\alpha d^3\mathbf{v}. \quad (2.48)$$

The time scales targeted for our model indicates that the guiding center approximation for the electron response is appropriate. The electron kinetic equation applicable is then the drift-kinetic equation,

$$\frac{\partial f_e}{\partial t} = -\left(v_\| \nabla_\| f_e + \frac{c\mathbf{E} \times \mathbf{B}}{B^2} \cdot \nabla f_e \right) + \frac{e}{m} \mathbf{E}_\| \cdot \nabla_v f_e. \quad (2.49)$$

The expression for the time derivative of the current may now be written in terms of particle quantities at the present time,

$$\frac{\partial \mathbf{J}}{\partial t} = -\nabla \cdot \mathcal{V}(\mathbf{x}) + \frac{e^2}{m} n_e(\mathbf{x}) \mathbf{E}_\|(\mathbf{x}) + \frac{e^2}{M} n_i(\mathbf{x}) \mathbf{E}_{(}\mathbf{x}) + \frac{e}{Mc} \mathbf{J}_i \times \mathbf{B}(\mathbf{x}) \quad (2.50)$$

with the identification of the current transfer function, $\mathcal{V} = \mathcal{V}_i - \mathcal{V}_e$. Substituting into Eq. (2.45)

$$c^2 \nabla^2 \mathbf{E}_T = -4\pi \nabla \cdot \mathcal{V}_t(\mathbf{x}) + \omega_{pe}^2 \mathbf{E}_{\|T}(\mathbf{x}) + \omega_{pi}^2 \mathbf{E}_T(\mathbf{x}) + 4\pi \Omega_i \mathbf{J}_i \times \hat{\mathbf{b}}. \quad (2.51)$$

The first term on the right hand side is the divergence of the current transfer tensor, the second term the bulk electron acceleration along the magnetic field lines, the third term the bulk ion acceleration and the last term represents the ion flux across the magnetic field.

In the particle simulation we have already noted the current is given by

$$\mathbf{J}(\mathbf{x}) = \sum_j q_j \mathbf{v}_j S(\mathbf{x} - \mathbf{x}_j). \tag{2.40}$$

Taking the partial derivative with respect to time in the particle's reference frame is equivalent to the total derivative in the grid frame,

$$\frac{\partial \mathbf{J}}{\partial t} = \sum_j q_j \left[\frac{d\mathbf{v}_j}{dt} S(\mathbf{x} - \mathbf{x}_j) - \mathbf{v}_j \mathbf{v}_j \cdot \nabla S(\mathbf{x} - \mathbf{x}_j) \right] \tag{2.52}$$

where the second term on the right hand side is equivalent to the current transfer tensor mentioned above. The particle acceleration is replaced through the appropriate equations of motion to give

$$\frac{\partial \mathbf{J}}{\partial t} = \frac{e^2}{M} \sum_j^{ions} S(\mathbf{x} - \mathbf{x}_j) \int \left[\mathbf{E}(\mathbf{x}') + \frac{\mathbf{v}_j}{c} \times \mathbf{B}(\mathbf{x}') \right] S(\mathbf{x}' - \mathbf{x}_j) dx'$$

$$+ \frac{e^2}{m} \sum_j^{electrons} S(\mathbf{x} - \mathbf{x}_j) \int \left[\hat{\mathbf{b}}(\mathbf{x}') \cdot \mathbf{E}(\mathbf{x}') \hat{\mathbf{b}}(\mathbf{x}') \right] S(\mathbf{x}' - \mathbf{x}_j) dx'$$

$$- \nabla \cdot \sum_j^{\substack{all \\ particles}} q_j \mathbf{v}_j \mathbf{v}_j S(\mathbf{x} - \mathbf{x}_j), \tag{2.53}$$

which matches Eq. (2.47) obtained by the Vlasov approach. The use of the guiding center equation of motion for the electrons removes the electron cyclotron time scale considerations from the simulation model in addition to the removal of the radiative effects.

The integro-differential equation for the transverse electric field,

$$\frac{c^2}{4\pi} \nabla^2 \mathbf{E}_T = \frac{e^2}{M} \sum_j^{ions} S(\mathbf{x} - \mathbf{x}_j) \int \left[\mathbf{E}(\mathbf{x}') + \frac{\mathbf{v}_j}{c} \times \mathbf{B}(\mathbf{x}') \right] S(\mathbf{x}' - \mathbf{x}_j) dx'$$

$$+ \frac{e^2}{m} \sum_j^{electrons} S(\mathbf{x} - \mathbf{x}_j) \int \left[\hat{\mathbf{b}}(\mathbf{x}') \cdot \mathbf{E}(\mathbf{x}') \hat{\mathbf{b}}(\mathbf{x}') \right] S(\mathbf{x}' - \mathbf{x}_j) dx'$$

$$-\nabla \cdot \sum_{j}^{\overset{\overset{all}{particles}}{}} q_j \mathbf{v}_j \mathbf{v}_j S(\mathbf{x} - \mathbf{x}_j), \qquad (2.54)$$

is most readily solved in its Fourier representation. The implementation of the solution method is done for the transverse electric force rather than the transverse electric field. The acceleration integrals need special treatment. These integrals may be expressed as matrices with a wavenumber $\mathbf{k}$ dependence upon summations over a second wavenumber $\mathbf{k}'$. Since these summations contain the transverse electric force, a m by m (m being the number of modes) matrix needs to be inverted. Direct inversion of this matrix is computationally prohibitive in cost and thus an indirect technique, a renormalization method is utilized. This is a preferred method when the off-diagonal terms of a matrix are of a smaller order than the diagonal elements (here by $O(\delta n/n_o)$). The Fourier representation of the transverse electric field equation can be written

$$\frac{k^2 c^2}{\mathbf{V}^2 |S(k)|^2} \frac{N_0}{V} \mathbf{F}_{\mathbf{E}_T}(\mathbf{k}) + \omega_{pe} \left[\sum_{k'} n_e(k') \mathbf{F}_{\mathbf{E}_\parallel}(\mathbf{k} - \mathbf{k}') \right]_T + \omega_{pi} \left[\sum_{k'} n_i(k') \mathbf{F}_{\mathbf{E}}(\mathbf{k} - \mathbf{k}') \right]_T$$

$$= -\frac{\omega_{pi}}{c} \left[\sum_{k'} \mathbf{U}_i(k') \times \mathbf{F}_{\mathbf{B}}(\mathbf{k} - \mathbf{k}') \right]_T + i\omega_{pe} \left[\mathbf{k} \cdot \mathcal{V}(\mathbf{k}) \right]_t$$

$$= \mathcal{S}_T(\mathbf{k}). \qquad (2.55)$$

The iterative technique keeps only the $\mathbf{k} = 0$ terms of $\mathbf{E}_T$ on the left hand side and places the remaining terms on the right hand side. The initial estimate for $\mathbf{F}_T$ only uses $\mathcal{S}_T$. This is substituted back into the right hand side and new iterative estimates for $\mathbf{F}_T$ are solved for until the desired convergence achieved. Busnardo-Neto et. al.[11] have shown that this procedure breaks down when the maximum density exceeded twice the backround density. The further approximation of a low beta, incompressible system is made and thus only the z component of the transverse electric field

is computed and $\mathbf{B}_z$ is taken as constant. The details of the application of this method to the hybrid three dimensional model are presented in Appendix A.

2.5 Time Advancement

The time advancement of the coupled particle-field equations can now be described in detail. At time t=0, the program deposits initial values for the particle velocities and positions, set all plasma derived electromagnetic fields to zero, and inserts the desired backround fields. The particle positions are then advanced to time $\Delta t/2$ by

$$\mathbf{x}_j^{1/2} = \mathbf{x}_j^0 + \mathbf{v}_j^0 \frac{\Delta t}{2} \qquad (2.56)$$

where the superscripts denote the time in units of Δt, $t^n = n\Delta t$. Following this initialization the main time loop is cycled through as the computer experiment evolves.

The ion and parallel electron evolution equations are of the form

$$\frac{dv}{dt} = \mathcal{F}(x) + \mathcal{G}(x,v). \qquad (2.57a)$$

$$\frac{dx}{dt} = v \qquad (2.57b)$$

where $\mathcal{F}$ is derived from the longitudinal electric field and $\mathcal{G}$ is derived from the transverse fields. These equations are pushed using a variant of the leap-frog method,

$$x^n = x^{n-1/2} + v^n \frac{\Delta t}{2}$$

$$\mathcal{G}^n = \mathcal{G}(x^n, v^n)$$

$$x^{n+1/2} = x^n + v^n \frac{\Delta t}{2}$$

$$\mathcal{F}^{n+1/2} = \mathcal{F}(x^{n+1/2})$$

$$\bar{\mathcal{G}}^{n+1/2} = 3/2\ \mathcal{G}^n - 1/2\ \mathcal{G}^{n-1}$$

$$v^{n+1} = v^n + \Delta t(\mathcal{F}^{n+1/2} + \bar{\mathcal{G}}^{n+1/2}).$$

The leap frog technique is commonly used because it is simple and stable for small time step due to its time centered form. Since $\mathcal{G}$ can only be evaluated on the integer time grid, it is extrapolated forward to restore time centering. This extrapolation of $\mathcal{G}$ should not create any major problems in the algorithm when the magnitudes of the longitudinal electric fields due to charge separation are large compared to the current-produced transverse electric fields and the plasma-induced magnetic fields are small compared to the backround magnetic field. The principal components of the fields are then time centered. The extrapolation should thus be sufficiently accurate.

The electron perpendicular evolution equations are in the form

$$v = \mathcal{F}(x) + \mathcal{G}(x,v) \tag{2.58a}$$

$$\frac{dx}{dt} = v. \tag{2.58b}$$

To provide for time centering of these difference equations a form of the predictor-corrector technique is used. For the case of $\mathcal{G} = 0$ this scheme,

$$x^{n+1/2} = x^{n-1/2} + v^n \Delta t$$

$$\mathcal{F}^{n+1/2} = \mathcal{F}(x^{n+1/2})$$

$$x^{n+3/2}_{\text{pred}} = x^{n-1/2} + 2\Delta t \mathcal{F}^{n+1/2}$$

$$\mathcal{F}^{n+3/2}_{\text{pred}} = \mathcal{F}(x^{n+3/2}_{\text{pred}})$$

$$v^{n+1} = \frac{\mathcal{F}^{n+3/2}_{\text{pred}} + \mathcal{F}^{n+1/2}}{2},$$

has been successfully applied to an electrostatic case by Lee and Okuda[8]. To include the functionality represented by $\mathcal{G}$, forward extrapolation is again required to preserve the virtual time-centering.

$$x^n = x^{n-1/2} + v^n \frac{\Delta t}{2}$$

$$\mathcal{G}^n = \mathcal{G}(x^n, v^n)$$

$$x^{n+1/2} = x^n + v^n \frac{\Delta t}{2}$$

$$\mathcal{F}^{n+1/2} = \mathcal{F}(x^{n+1/2})$$

$$\bar{\mathcal{G}}^{n+1/2} = 3/2\, \mathcal{G}^n - 1/2\, \mathcal{G}^{n-1}$$

$$x_{\text{pred}}^{n+3/2} = x^{n-1/2} + 2\Delta t(\mathcal{F}^{n+1/2} + \bar{\mathcal{G}}^{n+1/2})$$

$$\mathcal{F}_{\text{pred}}^{n+3/2} = \mathcal{F}(x_{\text{pred}}^{n+3/2})$$

$$\bar{\mathcal{G}}^{n+1} = 2\mathcal{G}^n - \mathcal{G}^{n-1}$$

$$v_{\text{pred}}^{n+1} = \frac{1}{2}\left(\mathcal{F}^{n+1/2} + \mathcal{F}_{\text{pred}}^{n+3/2}\right) + \bar{\mathcal{G}}^{n+1}$$

$$x_{\text{pred}}^{n+1} = x^{n+1/2} + v_{\text{pred}}^{n+1}\frac{\Delta t}{2}$$

$$\mathcal{G}_{\text{pred}}^{n+1} = \mathcal{G}(v_{\text{pred}}^{n+1}, x_{\text{pred}}^{n+1})$$

$$v^{n+1} = \frac{\mathcal{F}_{\text{pred}}^{n+3/2} + \mathcal{F}^{n+1/2}}{2} + \mathcal{G}_{\text{pred}}^{n+1}$$

Information at the present $n = 1, n, n + \frac{1}{2}$ time locations are used to predict future values of the particle and field quantities. The predicted fields are then used to advance the electron velocity in a virtual time-centered manner.

2.6 Dispersion and Fluctuation Analysis

An electromechanical system consisting of particles with interacting forces and fields exhibits various normal modes of oscillation. The

frequency, ω, and wavenumber, $\mathbf{k}$, response provides information about the particle-field interaction. The fluctuations in the electromagnetic fields are created by the thermal particle motion of a plasma. In turn the plasma particle motion is influenced by the fluctuating electromagnetic fields. Thus a particular electromagnetic mode amplitude that is immersed in the heat bath of many modes interacting with each other through the particles establishes its own average "thermal" level of amplitude. This should be proportional to the thermal level of the particles and to the strength of the coupling between the fields and particles. The coupling strength is related to the dissipative nature of the plasma. This relation manifests itself in the theorem of fluctuation-dissipation[25]. The fluctuation spectra of simulation plasmas should exhibit these features as should any many-body statistical physical system. This section discusses the mode diagnostics, the theoretical dispersion relations appropriate for the model, the fluctuations of modes, and the simulation results to compare with predictions.

For the case of stationary random processes, F, the basis for spectrum analysis is provided by the autocorrelation function

$$C(\tau) = E[F(t)F(t + \tau)], \tag{2.59}$$

where E is the expectation operator. The quantity of interest is the power distribution with frequency. The Wiener-Khinchin relation[26] provides the power spectral density, P, in terms of the Fourier transform of the autocorrelation function,

$$\mathcal{P} = \int_{-\infty}^{\infty} C(\tau) exp(-i\omega\tau) d\tau. \tag{2.60}$$

Replacing ensemble averages by time averages, the autocorrelation function becomes

$$C(\tau) = \lim_{T \to \infty} \frac{1}{2T} \int_{-T}^{T} F(t)F(t + \tau) dt, \tag{2.61}$$

which is then substituted to determine $\mathcal{P}$.

The required field quantities for the desired wavenumbers are written at each time step to external storage over the course of the run. The discrete nature of our knowledge of the field data requires us to replace the autocorrelation integral for the chosen wavenumber by a summation estimate. The most obvious choice is the unbiased estimator

$$C_{\mathbf{k}}(r\Delta t) = \frac{1}{N-r} \sum_{n=1}^{N-r} F_{\mathbf{k}}[n\Delta t]F_{\mathbf{k}}^*[(n+r)\Delta t], \quad r = 0, 1, \ldots m \qquad (2.62)$$

where $r\Delta t$ is the lag time, $m\Delta t$ is the maximum lag time, and N is the number of data points. Blackman and Tukey[27] proposed the spectral estimate as

$$\mathcal{P}_{\mathbf{k}}(\omega) = \Delta t \sum_{r=-m}^{m} C_{\mathbf{k}}(r\Delta t)exp(-i\omega r\Delta t). \qquad (2.63)$$

To reduce possible statistical errors in the estimate of $C_{\mathbf{k}}$ the maximum lag time is constrained to $\tau \le N\Delta t/4$.

Data windowing is employed to improve the frequency resolution of the power spectral density estimates. Spurious high frequency components which have been included due to the finite sample size may thus be filtered out. The convolution of the window transform with that of the actual signal transform means that the most narrow spectral response of the resultant transform is limited to that of the main-lobe width of the window transform. We have chosen to use the Parzen window function [28]

$$W(r\Delta t) = \begin{cases} 1 - 6(r/m)^2 + 6(r/m)^3 & r = 0, 1, \ldots, m/2 \\ 2(1-r/m)^3 & r = m/2 + 1, \ldots, m \\ 0 & r > m \end{cases} \qquad (2.64)$$

to produce a smooth estimate of the power spectral density via

$$\mathcal{P}_{\mathbf{k}}(\omega) = \Delta t \sum_{r=-m}^{m} C_{\mathbf{k}}(r)W(r\Delta t)exp(-i\omega r\Delta t). \qquad (2.65)$$

This discrete transform produces $\mathcal{P}_k$ at discrete frequencies, $\omega = j\Delta\omega$, where $\Delta\omega = 2\pi/m\Delta t$. By choosing $m \ll N$, statistical errors in $\mathcal{P}$ are reduced, however the spectral resolution is lessened by reduction of the number of datapoints in the lag interval, m. These competing requirements constrain the analysis.

The dispersion relation for linear waves may be derived from our modified set of Maxwell's equations plus equations for the particle distribution functions. The electric field may be expressed in terms of the current density as

$$\gamma_{ij}E_j = \frac{-4\pi i}{\omega}J_i \tag{2.66}$$

where

$$\gamma_{ij} = (n^2 + 1)\frac{k_i k_j}{k^2} - n^2\delta_{ij}$$

with $n^2 = k^2 c^2/\omega^2$ and δ_{ij} is a Kronecker delta. Using linearized Vlasov theory, the Fourier transformed plasma current of particle species α can be expressed as a linear function of the electric field through the susceptibility tensor χ_{ij}^{α};

$$J_i^{\alpha}(\omega, \mathbf{k}) = -i\omega\chi_{ij}^{\alpha}(\omega, \mathbf{k})E_j(\omega, \mathbf{k}). \tag{2.67}$$

The current densities of all species can be summed and substituted into Eq. (2.67) to yield

$$\Lambda_{ij}(\omega, \mathbf{k})E_j(\omega, \mathbf{k}) = 0 \tag{2.68}$$

where Λ_{ij} is the dispersion tensor defined by

$$\Lambda_{ij} \equiv \gamma_{ij} + 4\pi\chi_{ij}$$

and $\chi_{ij} = \sum_{\alpha}\chi_{ij}^{\alpha}$. The dispersion relation is obtained from setting the determinant of the dispersion tensor to zero

$$\Lambda \equiv \det|\Lambda_{ij}| = 0. \tag{2.69}$$

The roots of Eq. (2.69) for a given set $(\omega, \mathbf{k})$ determine the normal modes of oscillation.

In the cold fluid approximation the elements of the susceptibility tensor may be determined directly from the particle equations of motion. For a coordinate system with axes defined such that

$$\mathbf{B}_0 = B_0 \hat{k}$$

$$\mathbf{k} = k_x \hat{i} + k_z \hat{k} = k(\sin \phi \hat{i} + \cos \phi \hat{k})$$

where ϕ is the angle between $\mathbf{k}$ and $\mathbf{B}_0$ the electron conductivity tensor elements are given by

$$4\pi\chi^e_{ij} = \begin{pmatrix} 0 & \frac{-i\omega^2_{pi}}{\Omega_i \omega} & 0 \\ \frac{i\omega^2_{pi}}{\omega \Omega_i} & 0 & 0 \\ 0 & 0 & -\omega^2_{pe}/\omega^2 \end{pmatrix} \tag{2.70}$$

Using Eq. (2.16) for the ion equation of motion, the ion conductivity tensor is given by

$$4\pi\chi^i_{ij} = \begin{pmatrix} \frac{-\omega^2_{pi}}{\omega^2 - \Omega^2_i} & -i\frac{\Omega_i}{\omega}\frac{\omega^2_{pi}}{\omega^2 - \Omega^2_i} & 0 \\ \frac{i\Omega_i}{\omega}\frac{\omega^2_{pi}}{\omega^2 - \Omega^2_i} & \frac{-\omega^2_{pi}}{\omega^2 - \Omega^2_i} & 0 \\ 0 & 0 & -\frac{\omega^2_{pi}}{\omega^2} \end{pmatrix} \tag{2.71}.$$

Finite size particle effects are be included in the conductivity tensor by replacing ω^2_{pi} and ω^2_{pe} by $\omega^2_{pi}e^{-k^2 a^2}$ and $\omega^2_{pe}e^{-k^2 a^2}$ respectively.

The dispersion relation for a cold, homogeneous plasma in the magnetoinductive model with perpendicular guiding center electron motion can now be expressed as

$$\tan^2 \phi = \frac{-\left(1 + \frac{\omega^2_p}{\omega^2}\right)\left[\frac{k^2 c^2}{\omega^2} - \frac{\omega^2_{pi}}{\Omega_i(\omega + \Omega_i)}\right]\left[\frac{k^2 c^2}{\omega^2} + \frac{\omega^2_{pi}}{\Omega_i(\omega - \Omega_i)}\right]}{\left(\frac{\omega^2_p + k^2 c^2}{\omega^2}\right)\left[\left(1 - \frac{\omega^2_{pi}}{\omega^2 - \Omega^2_i}\right)\frac{k^2 c^2}{\omega^2} + \frac{\omega^2_{pi}}{\omega^2 - \Omega^2_i}\left(1 + \frac{\omega^2_{pi}}{\Omega^2_i}\right)\right]} \tag{2.72}$$

where $\omega_p^2 = \omega_{pe}^2 + \omega_{pi}^2$. This relation may be expressed as a cubic polynomial in ω^2. The roots of this polynomial yield the eigenfrequencies of the normal modes of oscillation.

Setting $\phi = 0$ in Eq. (2.72) yields three parallel propagating solutions; longitudinal plasma oscillations, whistler waves, and Alfvén waves. For $\phi = 90°$, the compressional Alfvén - lower hybrid and ion cyclotron waves are expected. The upper hybrid wave which appears in a fully electromagnetic model here reduces to a constant term.

When $\phi = 90°$ the warm plasma theory predicts spectral peaks in the vicinity of the lower hybrid frequency, $\omega_{LH}^2 = \omega_{pi}^2 + \Omega_i^2$, and at harmonics of the ion cyclotron frequency. These ion Bernstein modes have, for $\phi = 90°$, the dispersion relation[15]

$$1 - \frac{e^{-k^2 a^2}}{k^2 \lambda_{Di}^2} \sum_{n=-\infty}^{\infty} I_n(\beta_i) e^{-\beta_i} \frac{n\Omega_i}{\omega - n\Omega_i} = 0, \qquad (2.74)$$

where $\beta_i = k_\perp^2 T_i / M\Omega_i^2$, I_n is the modified Bessel function of the first kind, and $\lambda_{Di}^2 = T_i / M\omega_{pi}^2$. The first simulation investigation of the electron Bernstein modes for the full dynamics electron model has been done by Kamimura et. al[30]. An example power spectrum for mode $(k_x = 3, k_y = 0, k_z = 0)$ of the longitudinal electric field from our code is shown in Fig. 2.1. The parameters for this run are $L_x \times L_y \times L_z = 32\Delta \times 32\Delta \times 3200\Delta$, $a_x = a_y = 1.5\Delta$, $a_z = 300\Delta$, $v_{Te} = 1.0\omega_{pe}\Delta$, $M/m = 625.0$, $T_i/T_e = 1.0$, $\Omega_e/\omega_{pe} = 10.0$. The dispersion relation admits several solutions for ω as a function of k. These are drawn along with the points determined from the simulation in good correspondence in Fig. 2.2. For higher harmonics, the simulation modes with low wavenumbers become too weak to observe. We note that Eq. (2.74) fails to yield roots there as well.

The electromagnetic modes predicted for $\phi = 0$ are the whistler waves and shear Alfvén waves. These waves are circularly polarized. The
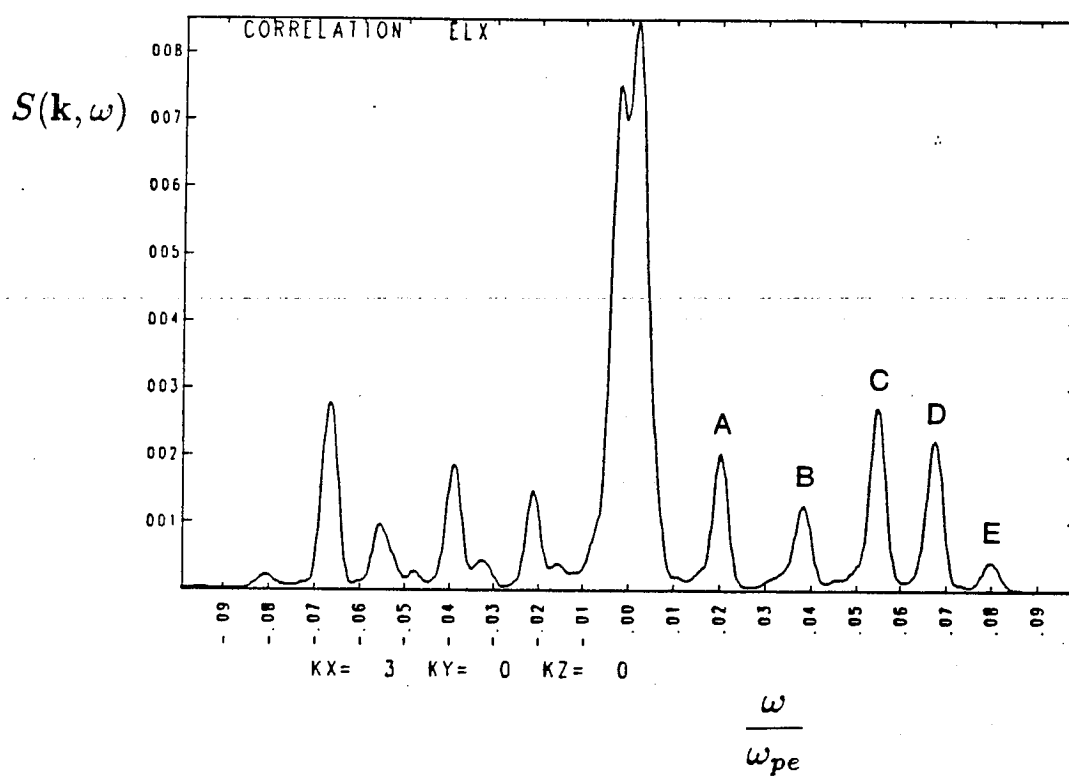
Figure 2.1 $\mathbf{E}_L$ mode spectrum from simulation for mode $(k_x = 3, k_y = 0, k_z = 0)$. Peaks labeled A-E correspond to points similarly labeled in Fig. 2.2.
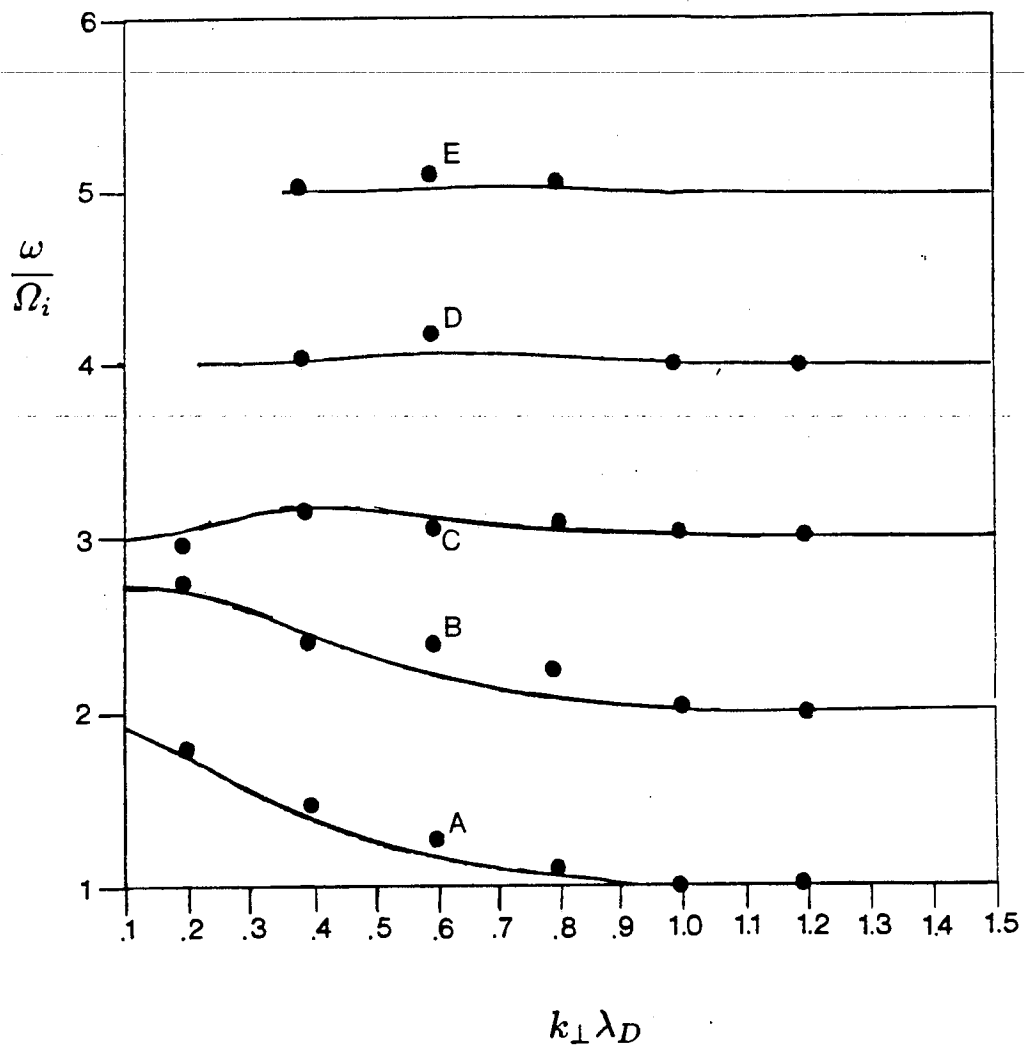
Figure 2.2 Theoretical dispersion curves for ion Bernstein modes with simulation points. Points labeled A-E correspond to the peaks similarly labeled in Fig. 2.1.

whistler wave rotates in the same direction as the electron cyclotron motion. Since we lack thermal electron motion perpendicular to the field we do not expect this mode to be excited from initially thermal conditions. The shear Alfvén wave, however, can be excited since ions carry perpendicular thermal motion. In the cold plasma limit the shear Alfvén wave frequency is given as

$$\omega_{SA} = \frac{k^2 v_A^2}{2\Omega_i} e^{k^2 a^2} \left[\left(1 + \frac{4\Omega_i^2}{k^2 v_A^2} e^{-k^2 a^2} \right)^{1/2} - 1 \right]. \qquad (2.75)$$

This has a small k limit, $\omega = k v_A$, and the large k limit, $\omega = \Omega_i$. Warm plasma effects may be included by use of Vlasov theory. The dispersion function required is,

$$\begin{aligned} \Lambda(\mathbf{k}, w) = & 1 - \frac{k^2 c^2}{\omega^2} \\ & + \frac{\omega_{pe}^2}{\omega^2} \frac{\omega}{\sqrt{2} k_\parallel v_{Te}} Z\left(\frac{\omega + \Omega_e}{\sqrt{2} k_\parallel v_{Te}} \right) \\ & + \frac{\omega_{pi}^2}{\omega^2} \frac{\omega}{\sqrt{2} k_\parallel v_{Ti}} Z\left(\frac{\omega - \Omega_i}{\sqrt{2} k_\parallel v_{Ti}} \right). \end{aligned} \qquad (2.76)$$

For a strongly magnetized plasma $\Omega_e \gg \omega$, and in the magnetoinductive approximation, $k_\parallel^2 c^2 / \omega^2 \gg 1$. This gives a result

$$\Lambda(\mathbf{k}, w) = -\frac{k^2 c^2}{\omega^2} + \frac{\omega_{pe}^2}{\omega \Omega_e} + \frac{\omega_{pi}^2}{\omega^2} \frac{\omega}{\sqrt{2} k_\parallel v_{Ti}} Z\left(\frac{\omega - \Omega_i}{\sqrt{2} k_\parallel v_{Ti}} \right), \qquad (2.77)$$

whose roots determine the frequency response at give wavenumbers. This curve is displayed in Fig. 2.3 along with results from a simulation run with parameters $L_x \times L_y \times L_z = 32\Delta \times 32\Delta \times 1833\Delta$, $a_x = a_y = 1.5\Delta$, $a_z = 300\Delta$, $v_{Te} = 1.0\omega_{pe}\Delta$, $M/m = 625.0$, $T_i/T_e = 1.0$, $\Omega_e/\omega_{pe} = 10.0$, and an angle between $\mathbf{B}$ and the z-axis of $1°$. This tilt of the magnetic field is required to obtain the shear Alfvén wave since a component of $\mathbf{E}_T$ perpendicular to the magnetic field is involved and only the component E_{Tz} is kept in this

incompressible model. The error bars indicate the width of the spectral peaks which is limited by the length of the run.

The distribution of energies among the various modes of a system provides another comparison between the simulation model and the theoretical predictions from statistical mechanics. Application of the classical fluctuation-dissipation theorem[25] can predict the ensemble averaged (here replaced by time averaged) levels of fluctuation in the electromagnetic fields for a homogeneous plasma in thermal equilibrium. This theorem says that if the system response to a weak external field may be described by a linear response function, the ensemble averaged fluctuation energy in each mode is completely determined by the system's dissipation properties.

In a periodic system with Gaussian shaped particles, the fluctuation spectra for the longitudinal electric field component is predicted by Langdon and Birdsall[31] to be

$$V\frac{\left\langle E_L^2 \right\rangle_{\mathbf{k}}}{4\pi} = \frac{T}{1 + k^2 \lambda_{De}^2 e^{k^2 a^2}} \tag{2.78}$$

where $\langle \ \rangle$ denotes an ensemble averaging and V is the simulation volume. This is tested in a triply periodic system with parameters $L_x \times L_y \times L_z = 32\Delta \times 32\Delta \times 3200\Delta$, $a_x = a_y = 1.5\Delta$, $a_z = 300\Delta$, $v_{Te} = 1.0\omega_{pe}\Delta$, $M/m = 125.0$, $T_i/T_e = 1.0$, $\Omega_e/\omega_{pe} = 10.0$. This is displayed in Fig. 2.4.

The fluctuations in the magnetic field are dependent upon the angle ϕ between $\mathbf{B}$ and $\mathbf{k}$. In the simulation model, only the components of $\mathbf{B}$ produced by the plasma in the x-y plane are calculated while the large backround $\mathbf{B}$ is along or nearly along the z-axis. Only the case for $\phi = 90^o$ is presented here. The resultant equation has been reported by Dawson[6] for this case including finite size particle effects and periodic boundary conditions
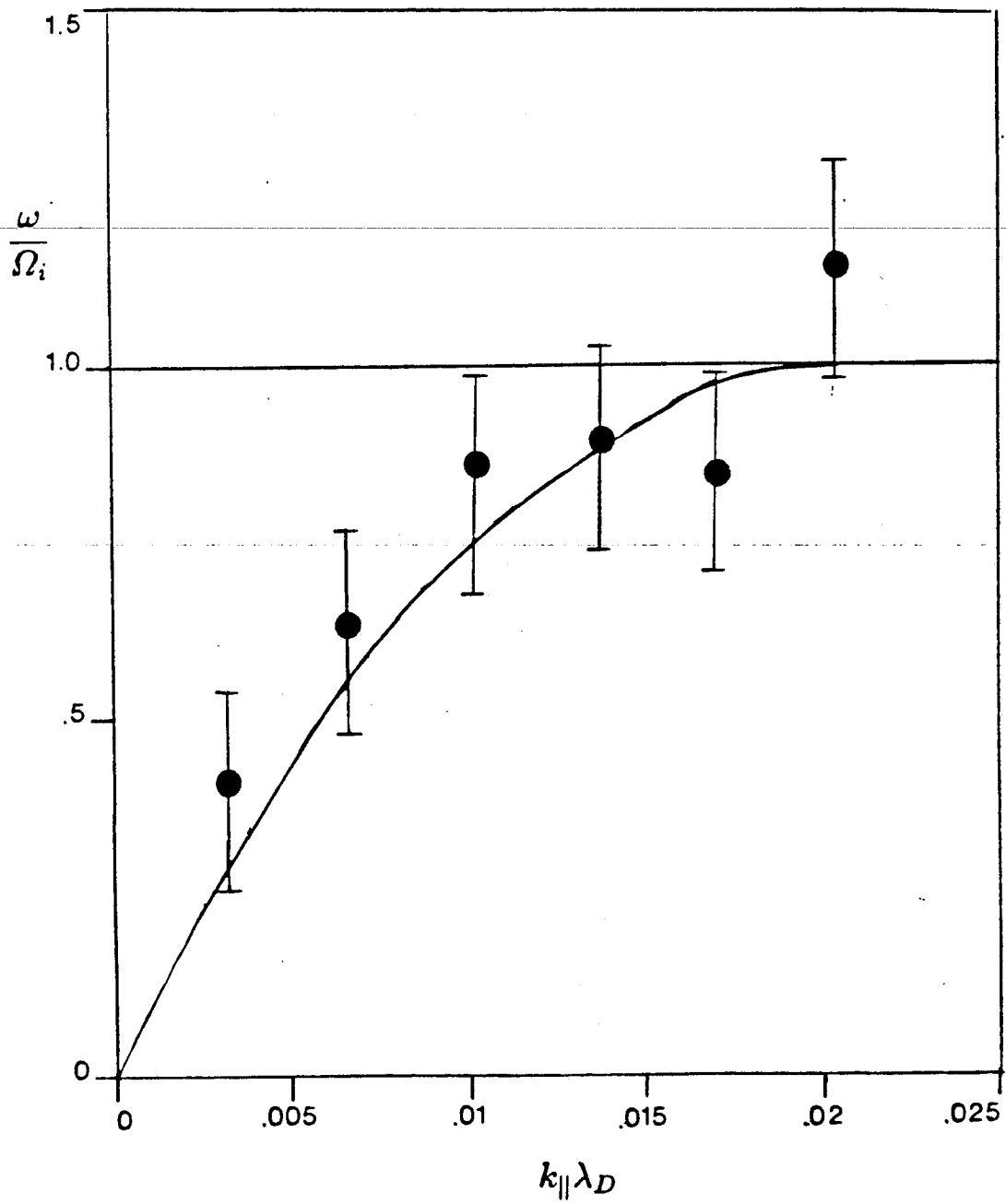
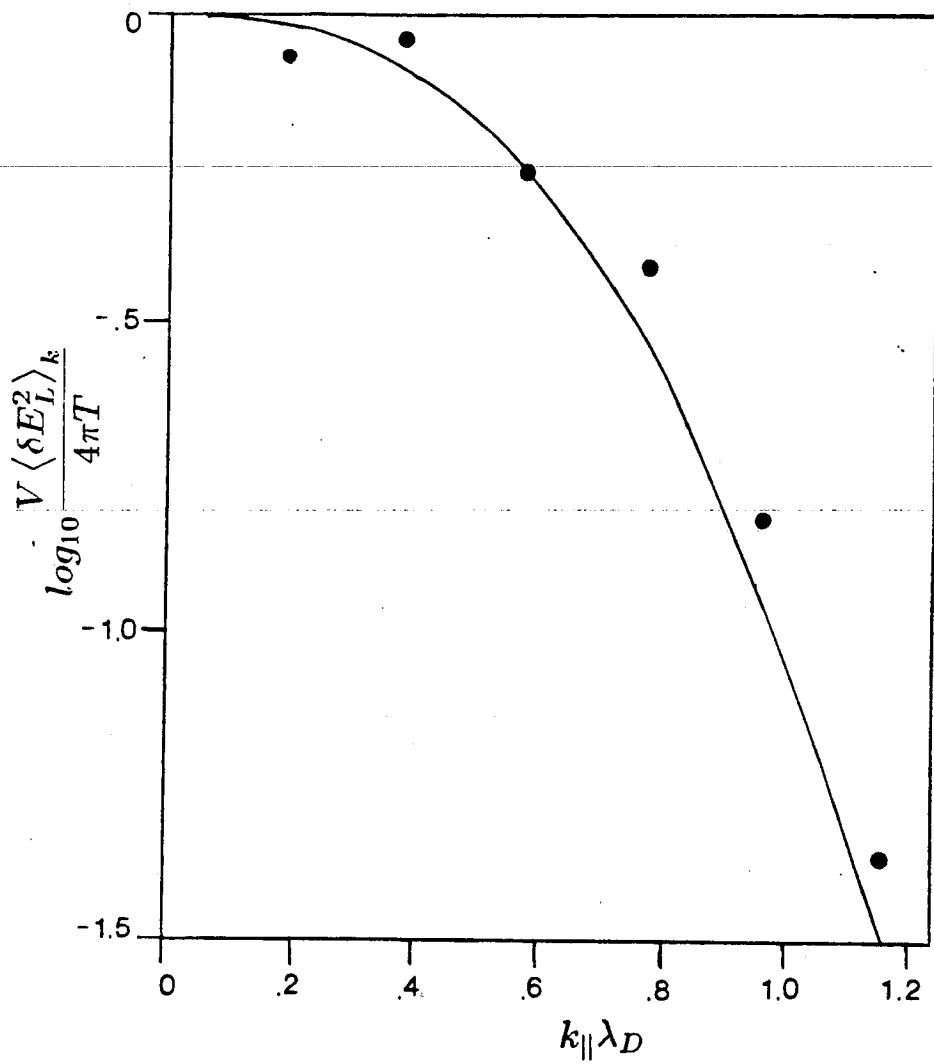Figure 2.3 Shear Alfvén dispersion curve comparing simulation points with warm plasma theory.

Figure 2.4 Longitudinal electric field fluctuation spectrum.

to be

$$V \frac{\langle B^2 \rangle_{\mathbf{k}}}{4\pi T} = \frac{1}{1 + \frac{k^2 c^2 e^{k^2 a^2}}{\omega_{pe}^2}} . \tag{2.79}$$

Simulation results are shown in Fig. 2.5 for the parameters $L_x \times L_y \times L_z = 32\Delta \times 32\Delta \times 3200\Delta$, $a_x = a_y = 1.5\Delta$, $a_z = 300\Delta$, $v_{Te} = 1.0\omega_{pe}\Delta$, $M/m = 625.0$, $T_i/T_e = 1.0$, $\Omega_e/\omega_{pe} = 10.0$. The fluctuation spectrum is somewhat noisier than the electrostatic fluctuation spectrum displayed in Fig. 2.4 since magnetic field fluctuations can take longer to equilibrate, but good agreement is shown.
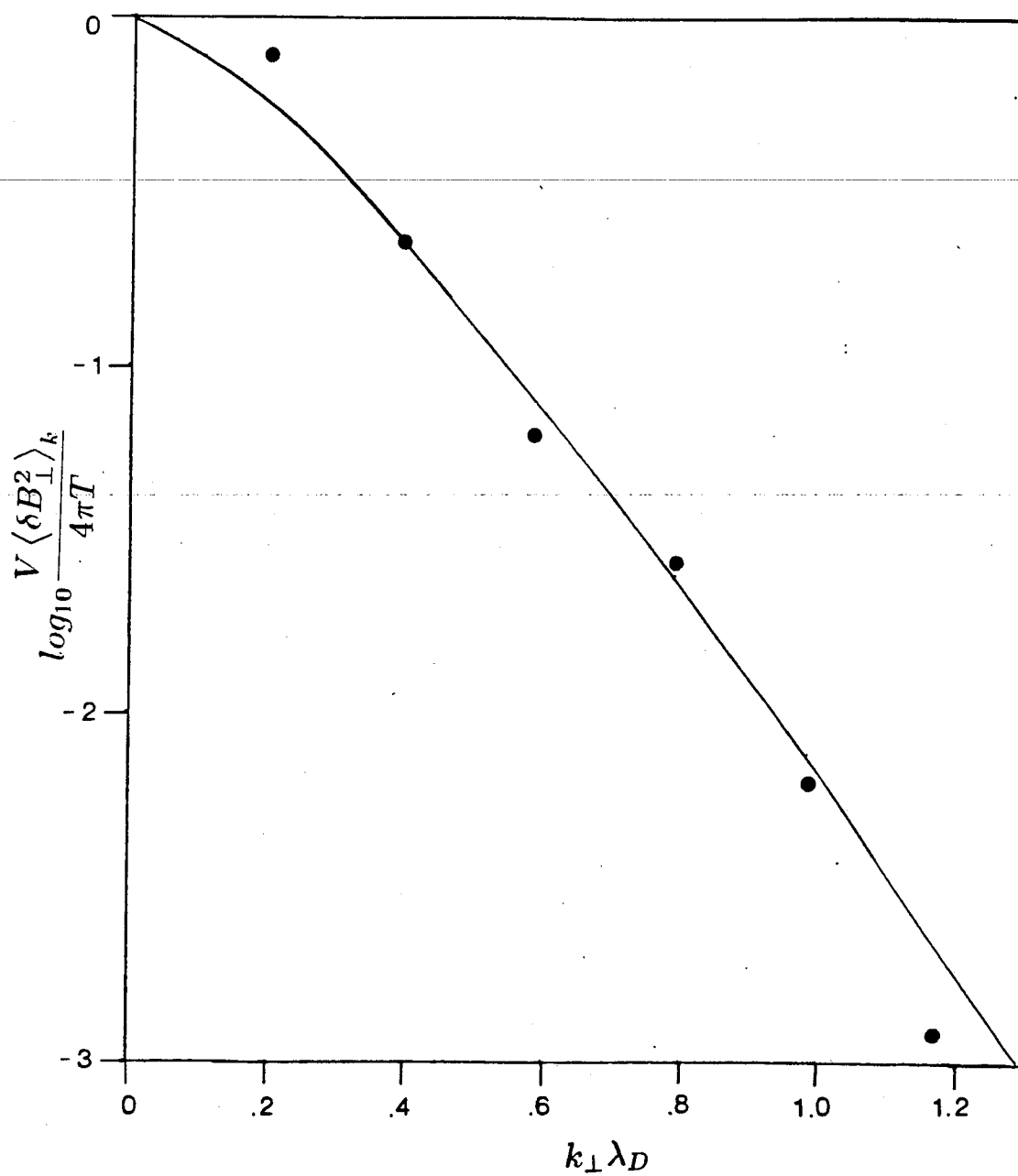
Figure 2.5 Magnetic field fluctuation spectrum for perpendicular propagation.

ALGORITHM

Initialization

$\downarrow$

A

Time Step Cycle

$\downarrow$

Accumulate charge density for each k_z mode

$$\rho^{n+1/2}(k_z) \quad \text{from} \quad \mathbf{x}^{n+1/2}$$

$\downarrow$

Calculate longitudinal electric field for each k_z mode

$$\nabla \cdot \mathbf{E}_L^{n+1/2}(k_z) = 4\pi \rho^{n+1/2}$$

$\downarrow$

Backstep particle positions 1/2 time step

$$\mathbf{x}^n = \mathbf{x}^{n+1/2} - \mathbf{v}^n \Delta t/2$$

Accumulate current, number, and 2nd order current densities
for each k_z mode

$$\mathbf{J}^n, n^n, \langle \mathbf{vv} \rangle^n \quad \text{from} \quad \mathbf{x}^n, \mathbf{v}^n$$

Calculate magnetic fields for each k_z

$$\nabla \times \mathbf{B}^n = \frac{4\pi}{c} \mathbf{J}_T^n$$

Calculate transverse electric fields for each k_z :

Use iterative procedure

$$\nabla^2 \mathbf{E}_T^n = \frac{4\pi}{c^2} \frac{\partial \mathbf{J}_T^n}{\partial t} \left[\mathbf{J}_A^n, \mathbf{J}_i^n, \mathbf{B}^n, n_e^n, n_i^n, \langle \mathbf{vv} \rangle^n, \frac{\mathbf{E}_L^{n+1/2} + \mathbf{E}_L^{n-1/2}}{2}, \mathbf{E}_T^n \right]$$

Calculate $\mathbf{E}$ and $\mathbf{B}$ at the $n + 1/2$ time step for each k_z

$$\mathbf{E}^{n+1/2} = \mathbf{E}_L^{n+1/2} + 3/2\mathbf{E}_T^n - 1/2\mathbf{E}_T^{n-1}$$

$$\mathbf{B}^{n+1/2} = 3/2\mathbf{B}^n - 1/2\mathbf{B}^{n-1}$$

Leap-frog ion velocities and positions

$$\frac{\mathbf{v}_i^{n+1} - \mathbf{v}_i^n}{\Delta t} = -\frac{e}{M}\mathbf{E}^{n+1/2} - \frac{e}{Mc}\frac{(\mathbf{v}_i^{n+1} + \mathbf{v}_i^n)}{2} \times \mathbf{B}^{n+1/2}$$

$$\mathbf{x}_i^{n+3/2} = \mathbf{x}_i^{n+1/2} + \mathbf{v}_i^{n+1}\Delta t$$

Leap-frog parallel electron velocity

$$\mathbf{v}_{e\parallel}^{n+1} = \mathbf{v}_{e\parallel}^n + \frac{e}{m}\mathbf{E}_\parallel^{n+1/2}\Delta t$$

Calculate predictor electron position

$$\mathbf{x}_e^{n+3/2}(\text{pred}) = \mathbf{x}_e^{n+1/2} + \mathbf{v}_{e\parallel}^{n+1}\Delta t - \mathbf{v}_{e\perp}^n\Delta t + \frac{2c}{B_0^2}\mathbf{E}^{n+1/2} \times \mathbf{B}_0\Delta t$$

Calculate predicted charge density for each k_z

$$\rho_{\text{pred}}^{n+3/2} \quad \text{from} \quad \mathbf{x}_i^{n+3/2}, \mathbf{x}_e^{n+3/2}(\text{pred})$$

Calculate predicted $\mathbf{E}_L$ for each k_z

$$\nabla \cdot \mathbf{E}_{L(\text{pred})} = 4\pi\rho_{(\text{pred})}^{n+3/2}$$

Calculated predicted electron perpendicular velocity

$$\mathbf{E}_{T(\text{pred})}^{n+1} = 2\mathbf{E}_T^n - \mathbf{E}_T^{n-1}$$

$$\mathbf{v}_{e\perp(\text{pred})}^{n+1} = \frac{c}{B_0^2}\left\{\mathbf{E}_{T(\text{pred})}^{n+1} + \frac{[\mathbf{E}_{L(\text{pred})}^{n+3/2} + \mathbf{E}_L^{n+1/2}]}{2}\right\} \times \mathbf{B}_0$$

Backstep positions 1/2 time step

$$\mathbf{x}_i^{n+1} = \mathbf{x}_i^{n+3/2} - \mathbf{v}_i^{n+1}\Delta t/2$$

$$\mathbf{x}_{e(\text{pred})}^{n+1} = \mathbf{x}_e^{n+3/2} - (\mathbf{v}_{e\perp}^{n+1}(\text{pred}) + \mathbf{v}_{e\parallel}^{n+1})\Delta t/2$$

Accumulate predicted current, number and 2nd order current densities

for each k_z

$$\mathbf{J}_p^{n+1}, n_p^{n+1}, \langle \mathbf{vv} \rangle^{n+1}$$

Calculate predicted magnetic fields for each k_z

$$\boldsymbol{\nabla} \times \mathbf{B}_{\text{pred}}^{n+1} = \frac{4\pi}{c} \mathbf{J}_{T(\text{pred})}^{n+1}$$

Calculate predicted transverse electric field for each k_z

$$\nabla^2 \mathbf{E}_{T(\text{pred})}^{n+1} = \frac{4\pi}{c^2} \frac{\partial}{\partial t} \mathbf{J}_T^{n+1} \left\{ \mathbf{J}_A^{n+1}, \mathbf{J}_i^{n+1}, \mathbf{B}_{(\text{pred})}^{n+1}, \right.$$

$$\left. n_{e(\text{pred})}^{n+1}, n_{i(\text{pred})}^{n+1}, \langle \mathbf{vv} \rangle_{\text{pred}}^{n+1}, \frac{(\mathbf{E}_{L(\text{pred})}^{n+3/2} + \mathbf{E}_L^{n+1/2})}{2}, \mathbf{E}_{T(\text{pred})}^{n+1} \right\}$$

Corrector step for electron perpendicular velocities and positions

$$\mathbf{v}_{e\perp}^{n+1} = \frac{c}{B_0^2} \left\{ \mathbf{E}_{T(\text{pred})}^{n+1} + \frac{\left[\mathbf{E}_{L(\text{pred})}^{n+3/2} + \mathbf{E}_L^{n+1/2} \right]}{2} \right\} \times \mathbf{B}_0$$

$$\mathbf{x}_e^{n+3/2} = \mathbf{x}_e^{n+1/2} + \left(\mathbf{v}_{e\perp}^{n+1} + \mathbf{v}_{e\parallel}^{n+1} \right) \Delta t$$

Back to A

CHAPTER 3.

THE COALESCENSE AND M=1 KINK INSTABILITIES

3.1 Introduction

The coalescense and m=1 kink instabilities are two examples of current driven instabilities. A common interesting characteristic for these processes is that in both cases the bulk current may be redistributed on a time scale on the order of the Alfvén time. The examples of tokamak confinement and solar flares are but two of the many applications where these phenomena may appear.

Magnetic surfaces can break up into thin filaments, magnetic islands, due to tearing mode instabilities. The time scale of the tearing is much longer than the Alfvén time[32]. The coalescense instability[33,34] provides a mechanism whereby the magnetic field lines can reconnect on a time scale possibly much shorter than that for tearing. The current filaments which produce these magnetic islands attract each other in a plasma as do two parallel wires with currents in the same direction. Under appropriate conditions the islands tend to move together and coalescense. Although the coalescense instability is essentially an ideal MHD instability in the linear theoretical sense, it would not nonlinearly evolve unless there is a resistive (non-ideal MHD) effect, since the magnetic flux which would pile up between the two islands would act to repell the islands. The interesting results[35] obtained from this essentially two dimensional current driven instability has us ask what sorts of phenomenon appear when a variation in the third direction is allowed. Although in two dimensions the configuration of the coalescence is perhaps one of the simplest that could involve a fast reconnection, when the third dimensional variation is allowed we may be able to consider a simpler current distribution that may undergo a fast reconnection of the order of the

Alfvén time scale rather than the tearing time scale. Such a configuration is simply a single toroidal magnetic field for the kink instabilities.

The m=1 kink instability has been extensively studied in both analytical theory and simulation[36,37,38]. This type of instability is driven by current parallel to the magnetic field as may be illustrated in terms of the following models. As one model, first consider a wire or thin plasma aligned initially in the z direction with a current I through it surrounded by a magnetic field, B_z. This current produces an azimuthal magnetic field. If the plasma tube undergoes a small perturbation, as shown in Fig. 3.1, the lines of azimuthal magnetic induction become bunched together on one side of the column compared to the other. The magnetic pressure changes so that the distortion is increased, the $I \times B$ becomes non-zero from this perturbation, and an unopposed destabilizing force acts upon the plasma.

Another model, described by J. L. Johnson, et al.,[39] considers a fat plasma column as in Fig. 3.2. Suppose we perturb this column by a m=1 helical shift while retaining rigid cross sections. Look at two of these cross sections $k\lambda = \pi/2$ apart. If the equilibrium magnetic field sweeps out more than 90° about the axis, the perturbed field will then subtend an even larger angle. In order to traverse this larger angle, the poloidal component of the magnetic field must be increased by the perturbation. This increases the magnetic pressure on one side and accelerates the instability. If, however, the equilibrium magnetic field subtends an angle less than 90°, the perturbation is opposed. This condition on angle is equivalent to a condition on the safety factor, q; $q < 1 \rightarrow$ *unstable*, $q > 1 \rightarrow$ *stable*. This condition is commonly denoted as the Shafranov stability criterion[40]. To determine if a region of plasma is unstable to a kink perturbation, we can calculate a q=1 surface. The region where q is less than one is where we will look for instabilities.
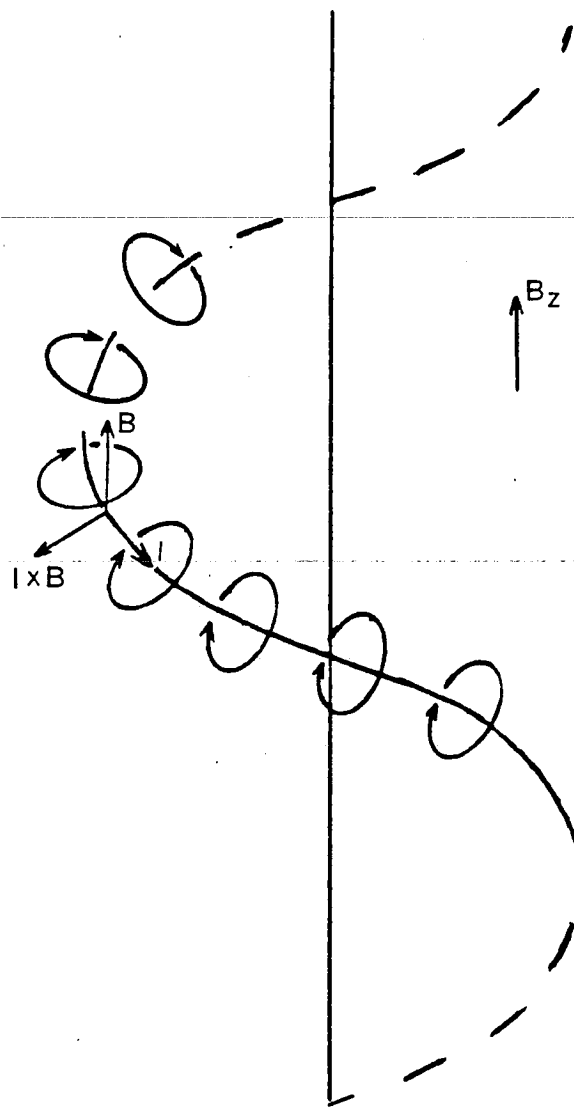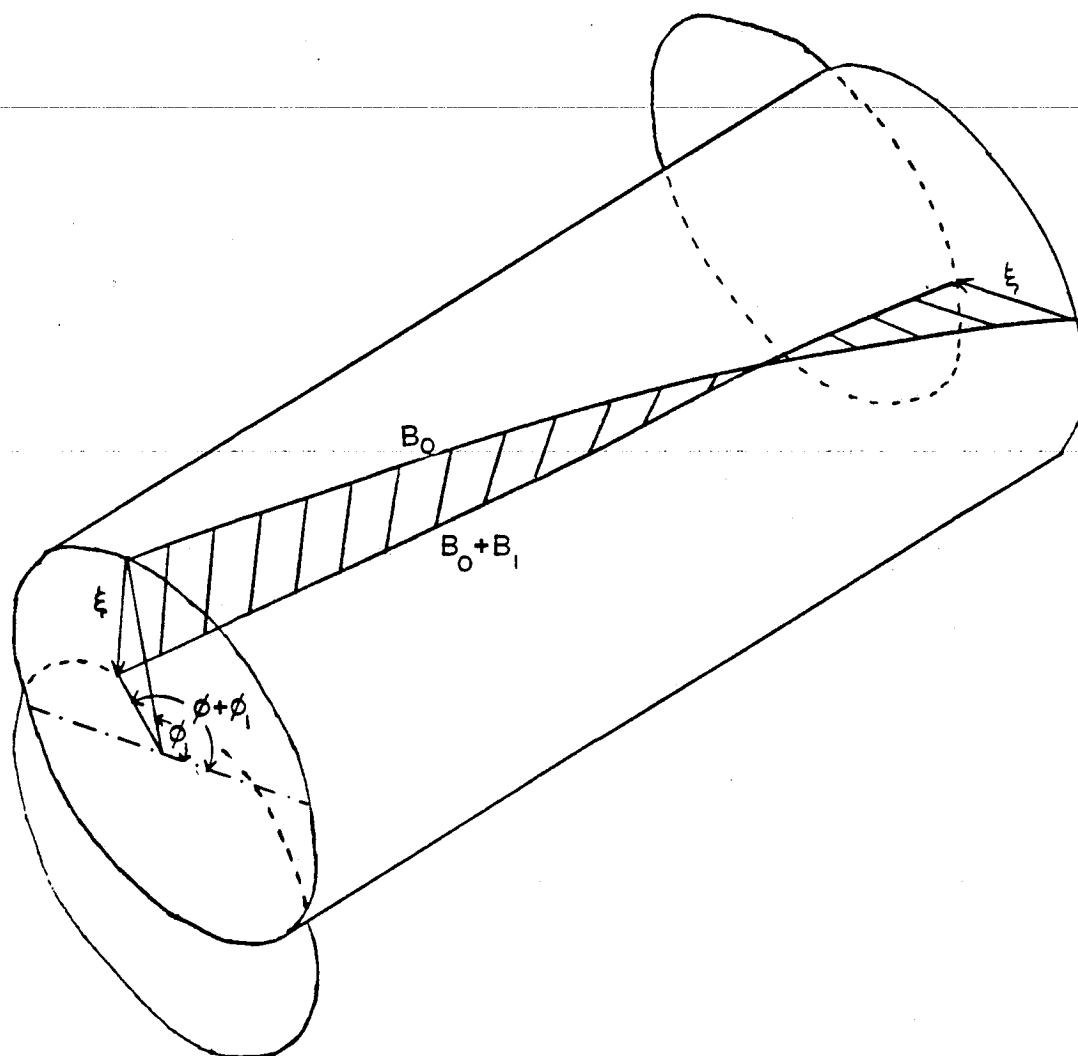
Figure 3.1 Thin plasma kink model.

Figure 3.2 Fat plasma column kink model.

3.2 Simulation Initialization

We look at simulation of the these instabilities as an initial value problem. For both the coalescense instability and the m=1 kink, the initial current distribution (among other factors) determines the quality of the simulation. The addition of a quiet start technique for the current provides a smoothed initial current density to provide an initially smooth azimuthal magnetic field.

A quiet start for the current is obtained by an iterative technique. The particle velocities are initially distributed thermally without regard for their position. This leads to spatially nonuniform distribution of the current density, which taken globally averages to zero. The current density and particle density are accumulated on the grid by use of the subtracted dipole scheme, as in the main body of the code.

$$n(x_g, y_g) = \frac{1}{2\pi a_x a_y} S(\mathbf{x} - \mathbf{x}_g)[M(x_g) +$$
$$D_x(x_{g+1}) - D_x(x_{g-1}) + D_y(y_{g+1}) - D_y(y_{g-1})]. \quad (3.1)$$

$$\mathbf{J}(x_g, y_g) = \frac{1}{2\pi a_x a_y} S(\mathbf{x} - \mathbf{x}_g)[\mathbf{M}_v(x_g) +$$
$$\mathbf{D}_{vx}(x_{g+1}) - \mathbf{D}_{vx}(x_{g-1}) + \mathbf{D}_{vy}(y_{g+1}) - \mathbf{D}_{vy}(y_{g-1})]. \quad (3.2)$$

We wish to have the local current density at each grid node to be zero, so an amount is subtracted from each electron velocity equal to the current density at the nearest grid point to the particle (NGP) divided by the particle density at that same grid point,

$$v_z^{new}(i) = v_z^{old}(i) - [J_z(NGP)/n(NGP)] \quad (3.3)$$

. This does not provide a very smoothed current density since the reaction back to the particle velocities is of lower order than the accumulation to the

grid. To further smooth the local variations in the current density, the above process is iterated, in our case for ten times, so that the desired smoothness in the backround current density is achieved. The applied current density is then loaded into the particle velocities as a position dependent quantity.

3.3 Simulations of the tearing instability

The tearing instability is the tendency for a plasma to break up into magnetic islands so as to reduce the magnetic energy in the regions away from the islands. Consider a sheared magnetic field embedded in a plasma. In a slab geometry, the magnetic field may be taken to be of the form, $\mathbf{B} = B_y(x)\hat{y} + B_z\hat{z}$. The elimination of the magnetic shear in some region of space reduces the free energy in that region. Faraday's law, $\nabla \times \mathbf{E} = -1/c \, \partial \mathbf{B}/\partial t$, and Ohm's law $\mathbf{J} = \sigma(\mathbf{E} + v/c \times \mathbf{B})$, may be combined to give

$$\frac{\partial \mathbf{B}}{\partial t} = \nabla \times (\mathbf{v} \times \mathbf{B}) + \frac{c^2}{4\pi\sigma}\nabla^2 \mathbf{B}. \tag{3.4}$$

If the system is then perturbed, then in the region where $\mathbf{k} \cdot \mathbf{B} = 0$ the magnetic field diffusion is largest.

We simulation the evolution of the tearing instability in the collisionless regime[45,46] by use of a standard 2 1/2 dimensional electromagnetic particle code[43,44] with slab geometry. The initial sheared magnetic field is of the form

$$B_y = \alpha \mid \mathbf{B} \mid tanh(x/L) \tag{3.5}.$$

The corresponding parallel current is thus of the form

$$J_{\parallel} = \frac{c}{4\pi}\alpha\frac{\mid \mathbf{B} \mid^2}{(\mid \mathbf{B} \mid^2 - B_y^2)^{\frac{1}{2}}}\frac{sech^2\left(\frac{x}{L}\right)}{L}. \tag{3.6}$$

The simulation parameters are $L_x \times L_y = 64\Delta \times 64\Delta, \Delta t/\omega_{pe} = 0.1, M/m = 16.0, \lambda_{De}/\Delta = 1.0, \Omega_e/\omega_{pe} = 1.5, T_i/T_e = 1.0, c/\omega_{pe}\Delta = 10.0, \alpha =$

$0.0435, L = 7.36\Delta$. The initial magnetic field profile and current distribution are show in Fig. 3.3. Contours of the projection of the magnetic field into the x-y plane in Fig. 3.4 show the evolution of a magnetic island. The growth rate of the modes in the linear regime are compared with theoretical predictions obtained by solving

$$\nabla^2 \tilde{A}_z = \frac{1}{c^2 \lambda_{De}^2} \left[\omega \left(\langle v_\parallel^3 \rangle - v_{z0} \langle v_\parallel \rangle \right) - \frac{k_y}{\Omega_e} \left(\langle v_\parallel^3 \rangle - v_{z0} \langle v_\parallel^2 \rangle \right) \frac{\partial v_{z0}}{\partial x} \right] \tilde{A}_z, \quad (3.7)$$

with

$$v_{z0} = \frac{c}{4\pi e n_0} \alpha \mid \mathbf{B} \mid^2 \frac{sech^2 \left(\frac{x}{L} \right)}{L}$$

and

$$\langle v_\parallel^n \rangle = \int f_0 \frac{v_\parallel^n}{\omega - k_\parallel v_\parallel} d\mathbf{v},$$

$$f_0 = \frac{1}{\left(M^{\frac{1}{2}} v_{Te} \right)^3} exp \left(-\frac{\mid v - v_{z0} \mid^2}{v_{Te}^2} \right)$$

as an eigenvalue problem via a shooting method code. The growth rates of the magnetic flux thus derived are compared with the simulation results in Fig. 3.5 obtained from the previously described simulation and also for the results of a simulation using an implicit electromagnetic code[43,44]. The evolution of the magnetic island width is also displayed for the implicit run in Fig. 3.6 for the sake of comparison.

3.4 Simulations of the coalescense instability

The process of magnetic field reconnection which attempts to lower the free energy of magnetic island configurations may be carried out by the coalescense instability. We study the coalescense instability by considering a small perturbation applied to an initial magnetohydrodynamic equilibrium consisting of a chain of magnetic islands of the form given by
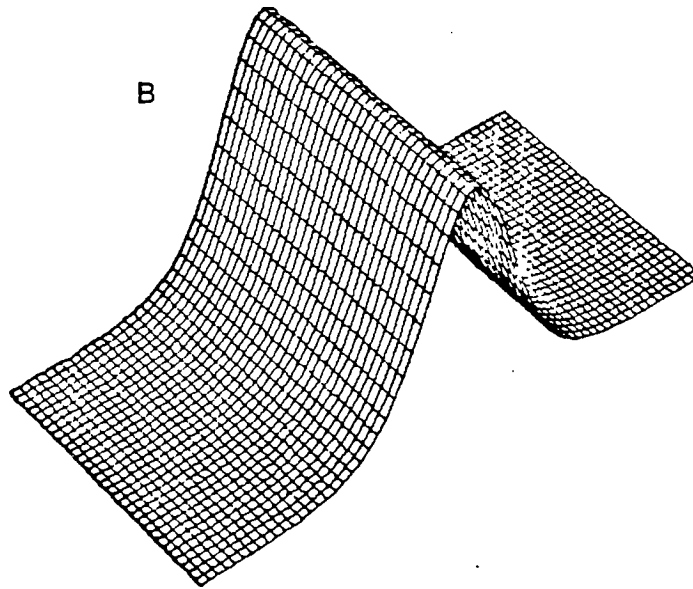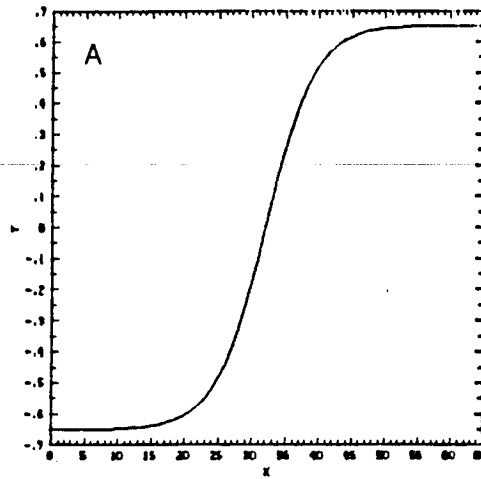
Figure 3.3 Tearing simulation initial magnetic field profile and current distribution.
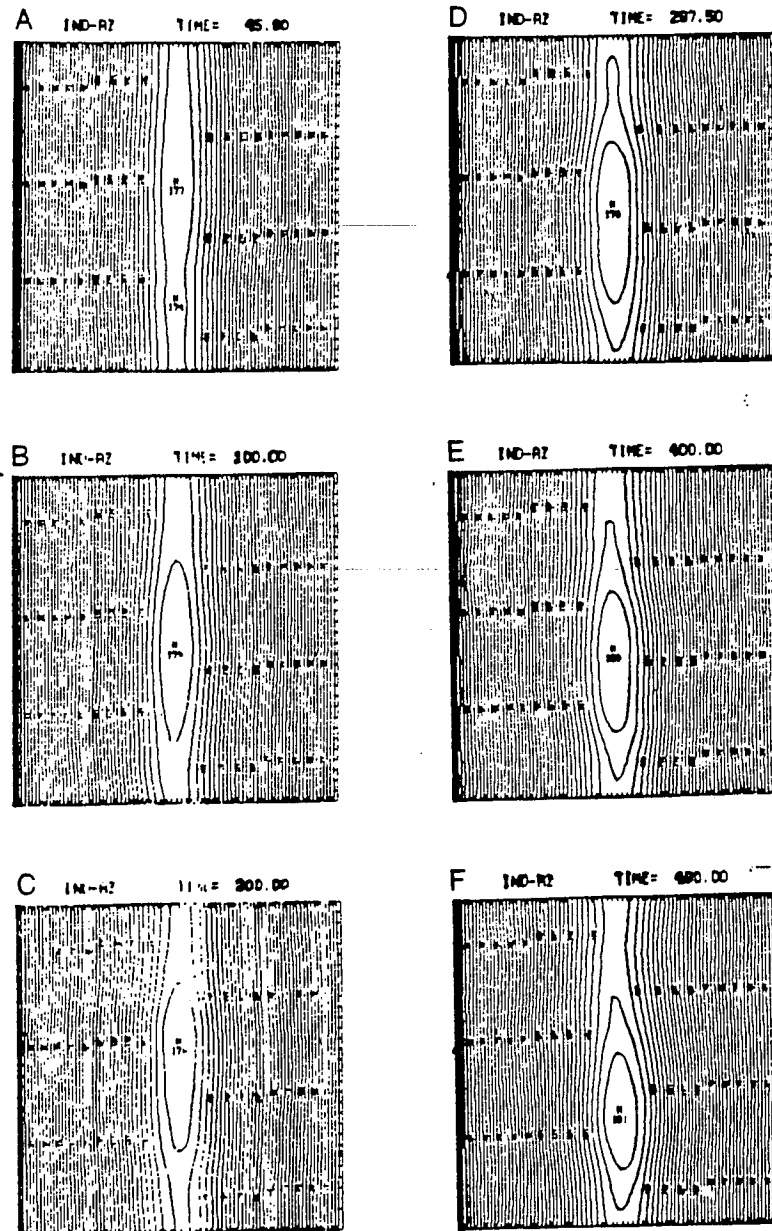
Figure 3.4 Contours of the projection of the magnetic field into the x-y plane show the evolution of a magnetic island.
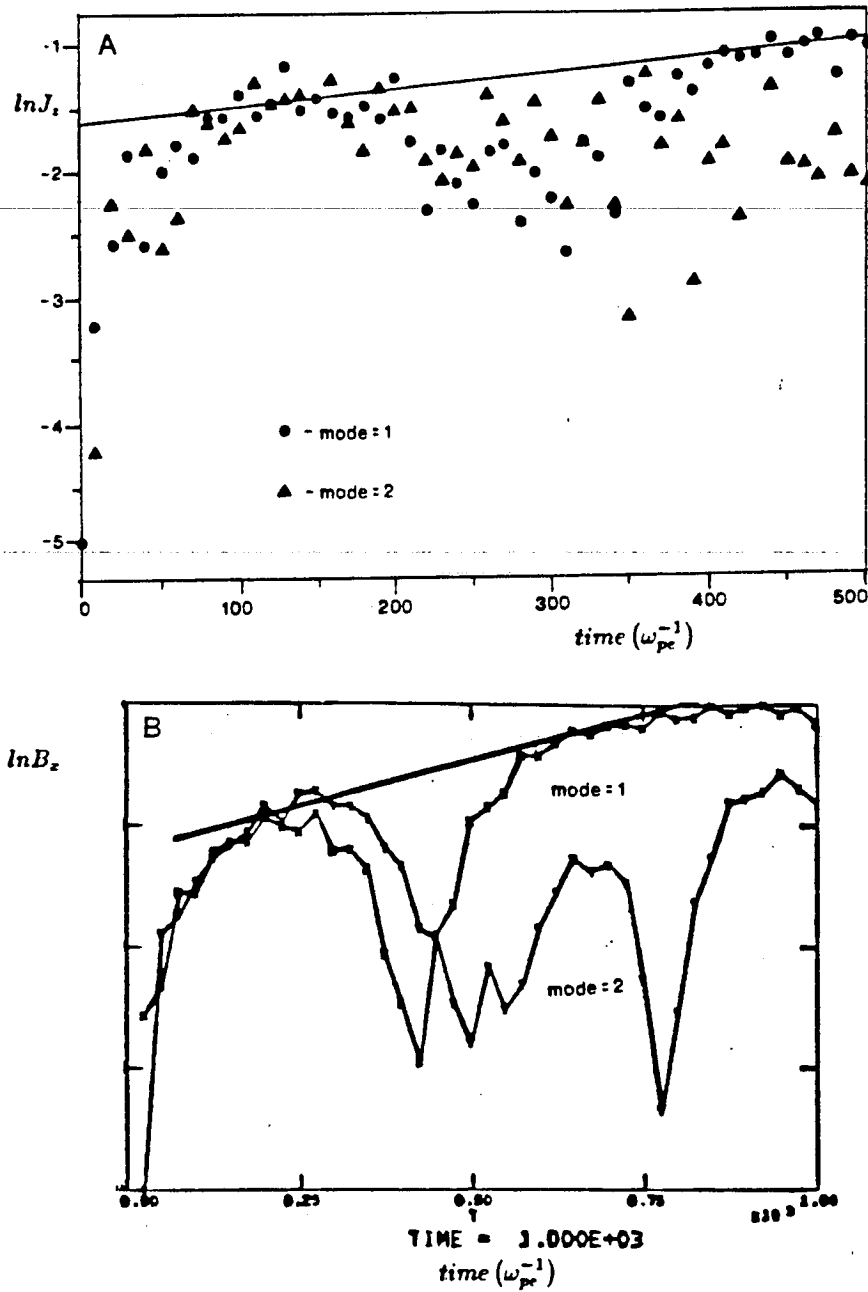
Figure 3.5 Growth of the magnetic flux and comparison with theoretical linear growth rate for (A) the simulation described and also from (B) an implicit electromagnetic code.
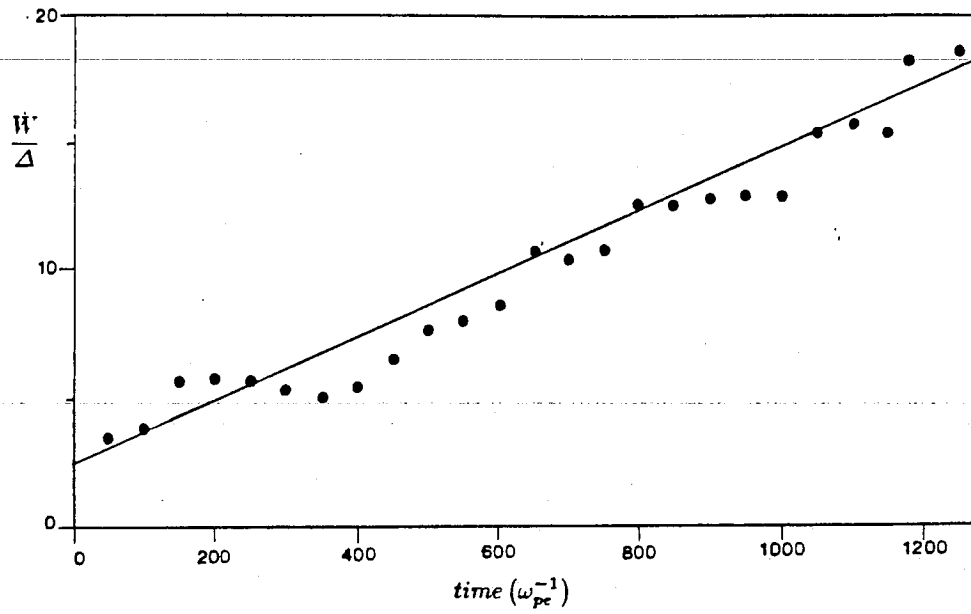
Figure 3.6 The evolution of the magnetic island width from simulation with the previously mentioned implicit code.

Fadeev, et al.[47] This equilibrium is characterized by the current localization parameter ϵ_c. The equilibrium current is taken to be

$$J_z = B_{y0}k(1 - \epsilon_c^2)\frac{1}{(coshkx + \epsilon_c cosky)^2}.$$ (3.8)

The corresponding magnetic field is

$$B_x = B_{y0}\frac{\epsilon_c sinky}{coshkx + \epsilon_c cosky},$$ (3.9)

$$B_y = B_{y0}\frac{sinhkx}{coshkx + \epsilon_c cosky},$$ (3.10)

$$B_z = \left[B_{y0}^2(1 - \epsilon_c^2)\frac{1}{(coshkx + \epsilon_c cosky)^2} + B_{z0}^2\right]^{\frac{1}{2}}.$$ (3.11)

The parameter ϵ_c varies from 0 to 1 with small ϵ_c corresponding to a weak localization and ϵ_c close to unity corresponding to a strong localization; in the limit of $\epsilon_c \rightarrow 1$ the current distribution becomes a delta function. The particle density is taken as initially uniform.

The particle simulation model used here to model the coalescense instability is a standard electromagnetic particle code[43,44] Let us consider two cases which were simulated. The simulation parameters for the first case are $L_x \times L_y = 64\Delta \times 128\Delta$, $\Delta t/\omega_{pe} = 0.1$, $M/m = 16.0$, $\lambda_{De}/\Delta = 1.0$, $\Omega_e/\omega_{pe} = 1.5$, $T_i/T_e = 1.0$, $c/\omega_{pe}\Delta = 10.0$, $B_{y0}/B_{z0} = 0.233$, $\epsilon_c = 0.7$. The initial current distribution in the z direction is shown in Fig. 3.7. Contours of the projection of the magnetic field onto the x-y plane are shown in Fig. 3.8. The MHD equilibrium is perturbed slightly at the start of the simulation by pushing the islands together with an initial velocity of a fraction of v_{Te}. The two initial islands come together and form one island.

The second simulation has parameters $L_x \times L_y = 64\Delta \times 128\Delta$, $\Delta t/\omega_{pe} = 0.1$, $M/m = 16.0$, $\lambda_{De}/\Delta = 1.0$, $\Omega_e/\omega_{pe} = 3.0$, $T_i/T_e = 1.0$, $c/\omega_{pe}\Delta = 5.0$, $B_{y0}/B_{z0} = 0.233$, $\epsilon_c = 0.3$. The initial current distribution
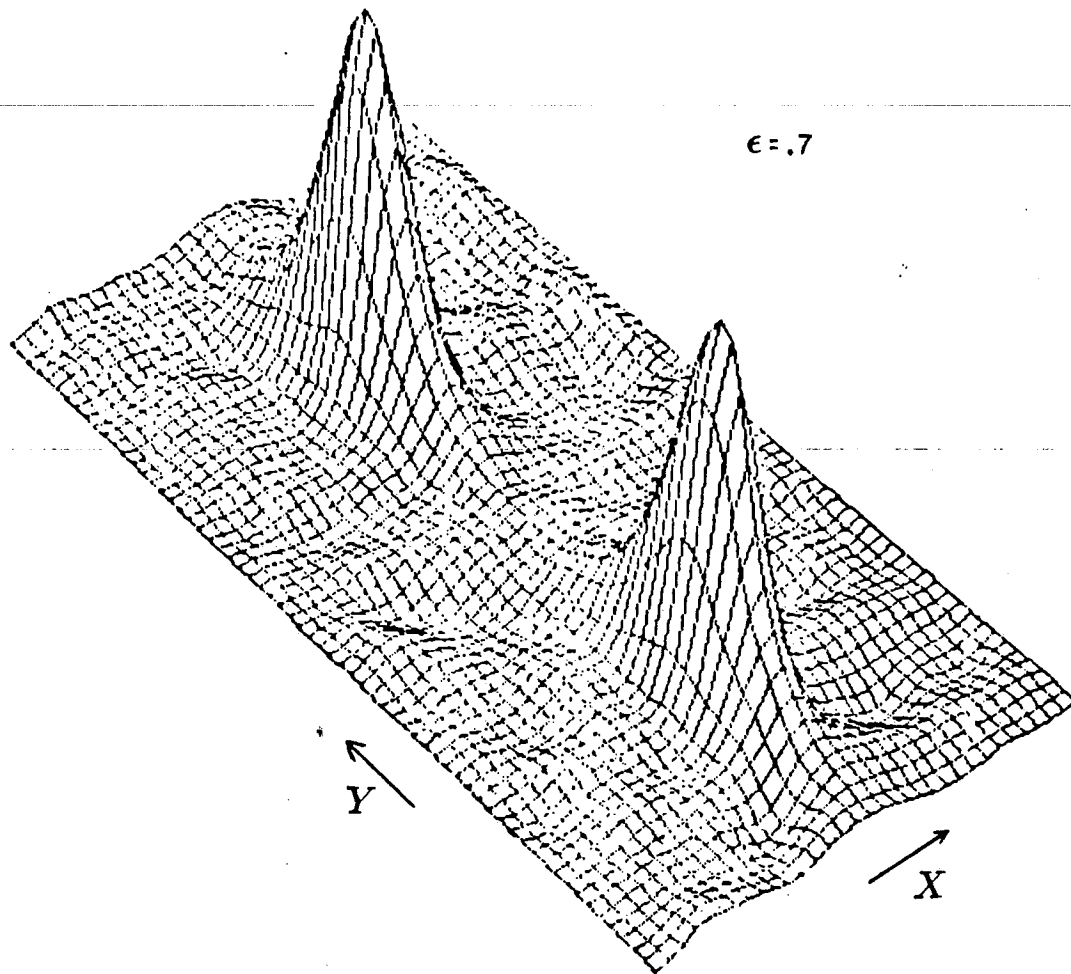
$\epsilon = .7$

Figure 3.7 The initial current distribution in the z direction for coalescense simulation Case 1.
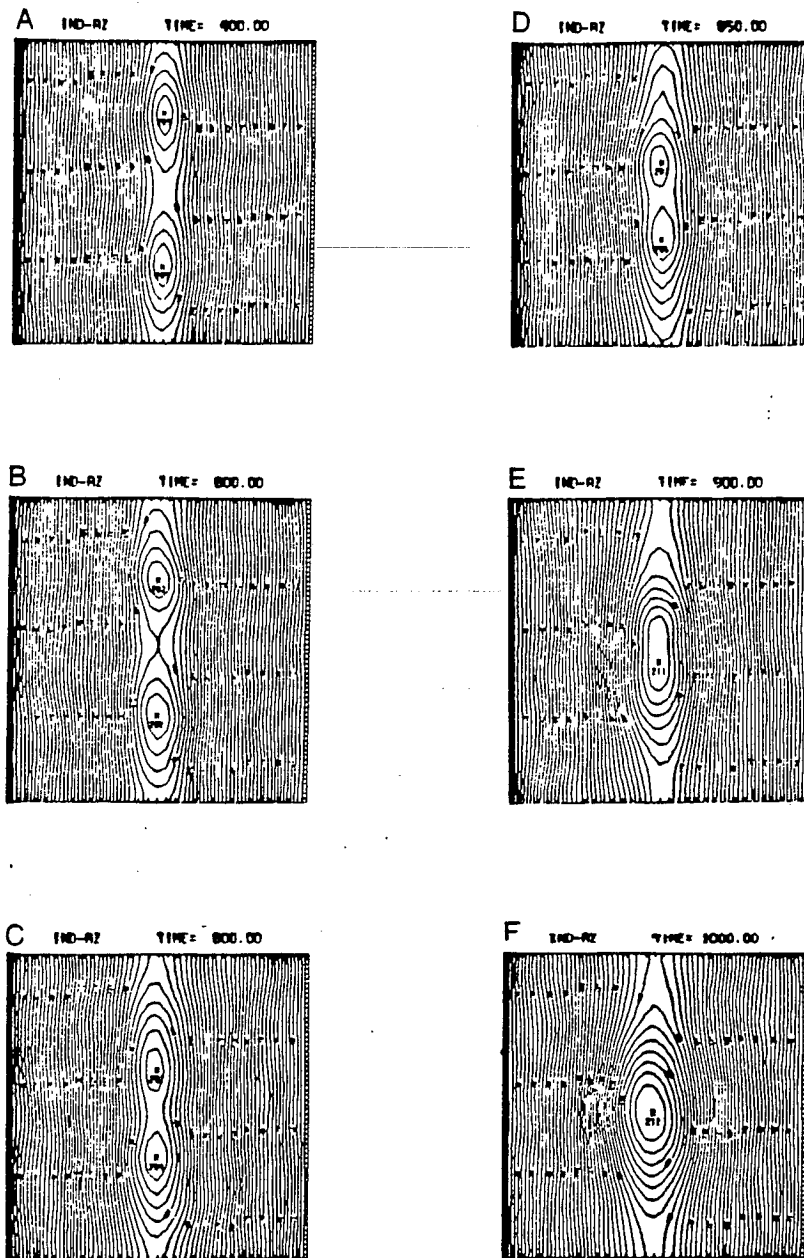
Figure 3.8 Contours of the projection of the magnetic field onto the x-y plane for coalescense simulation Case 1.

is seen in Fig. 3.9 to be not as sharply peaked as the previous case. The magnetic field contours are displayed in Fig. 3.10 and are seen to be much broader than the previous case. The magnetic islands, as they approach each other, do not do so along their initial line of symmetry. Since this run has a strong "toroidal" magnetic field the two islands begin to rotate as they try to coalesce.

3.5 Simulations of the m=1 kink instability

These $2\frac{1}{2}$ dimensional simulations in sections 3.3 and 3.4 exhibit some characteristics of interest in the modeling of fusion devices and of solar flares. They are restricted to single helicity simulation. They are also limited by the restrictions of the electromagnetic model. This model follows the fast time scales of light wave propagation and Ω_e. The restrictions are removed by the use of a three dimensional magnetoinductive model. We have described such a model in the previous chapter. The m=1 kink mode has been the subject of much study and is an essentially three dimensional dynamical mode and was thus selected as the first instability to apply our code to. It is also a basis of investigation that link the two dimensional driven instabilities such as the coalescence and three dimensional drive instabilities.

The initial current profile for the kink simulations is taken as[48]

$$J_z = J_{z0} \left(1 - \left(\frac{r}{r_{minor}} \right)^2 \right)^3 . \tag{3.12}$$

The azimuthal magnetic field is to be determined through the plasma current density which is obtained by the accumulation of the particle velocities to the grid locations. Two cases are discussed in this section. In the first case the simulation parameters are $L_x \times L_y \times L_z = 32\Delta \times 32\Delta \times 3200\Delta$, $\Delta t/\omega_{pe} = 10.0$, $M/m = 625.0$, $\lambda_{De}/\Delta = 1.0$, $\Omega_e/\omega_{pe} = 10.0$, $T_i/T_e = 1.0$, $c/\omega_{pe}\Delta = 4.0$, $J_{z0}/\Delta\omega_{pe} = 2.0$. In Fig. 3.11 the initial magnetic field
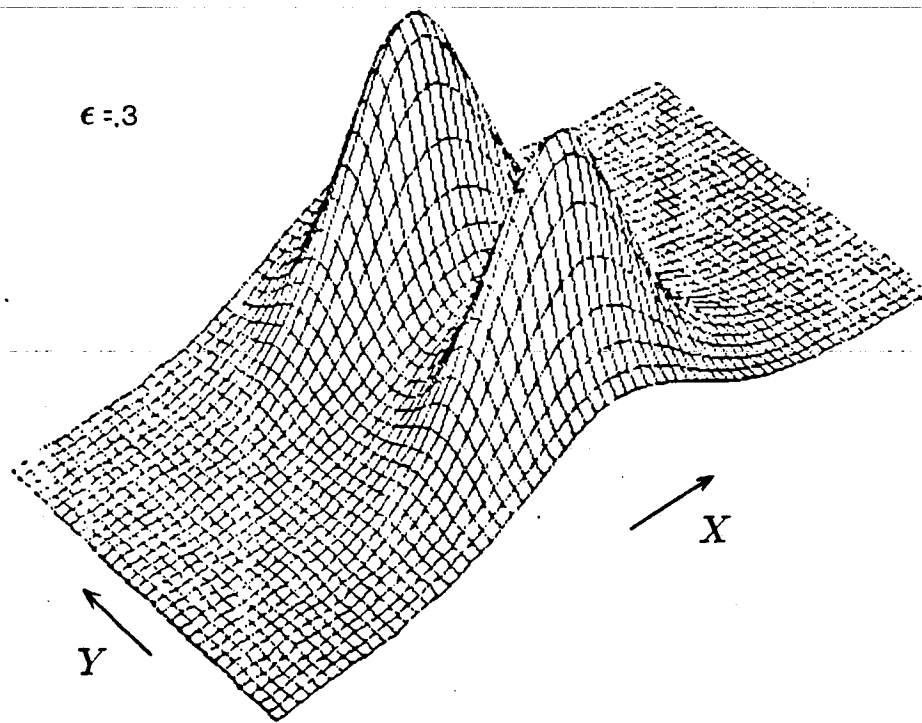
Figure 3.9 The initial current distribution in the z direction for coalescense simulation Case 2.
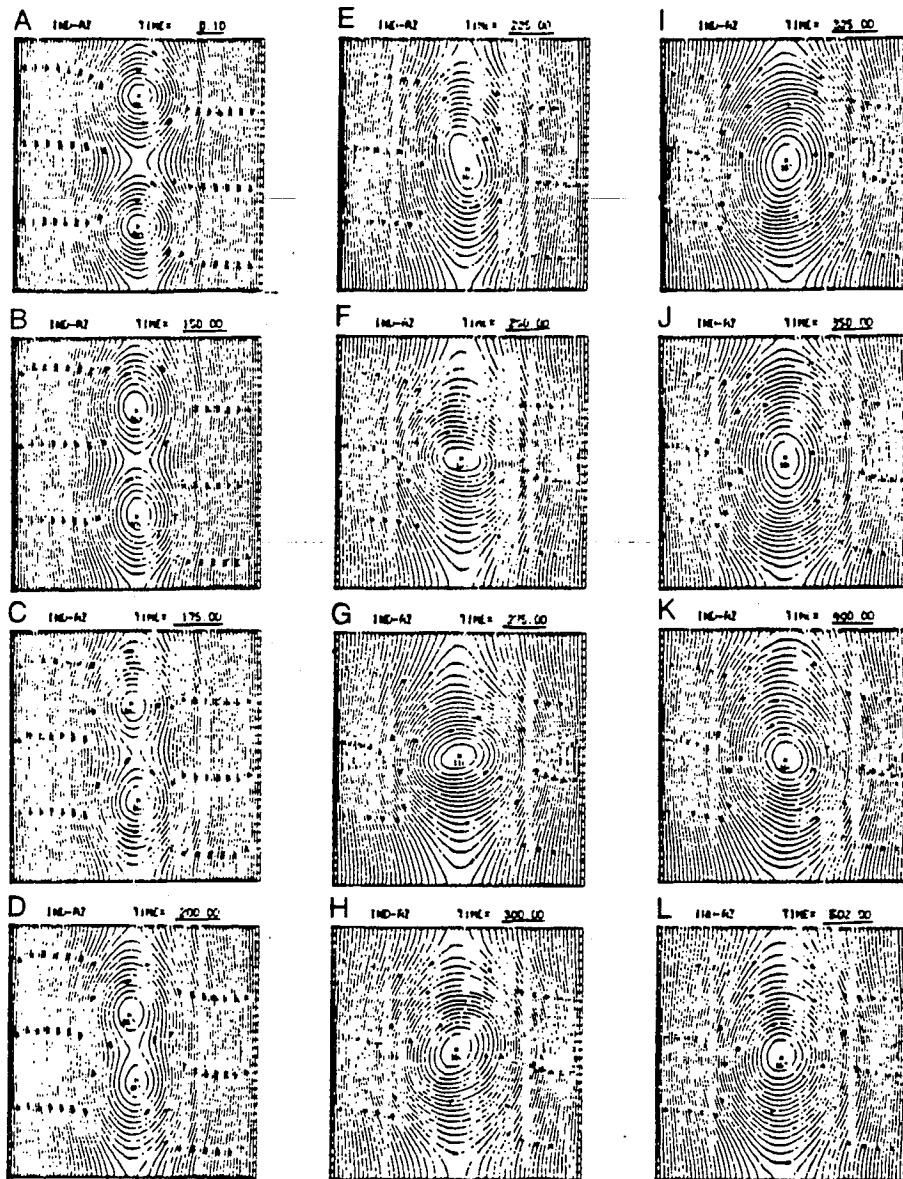
58

Figure 3.10 Contours of the projection of the magnetic field onto the x-y plane for coalescense simulation Case 2.

is contoured at several cross sectional slices along z. The $q = 1$ surface encloses a large portion of the plasma volume. The plasma evolves from these initial conditions by the generation of azimuthal electron flow, as seen in Fig. 3.12, and by the development of a kink structure in the magnetic field. The magnetic field contours at time $1500\omega_{pe}^{-1}$ are presented in Fig. 3.13 along with a perspective view of some field lines in Fig. 3.14. For the second case, the current amplitude is decreased to $J_{z0} = 0.5$. The $q = 1$ surface does not exist in this simulation and the m=1 kink mode does not seem to appear. A perspective view of magnetic field lines both at the beginning of the simulation and at a time after the other simulations observed kink behavior are displayed in Fig. 3.15.

These results are not inconsistent with the linear Shafranov theory of the kink instability. The simulation code which we have developed thus appears able to model the physics associated with kink-type instabilities due to its enhanced time scale and the inclusion of three full dimensions.
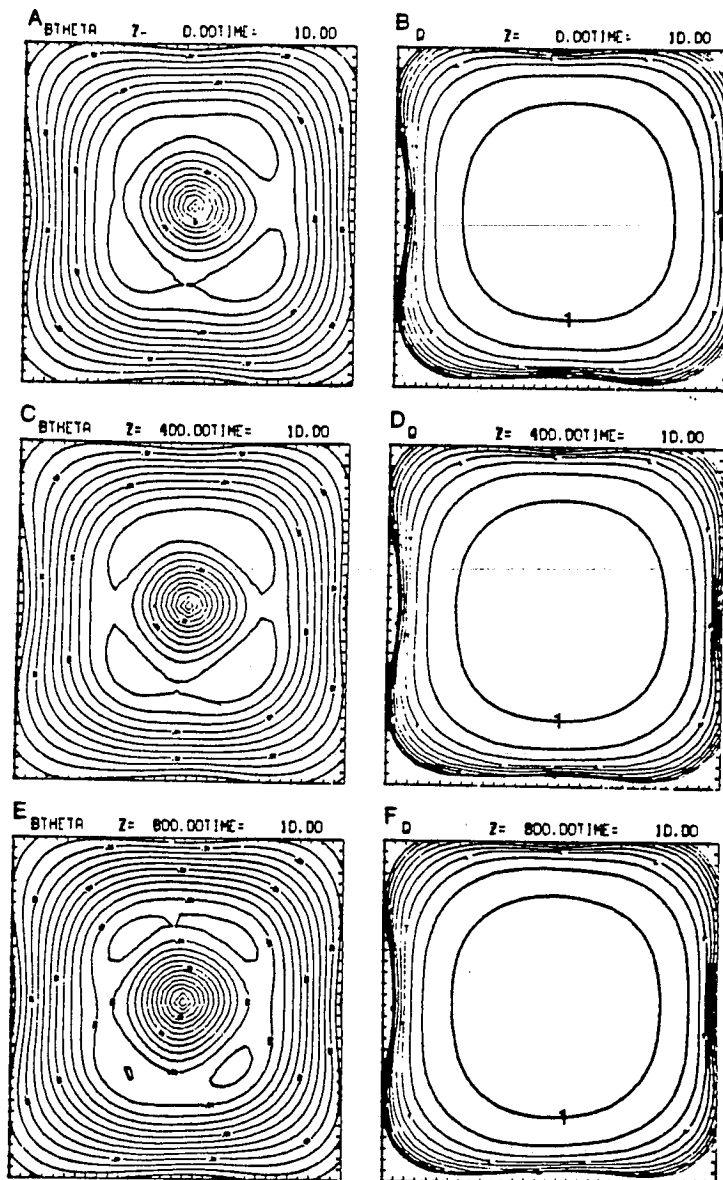
Figure 3.11 Magnetic field contours at the begining of the kink simulation Case 1 at several cross sectional slices along z. The $q = 1$ surface encloses a large portion of the plasma volume.
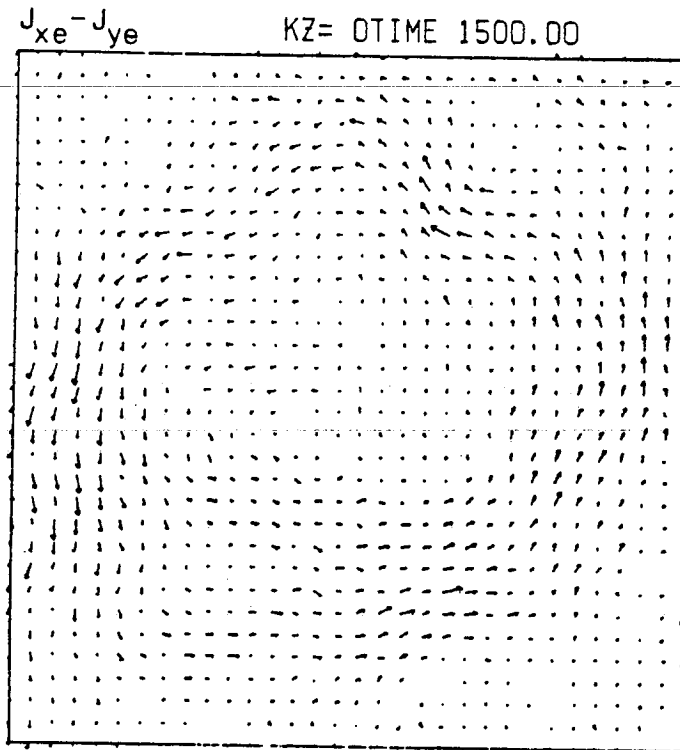
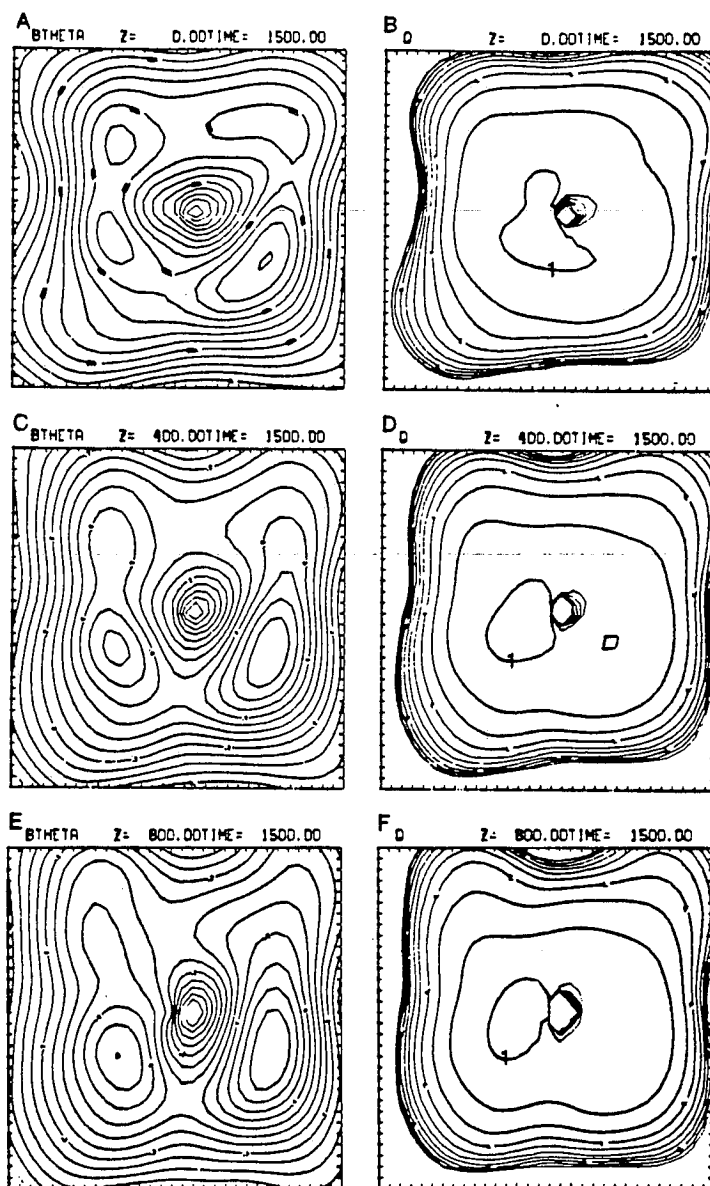Figure 3.12 Electron flow vectors with $k_z = 0$ for Case 1 at time=1500 ω_{pe}^{-1}.

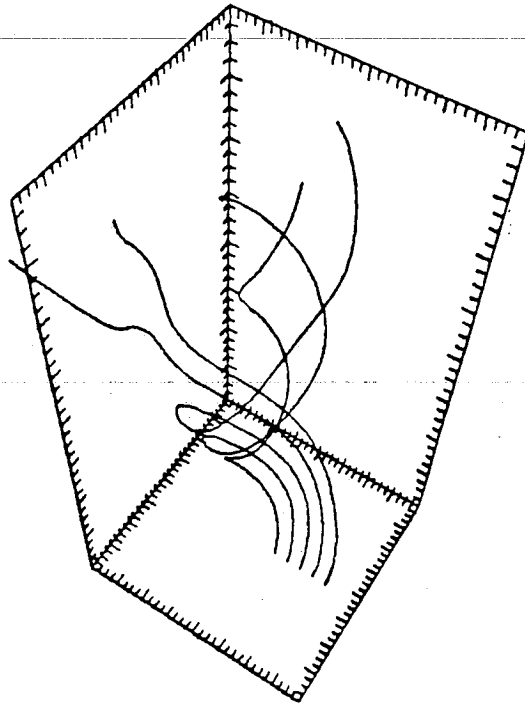Figure 3.13 Magnetic field contours for Case 1 at time=1500 ω_{pe}^{-1}.

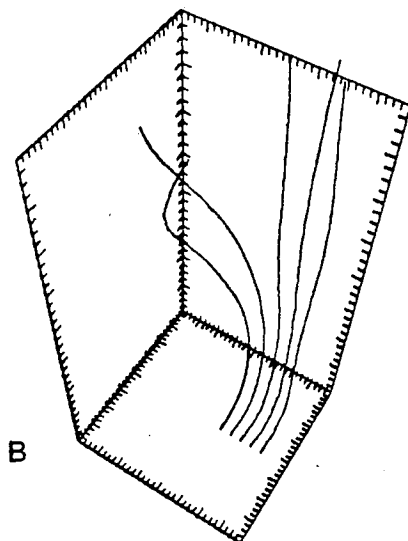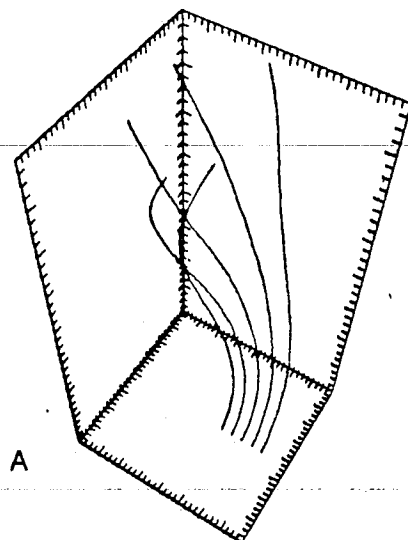Figure 3.14 Perspective view of magnetic field lines for Case 1 at time=1500 ω_{pe}^{-1}

Figure 3.15 Perspective view of magnetic field lines for Case 2 initially (A) and at long times (B).

CHAPTER 4.

THE TWIST-KINK INSTABILITY

4.1 Introduction

The introduction of differential rotation of a plasma about an axis parallel to the backround magnetic field can produce a variant of the kink mode which we denote as the twist-kink instability. Recent interest has appeared in the application of twisting of a plasma column to instabilities associated with the tandem mirror[49,50] and with solar flares[51,52].

In a tandem mirror[53], axial variation in the equilibrium $\mathbf{E} \times \mathbf{B}$ velocity occurs for even the simplest model consisting of two regions, i.e. a central cell and end cells. Since the electrons escape through the magnetic mirrors much faster than the ions do, because of Coulomb pitch-angle scattering, an ambipolar electric field is established in the plasma. The profile of the ambipolar potential is related to the ion profile via Boltzmann's law

$$n_i(r, z) = n_0 exp \frac{\phi(r, z) - \phi_0}{T}. \tag{4.1}$$

Since the plasma has thus acquired a net positive charge, a radial electric field which is on the order of $E_r(z) = -\phi(z, r = 0)/a$ is induced. Since the density varies axially, the potential does also. Sample density and potential profiles along with the corresponding magnetic field profile are shown in Fig. 4.1. The $\mathbf{E}_r \times \mathbf{B}_z$ plasma rotation thus varies along z.

The eruption of flux from the photospheric region of the sun to form coronal loops is a complex phenomenon. A schematic diagram of this occurence is show in Fig. 4.2. This situation is further complicated by the recognition that photospheric shear motion at the feet of the loop acts to twist the column as shown in Fig. 4.3.
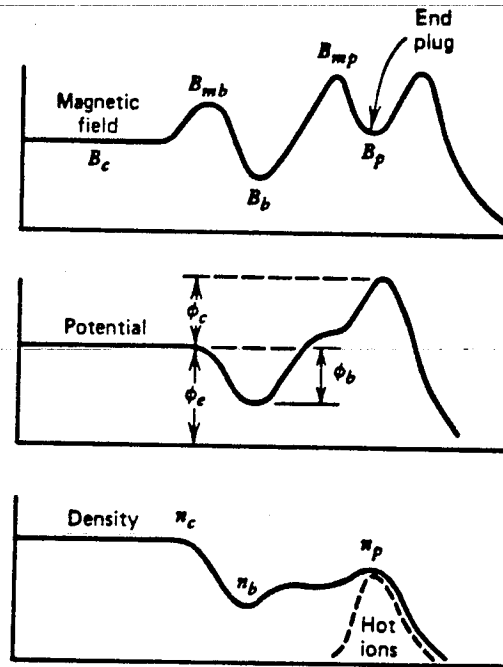
Figure 4.1 Sample profiles of magnetic field, potential and density for a tandem mirror.
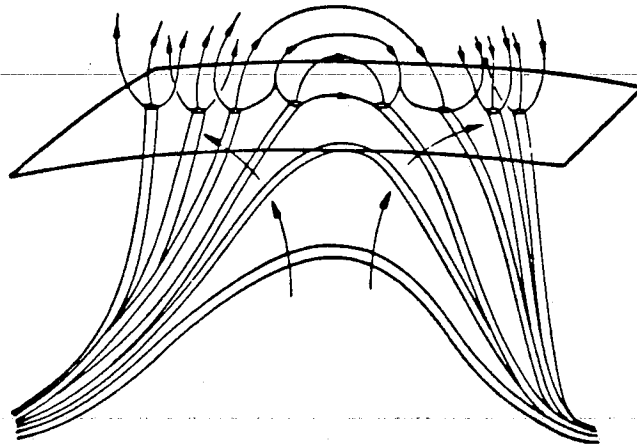
Figure 4.2 A schematic diagram of the eruption of flux from the photospheric region of the sun to form coronal loops.
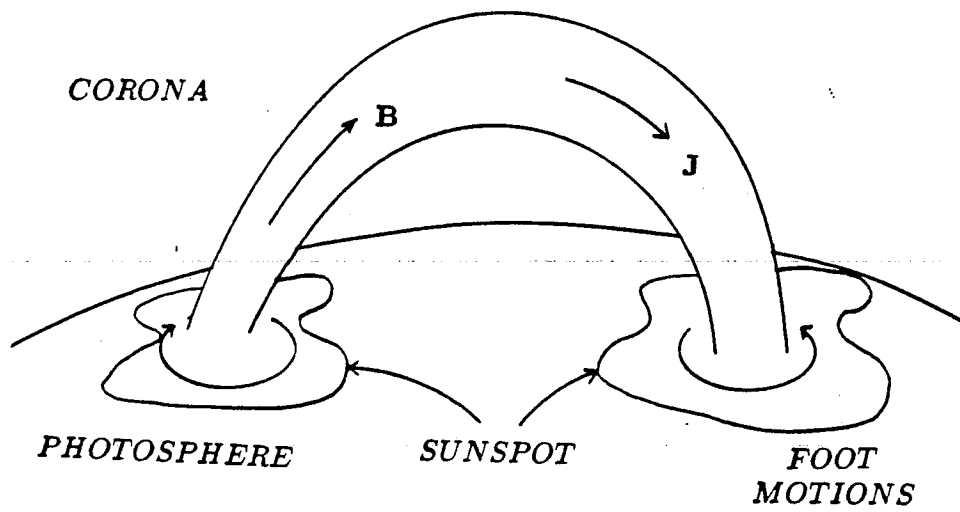
Figure 4.3 Photospheric shear motion at the feet of a coronal loop acts to twist the column.

The MHD description of the mechanism whereby the differential twisting of a plasma column develops a kink structure is described by the following equations. The azimuthal velocity of the twisting motion about the magnetic field gives rise to an increase in the azimuthal component of the magnetic field.

$$\left(\frac{\partial \mathbf{B}(r,z)}{\partial t}\right)_\theta = \nabla_z \times (\mathbf{v}_\theta(r,z) \times \mathbf{B}_z)_r \qquad (4.2)$$

This increase in the magnetic field corresponds to an increase in current along the column.

$$\mathbf{J}_z(r,z) = \frac{c}{4\pi}\nabla_r \times \mathbf{B}_\theta(r,z) \qquad (4.3)$$

This current eventually can build up to sufficient current, for long enough twisting times, to cause kink type instabilities. However, this current is function of z so that it exceeds a threshold for kink motion only locally in z.

4.2 Simulation Results

These rotations are generated by imposing an external radial electric field on the plasma column. The plasma is assumed to be strongly magnetized so that $\mathbf{B}_z$ is constant (incompressible toroidal magnetic field). The twisting electric fields, constant in time, are given externally as

$$\mathbf{E}_r(r,z) = \mathbf{E}_{r0}sin^\epsilon \left(\frac{\pi}{r_0}r\right)cos\left(\frac{2\pi}{L_z}\right) \quad (r < r_0). \qquad (4.4)$$

This radial field gives rise to an azimuthal flow of electrons and ions both with $\mathbf{v}_\theta(r,z) = c\mathbf{E}_r(r,z) \times \mathbf{B}_z/B_z^2$. This azimuthal flow v_θ peaks at $r = r_0/2$, having a shear $(d\omega/dr \neq)$. In the vicinity of $r = 0$ the azimuthal flow is close to the rigid body rotation when $\epsilon = 1$. As r increases, the shear in the flow increases. The plasma experiences no externally imposed azimuthal flow beyond $r \geq r_0$. The largest amount of differential rotation takes place at

$2\pi z/L_z = \pi/2$ and $3\pi/2$. We expect that the twisting of the plasma induces a field aligned current (J_z) due to the injected helicity, a pinching of the plasma column, and an eventual kink instability due to the large induced axial current.

Several different cases were simulated. The first simulation is set up with the following parameters: $M/m = 125$, $v_{Te} = \omega_{pe}\Delta$, $\Omega_i/\omega_{pi} = v_A/c = 0.4$, $\Omega_i = 8 \times 10^{-2}\omega_{pe}$, $\rho_i = 1.1\Delta$, $v_A = 1.6\omega_{pe}\Delta$, $L_z = L_y = 32\Delta$, $L_z = 3200\Delta$, $\omega_{pe}\Delta t = 10$. The plasma β is 1.25×10^{-3} and thus the use of our low beta model is appropriate. The applied radial electric field has peak magnitude $E_{r0} = 0.5\dfrac{m}{e}\Delta\omega_{pe}^2$ with an $\epsilon = 1$ radial dependence with maximum radial distance $r_0 = 14\Delta$. The plasma is initially uniform in density and contains only a constant B_z field.

A perspective view of five radially distributed magnetic field lines are shown in Fig. 4.4(a) at the first time step. At the relatively early time of $200\omega_{pe}^{-1}$, a similar perspective plot, Fig. 4.4(b) shows a twisting of the magnetic field developing. Figures 4.5 and 4.6 refer to time $200\omega_{pe}^{-1}$. The $k_z = 2\pi/L_z$ Fourier component of the applied radial electric field plus the electric field due to electrostatic charge separation are combined in Fig. 4.5(a). The applied field is clearly dominant. A clear pattern of plasma rotation due to the external twisting $\mathbf{E}_r \times \mathbf{B}_z$ is seen in the velocity flow diagram of Fig. 4.5(b). As the plasma twist continues, the plasma is pinched and the density increases near the $r=0$ axis and the field aligned current, J_z, is induced, (Fig. 4.6(a)). This produces the poloidal magnetic field, B_θ, as seen in Fig. 4.6(b).

The current is peaked near $r=0$ and so is B_θ. Thus the total magnetic field $\mathbf{B}$ starts to acquire shear in the radial direction. The sheared magnetic field structure may be best illustrated by the analysis of the mag-
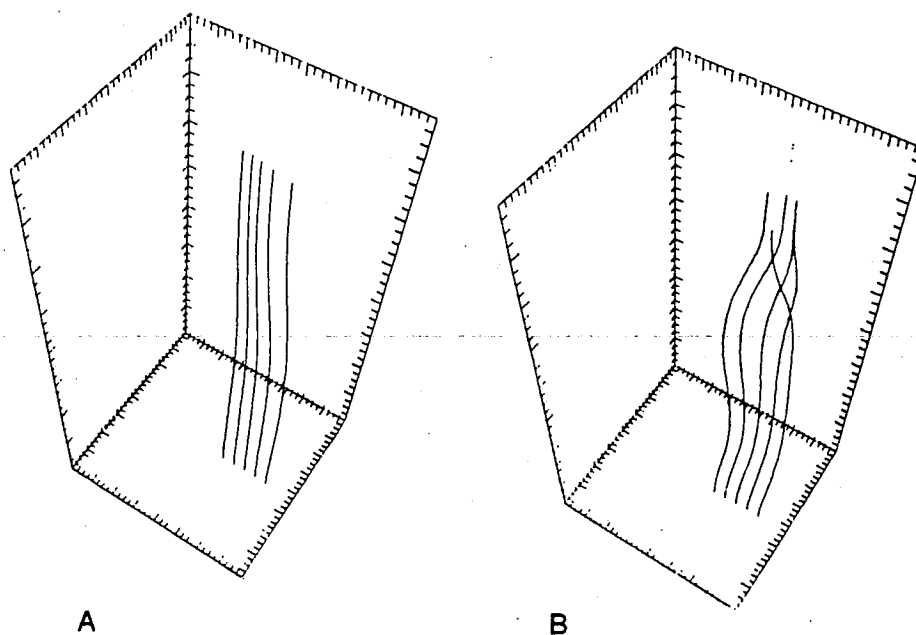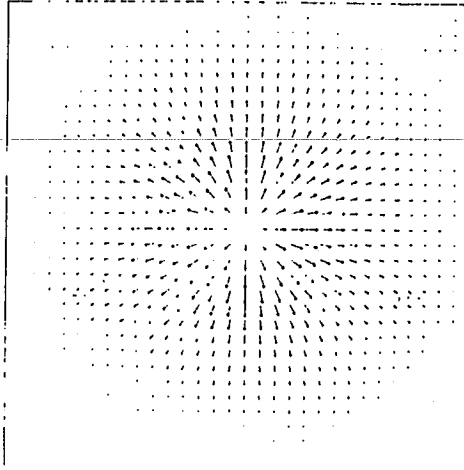
Figure 4.4 Perspective view of five radially distributed magnetic field lines at time=10 ω_{pe}^{-1} (A) and at time=200ω_{pe}^{-1} (B), shows a twisting of the magnetic field developing.

A $E_{LX} - E_{LY}$ $K_Z = 1$ $TIME = 200.00$
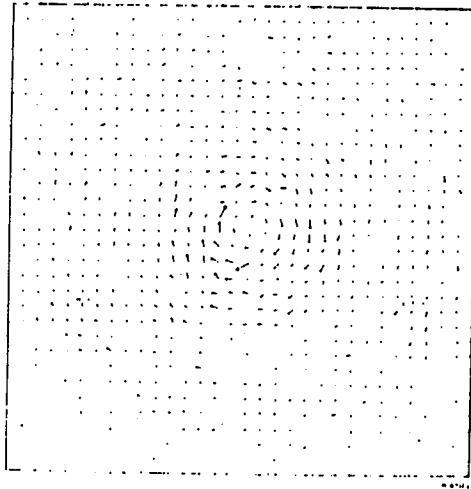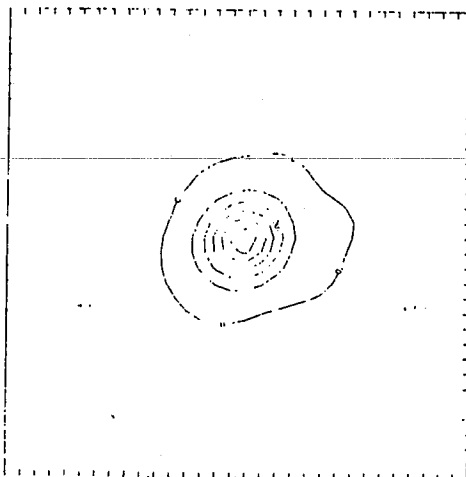

B $J_{IX} - J_{IY}$ $K_Z = 1$ $TIME = 200.00$

Figure 4.5 Vector diagrams of $E_{Lx} - E_{Ly}$ (A) with $k_z = 1 \times \frac{2\pi}{L_z}$ and ion flow (B) with $k_z = 1 \times \frac{2\pi}{L_z}$ at time$=200\omega_{pe}^{-1}$ for Case 1.

A $J_Z\ Z = 400.00\ TIME = 200.00$

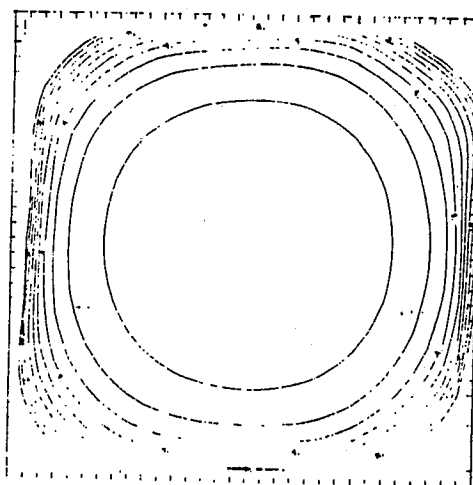B $B_\theta\ Z = 400.00\ TIME = 200.00$
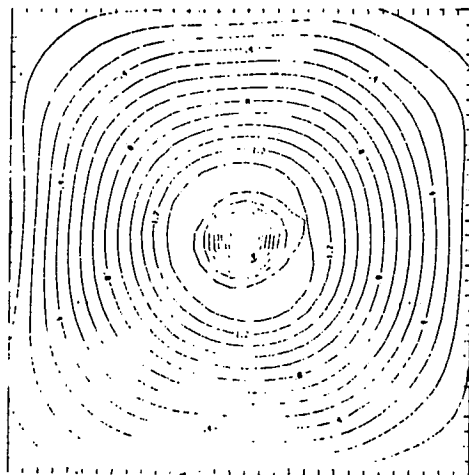
C $Q\ Z = 400.00\ TIME = 200.00$

Figure 4.6 Contours of J_z (A), B_θ (B), and q (C) in a cross sectional slice at $z = 400\Delta$ at time$=200\omega_{pe}^{-1}$ for Case 1.

netic fields in terms of the local rotational transform (angle) $\iota(r,z)$ and its associated so-called safety factor $q(r,z) = 2\pi/\iota$ locally defined as

$$q(r,z) = \frac{rB_z}{RB_\theta(\mathbf{x})},$$

where $R = L_z/2\pi$. Its contours are illustrated in Fig. 4.6(c). Here the usual definition of the (global) safety factor $q(r)$ and rotational transform $\iota(r)$ is independent of z, while the present ones are locally defined quantities for convenience. Since the twist is a function of z, the "rotational transform" and the safety factor are functions of z and are thus local (z) quantities. When q is, for example, 3 at $z=z_0$, the magnetic field is spiraling in the azimuthal direction with a pitch of $3L_z$. This would amount to a winding in the poloidal direction of the particular field line once while winding three times in the toroidal direction (in the periodicity of z) if this local $q=3$ was held for all z. Such a local q is depicted in Fig. 4.6(c). From Shafranov's theory[39] the kink instability is expected when q becomes less than unity. The results presented in Fig 4.7 for the electric field and flow pattern and in Fig. 4.8 for the azimuthal magnetic field, local q and current due to this magnetic field are for time $400\omega_{pe}^{-1}$ and in similarly in Figures 4.9 and 4.10 for time $800\omega_{pe}^{-1}$. As the twisting continues, the magnetic field lines become more wrapped showing a wider area with $q < 1$ (Fig. 4.8(c)). Figure 4.8(b) shows an $m=1$ distortion as exemplified by a crescent-shaped island and by a dipole structure. At this point it turns out that the system has achieved its maximum twist. It seems, in fact, that at this time the strong anticipated kink mode sets in, although the above conjecture is based on the analysis of the locally defined q. This strong kink mode makes the plasma unstable and shows a turbulent plasma motion. At $t=800\omega_{pe}^{-1}$, the flow pattern is re-established and the central structure of B_θ indicate that the plasma has somewhat relaxed. The time histories (Fig. 4.11) correlate well with the

magnetic field energy undergoing rapid growth until about time $400\omega_{pe}^{-1}$ and then decreasing such that the energy stored in the magnetic field at time $800\omega_{pe}^{-1}$ is nearly the same as at the earlier time of $200\omega_{pe}^{-1}$. The growth of the electron kinetic energy is seen to occur at the same times as the growth of the magnetic field energy.

A second simulation differs from the first case by having a reduced magnitude of the applied radial electric field, $eE_{r0}/m\omega_{pe}^2\Delta = 0.2$. Figures 4.12 and 4.13 are for $t = 200\omega_{pe}^{-1}$. The velocity field seen in Fig 4.12(a) is not as clearly organized at $t = 200\omega_{pe}^{-1}$ as the previous case. The contour plots of $\mathbf{J}_z$, Fig. 4.12(b) have a maximum contour level of 32.0, down almost an order of magnitude from Case 1. The peaking of the current is, however, still clearly visible. The n=1 component of the electric field is shown in Fig. 4.13(a). The contoured slice at $z = 400$ of the azimuthal component of the magnetic field shown in Fig. 4.13(b) has a much smaller regions enclosed by the q=1 contour seen in Fig. 4.13(c). At $t = 500\omega_{pe}^{-1}$ the diagrams of Fig. 4.14 and 4.15 show behavior similar to that of Case 1. The perspective field line diagram in Fig. 4.16 shows the field line twist at $t = 500\omega_{pe}^{-1}$ in (a) and a relaxation in (b) at $t = 800\omega_{pe}^{-1}$. The velocity field (Fig. 4.17(a)) and the n=1 vector field diagram in Fig. 4.18(b) for the electric field show m=1 structure retained as the field is relaxing. In Fig. 4.17(b), $\mathbf{J}_z$ is seen to be highly localized and it's magnitude comparable to that of Case 1. The contour plots of the azimuthal magnetic field (Fig. 4.18(b) and it's associated q contours (Fig. 4.18(c)) also show the m=1 structure. The energy time histories show a reduced magnitude especially in the first peak of the magnetic field energy as seen in Fig. 4.19.

A third simulation differs from the first case by having the radial dependence of the electric field vary as sin^2 (or $\epsilon = 2$) instead of sin

$A \quad E_{LX} - E_{LY} \ K_Z = 1 \ TIME = 400.00$
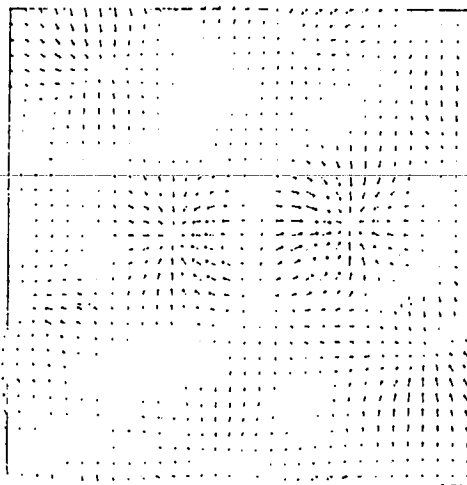
$B \quad J_{IX} - J_{IY} \ K_Z = 1 \ TIME = 400.00$

Figure 4.7 Vector diagrams of $E_{Lx} - E_{Ly}$ (A) with $k_z = 1 \times \frac{2\pi}{L_z}$ and ion flow (B) with $k_z = 1 \times \frac{2\pi}{L_z}$ at time=$400\omega_{pe}^{-1}$ for Case 1.

A $J_Z\,Z = 400.00\,TIME = 400.00$

B $B_\theta\,Z = 400.00\,TIME = 400.00$

C $Q\,Z = 400.00\,TIME = 400.00$

Figure 4.8 Contours of J_z (A), B_θ (B), and q (C) in a cross sectional slice at $z = 400\Delta$ at time=$400\omega_{pe}^{-1}$ for Case 1.

A $E_{LX} - E_{LY}$ $K_Z = 1$ $TIME = 800.00$
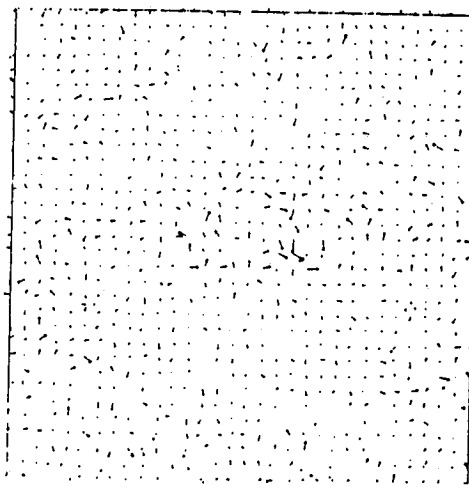
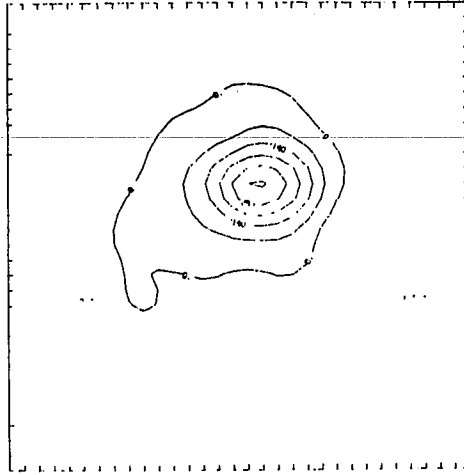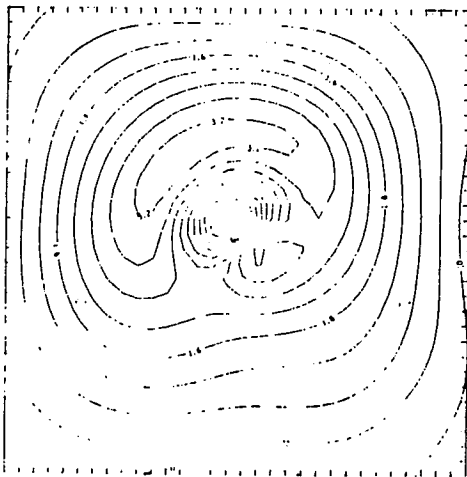**B** $J_{IX} - J_{IY}$ $K_Z = 1$ $TIME = 800.00$
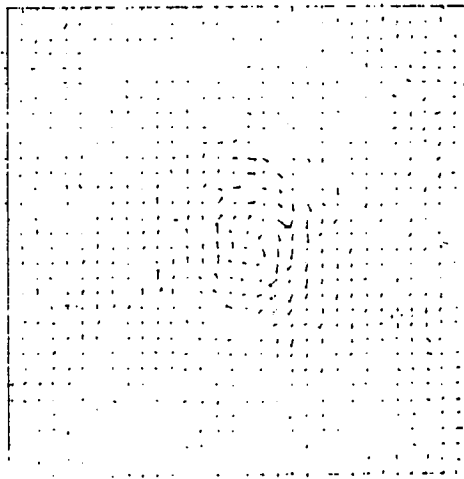
Figure 4.9 Vector diagrams of $E_{Lx} - E_{Ly}$ (A) with $k_z = 1 \times \frac{2\pi}{L_z}$ and ion flow (B) with $k_z = 1 \times \frac{2\pi}{L_z}$ at time=$800\omega_{pe}^{-1}$ for Case 1.

$A \quad J_Z \, Z = 400.00 \, TIME = 800.00$

$B \quad B_\theta \, Z = 400.00 \, TIME = 800.00$

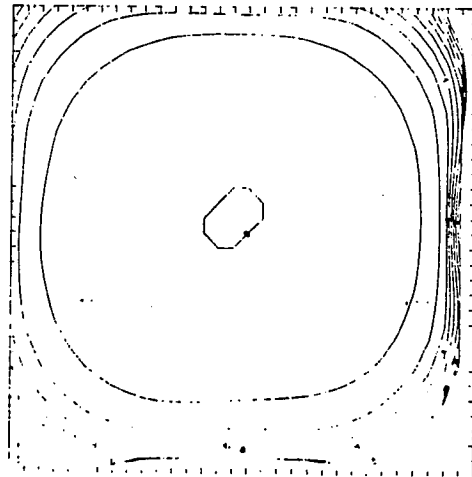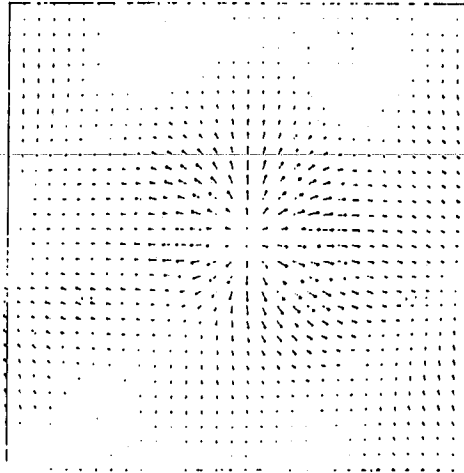$C \quad Q \, Z = 400.00 \, TIME = 800.00$
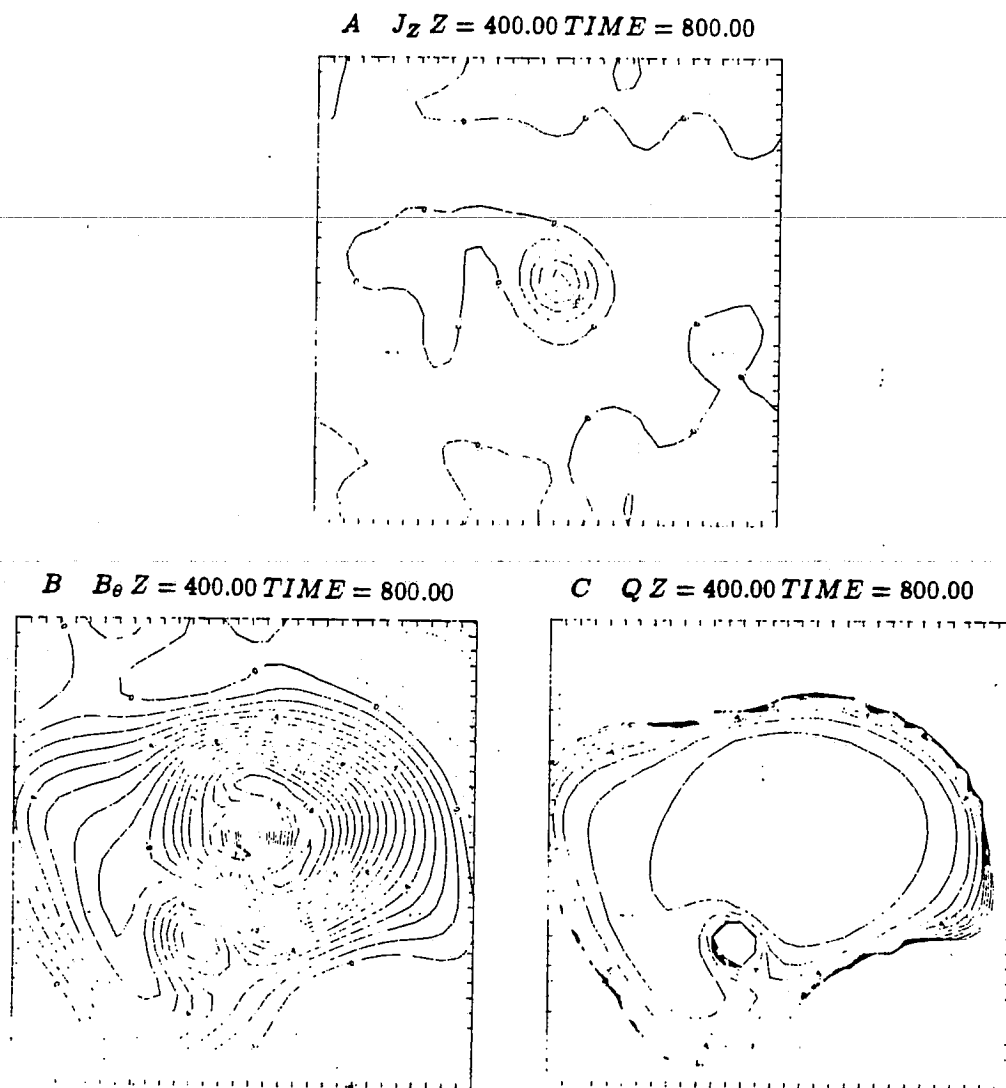
Figure 4.10 Contours of J_z(A), B_θ(B), and q (C) in a cross sectional slice at $z = 400\Delta$ at time=$800\omega_{pe}^{-1}$ for Case 1.
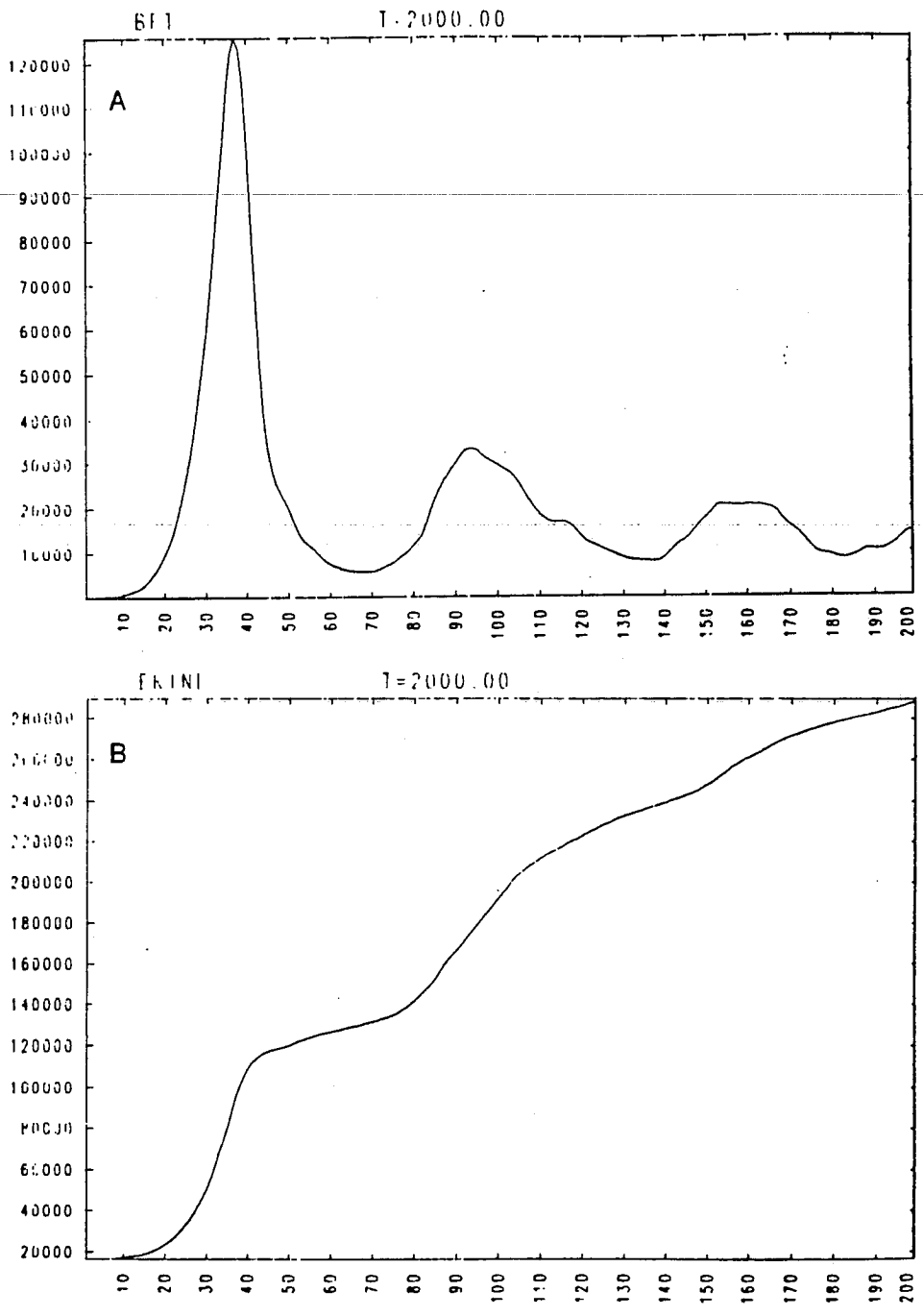
Figure 4.11 Time histories of the magnetic field energy (A) and the electron kinetic energy (B) for Case 1.

$$A \quad J_{IX} - J_{IY} \ K_Z = 1 \ TIME = 200.00$$
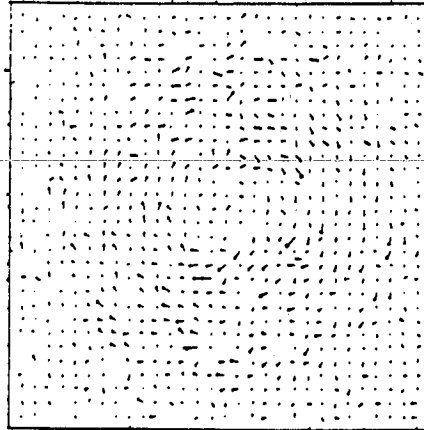
$$B \quad J_Z \ \underline{Z} = 400.00 \ TIME = 200.00$$

Figure 4.12 Vector diagram of the ion flow with $k_z = 1 \times \frac{2\pi}{L_z}$ (A) and contours of J_z (B) in a cross sectional slice at $z = 400\Delta$ at time=$200\omega_{pc}^{-1}$ for Case 2.

A $E_{LX} - E_{LY}$ $K_Z = 1$ $TIME = 200.00$

B B_θ $Z = 400.00$ $TIME = 200.00$ C Q $Z = 400.00$ $TIME = 200.00$

Figure 4.13 Vector diagrams of $E_{Lx} - E_{Ly}$ (A) with $k_z = 1 \times \frac{2\pi}{L_z}$ and contours of B_θ (B), and q (C) in a cross sectional slice at $z = 400\Delta$ at time=$200\omega_{pe}^{-1}$ for Case 2.

$A \quad J_{IX} - J_{IY} \ K_Z = 1 \ TIME = 500.00$

$B \quad J_Z \ Z = 400.00 \ TIME = 500.00$
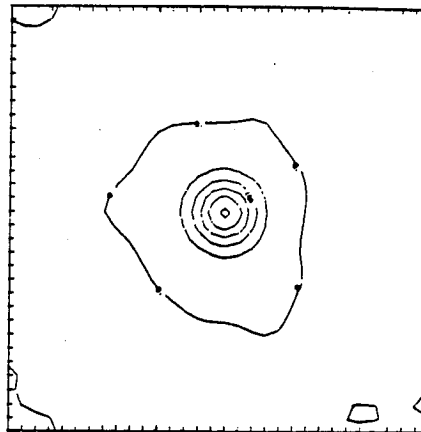
Figure 4.14 Vector diagram of the ion flow with $k_z = 1 \times \frac{2\pi}{L_z}$ (A) and contours of J_z (B) in a cross sectional slice at $z = 400\Delta$ at time=$500\omega_{pe}^{-1}$ for Case 2.

A $E_{LX} - E_{LY}\ K_Z = 1\ TIME = 500.00$
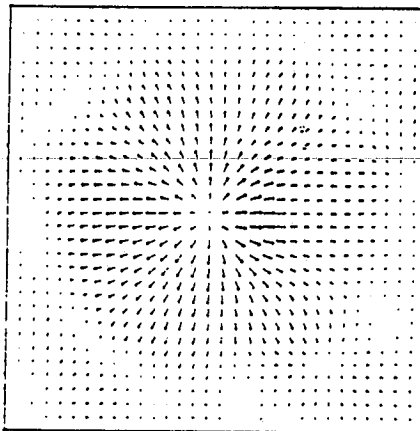
B $B_\theta\ Z = 400.00\ TIME = 500.00$
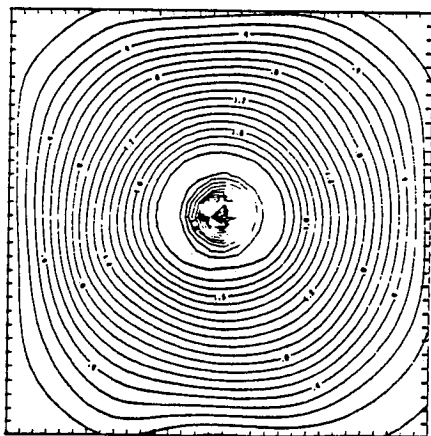
C $Q\ Z = 400.00\ TIME = 500.00$

Figure 4.15 Vector diagrams of $E_{Lx} - E_{Ly}$ (A) with $k_z = 1 \times \frac{2\pi}{L_z}$ and contours of B_θ (B), and q (C) in a cross sectional slice at $z = 400\Delta$ at time=$500\omega_{pe}^{-1}$ for Case 2.
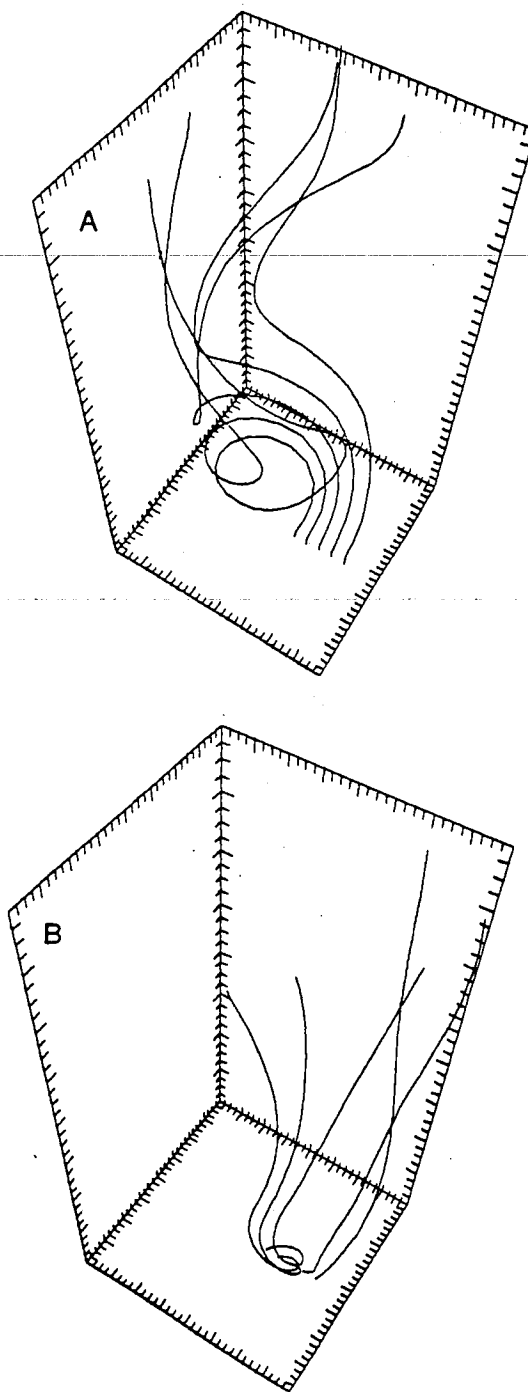
Figure 4.16 Perpective view of magnetic field lines at time=$500\omega_{pe}^{-1}$ (A) and at time=$800\omega_{pe}^{-1}$ (B) for Case 2.

A $J_{IX} - J_{IY}$ $K_Z = 1$ $TIME = 800.00$
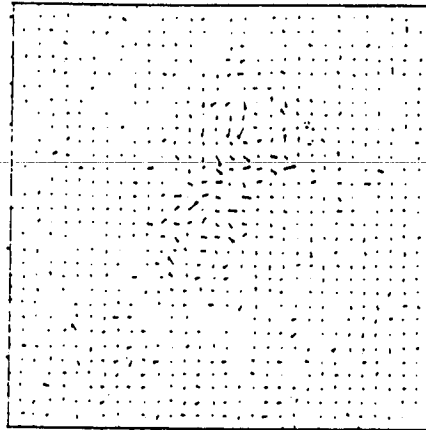
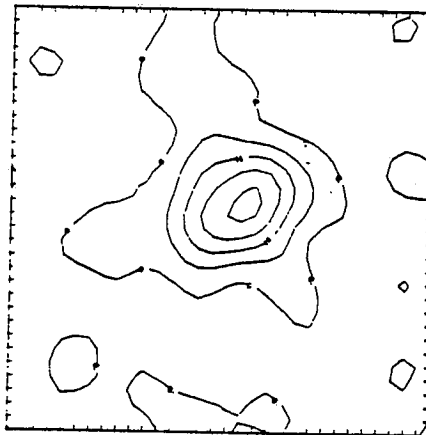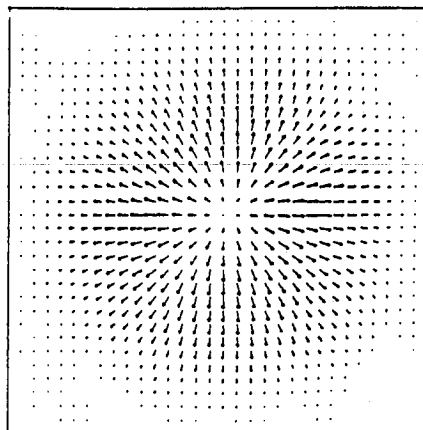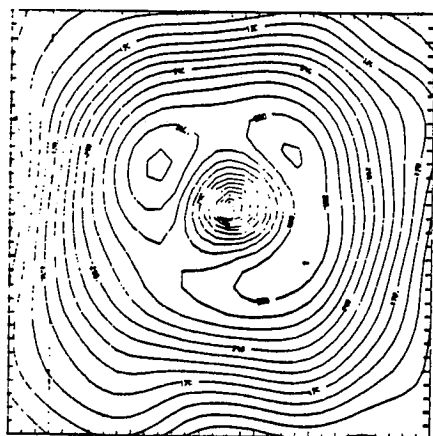
B J_Z $Z = 400.00$ $TIME = 800.00$
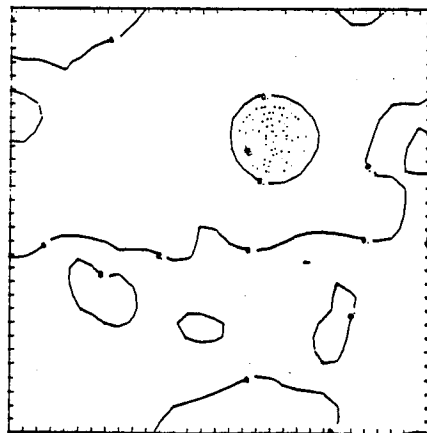
Figure 4.17 Vector diagram of the ion flow with $k_z = 1 \times \frac{2\pi}{L_z}$ (A) and contours of J_z (B) in a cross sectional slice at $z = 400\Delta$ at time$=800\omega_{pe}^{-1}$ for Case 2.

A $E_{LX} - E_{LY}$ $K_Z = 1\, TIME = 800.00$
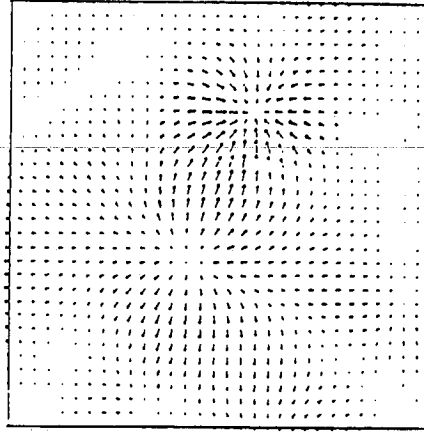
B B_θ $Z = 400.00\, TIME = 800.00$

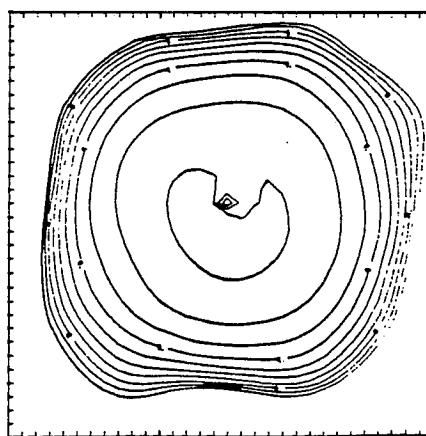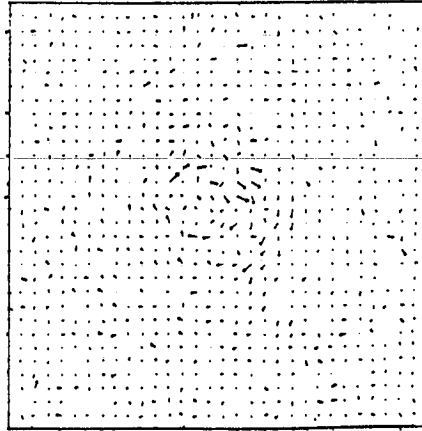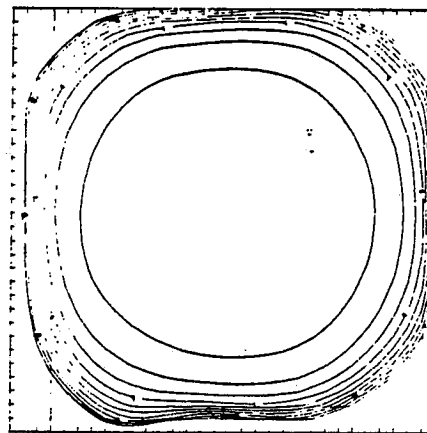C Q $Z = 400.00\, TIME = 800.00$

Figure 4.18 Vector diagrams of $E_{Lz} - E_{Ly}$ (A) with $k_z = 1 \times \frac{2\pi}{L_z}$ and contours of B_θ (B), and q (C) in a cross sectional slice at $z = 400\Delta$ at time$=800\omega_{pe}^{-1}$ for Case 2.
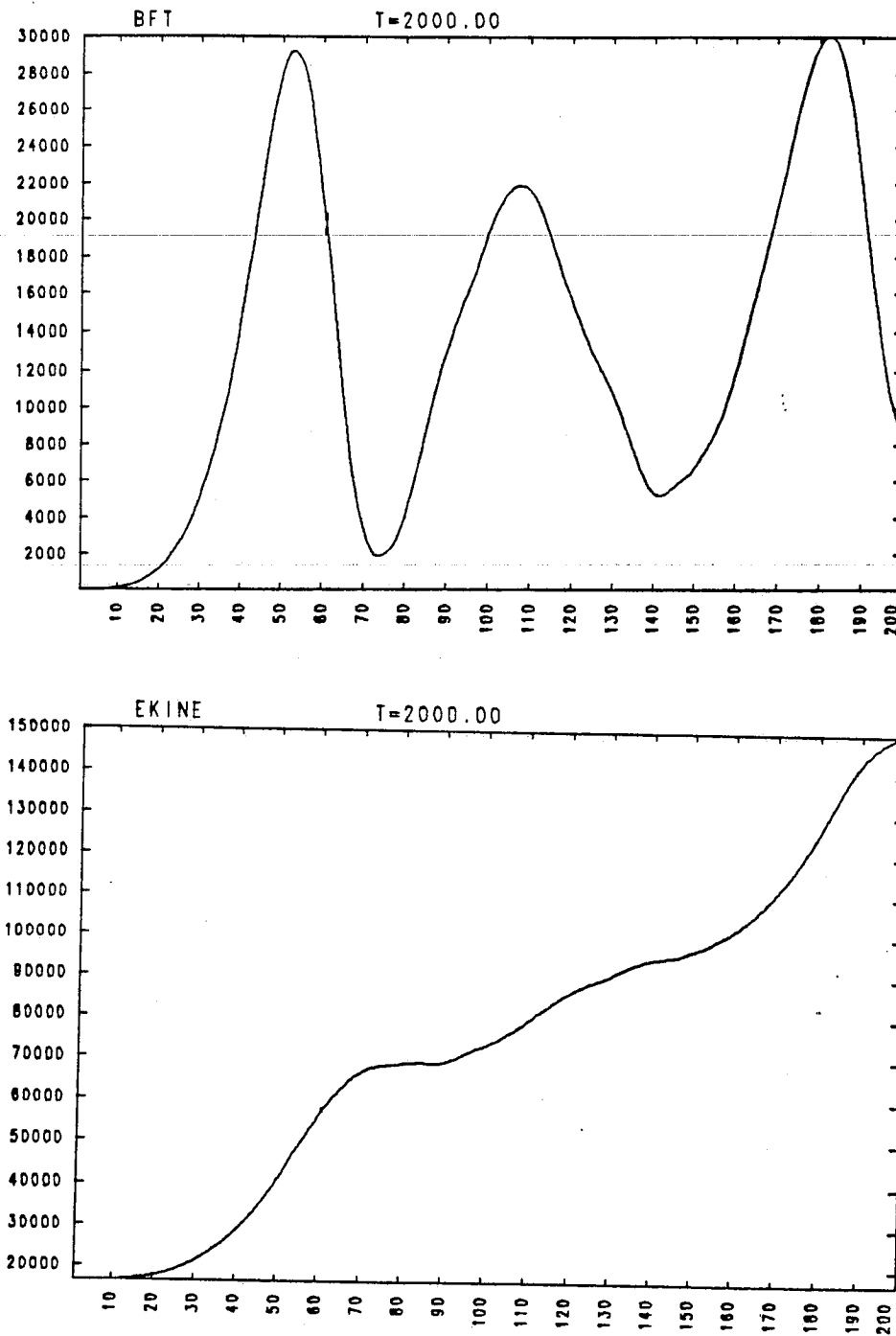
Figure 4.19 Time histories of the magnetic field energy (A) and the electron kinetic energy (B) for Case 2.

(or $\epsilon = 1$). The results are essentially the same as Case 1. A perspective view of magnetic field lines is shown in Fig. 4.20 for times $t = 10\omega_{pe}^{-1}$ (a), $t = 100\omega_{pe}^{-1}$ (b), and $t = 200\omega_{pe}^{-1}$ (c).

4.3 Discussion

The pinching of plasma near $r = 0$ and increase of the plasma density are not inconsistent with Zweibel and Boozer's twist equilibrium[49]. Also pinching and twisting were observed in a $2D$ azimuthally symmetric MHD simulation by Steinolfson and Tajima[54], consistent with the present result. In their runs when the field lines wrapped around azimuthally more than one revolution, there appears a bifurcation of magnetic field configuration, yielding a field reversed configuration that resembles Strauss and Van Hoven's runs in a $2D$ azimuthally symmetric MHD simulation. In the latter[55] the initial toroidal current J_z is given and thus the initial poloidal flux ψ is imposed, which undergoes the $m = 0$ tearing.

In our $3D$ study, however, the system is allowed to undergo motions with another degree of freedom (a third dimension, i.e. the azimuthal direction in this case). Instead of the system being forced to behave with $m=0$ distortion and bifurcation, the plasma column now developes azimuthal modulation, exhibiting the (local) kink mode. By this azimuthal symmetry breaking the system is now allowed to reach a new magnetic configuration which should have lower free energy than those observed by Steinolfson and Tajima[54] and Strauss and Van Hoven[55].
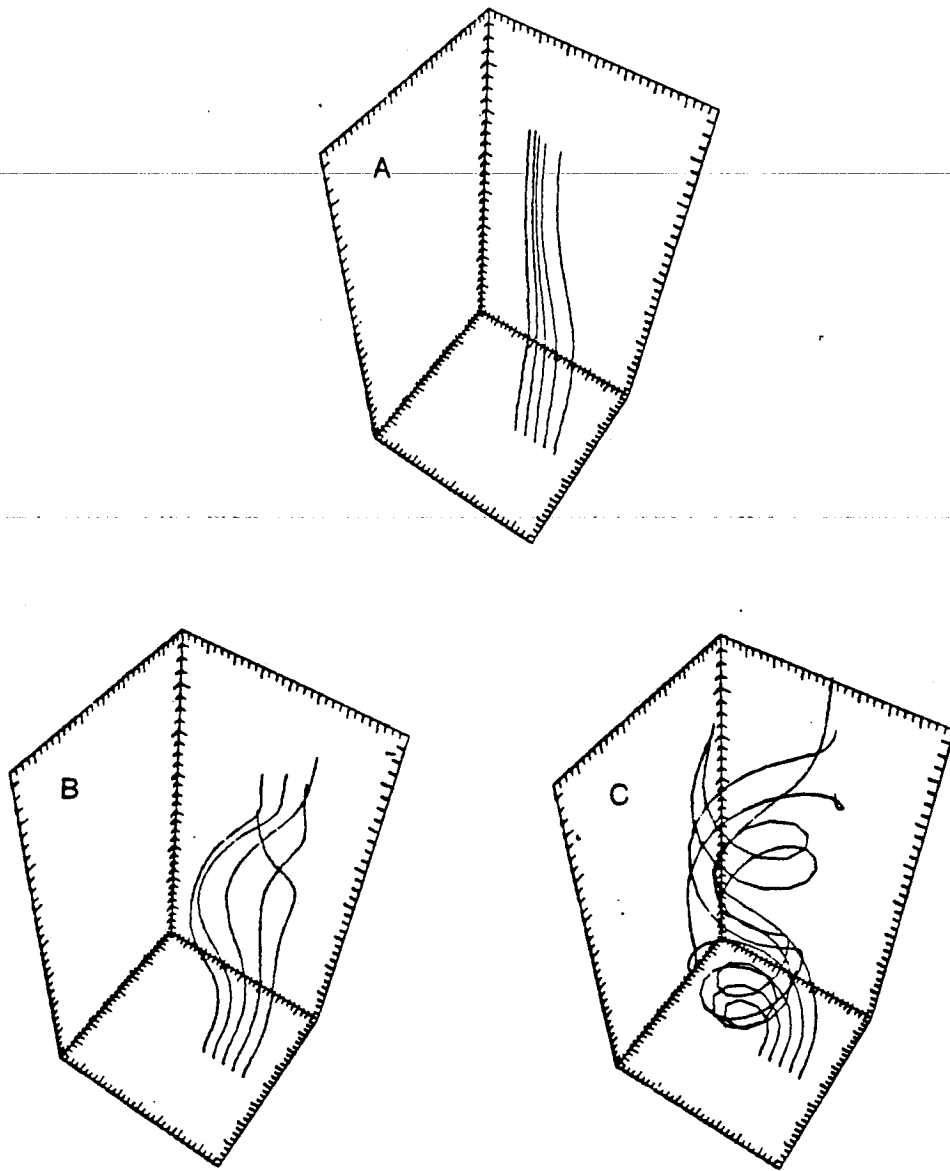
Figure 4.20 Perspective view of magnetic field lines at time t=10 ω_{pe}^{-1} (A), at time t=100 ω_{pe}^{-1} (B), and at time t=200 ω_{pe}^{-1} (C) for Case 3.

CHAPTER 5.
CONCLUSIONS

We have developed a computational model which extends the applicability of particle simulation to lower frequencies with the inclusion of three dimensional geometry. This allows us much needed flexibility to tackle classes of problems which are important but never before tried because of their computational difficulty. The approximations of a Darwin radiationless formulation of the electromagnetic field equations and of guiding center electrons allow a relaxation of the constraint on the time step thereby allowing us to simulate longer time scale processes. The inclusion of the third dimension obviously permits investigations of phenomena in the full three dimensions. However, in order to carry out meaningful simulations within feasible computational resources, it behooves us to separate the treatment of fields and particles along the external magnetic field and across it. In the third dimension, an eigenfunction expansion is adopted, while in the cross field directions a standard gridded technique is used. A development of this model and tests thereof are presented in Chapter 2. These tests show results for the thermal excited properties of a homogeneous magnetized plasma in agreement with theoretical expectations for both the spectra and distribution of energy among modes.

Two of the plasma processes involving the bulk current redistribution and release of magnetic energy into kinetic which occur on the order of the Alfvén time scale, the kink instability and the coalescense instability of multiple current channels, have been simulated. Two dimensional electromagnetic particle simulations explain some aspects of the physics but are limited by the restrictions of: (1) single helicity and (2) the short time step required. Within this two dimensional framework, the tearing and co-

alescense instabilities provide some insight into the basic reconnection processes. The kink instability, which is also a current driven instability, requires the inclusion of three dimensions for physically interesting results. The simulation method described in this dissertation provides a tool which allows kink mode development due to its three dimensional nature and also allows simulation of the low frequency time scales of interest. The simulation code which we have developed thus appears able to model the physics associated with kink-type instabilities, showing kink development not inconsistent with Shafranov's linear theory.

This tool was then applied to the study of twist-kink modes in a plasma column. As a twisting of the plasma column continues, we observe that the plasma is constricted toward the center of the loop and the axial current density also increases in this vicinity. As the current density continues to increase further, the poloidal field becomes sufficiently large so that the field line azimuthally rotates more than one revolution within the length of the loop plasma. Then the plasma column is observed to kink. Relaxation of the twist then follows and the process repeats as the twist continues to be applied. The observation of this kink induced by twist is the major finding of this dissertation. The pinching of plasma near $r = 0$ and increase of the plasma density are not inconsistent with Zweibel and Boozer's twist equilibrium result[49].

The inclusion of the third dimension in the present study makes a marked difference from previous two dimensional results. In Steinolfson, et al.[54], the simulation system is two dimensional (MHD) in the r and z directions. As a result of an applied twist, the current, J_z, increases and constriction of the axial magnetic field toward the center are observed similar to the present study. As further twisting is applied, the 2D plasma exhibits

a reversal of the axial magnetic field within a cylindrical shell apparently because of the azimuthal symmetry constraint. Thus we suspect that the difference in development beyond $\hat{t}(z) > 1$ is due to the additional freedom in the 3D model to break the symmetry which allows the system to relax via a "lower energy route".

Twisting of a plasma column appears in various physical situations. On the solar surface during the preflare stage, active regions exhibit photospheric twist motion at the feet of a coronal loop several hours prior to the onset of the flare. We surmise that such a preflare motion stores magnetic energy through the axial current induction with the coronal plasma eventually becomes unstable releasing this energy into other forms through the mechanism observed in our simulations. In a tandem mirror, the addition of end cells into a mirror geometry creates an axial variation in the ambipolar potential profile which leads to a differential twisting of the plasma column.

APPENDIX A.

SOLUTION FOR THE TRANSVERSE ELECTRIC FIELD

The details of deriving the method of solution for the transverse electric field are presented in this appendix. The method of solution follows the same procedure as outlined in Busnardo-Neto et. al.[11] The transverse electric field is to be calculated from the time derivative of the transverse current which is to be determined via the particle equations of motion.

$$\nabla^2 \mathbf{E}_T = \frac{4\pi}{c^2} \left(\frac{\partial \mathbf{J}}{\partial t} \right)_T \qquad (A1)$$

For finite size particles the current due to plasma particles is

$$\mathbf{J}(\mathbf{x}) = q_p \left[\sum_{j=1}^{N_0} \mathbf{v}_j S\left(\mathbf{x} - \mathbf{x}_j\right) - \sum_{i=1}^{N_0} \mathbf{v}_i S\left(\mathbf{x} - \mathbf{x}_i\right) \right]; \qquad (A2)$$

where: The j sum is over the electrons, the i sum is over the ions, $S(\mathbf{x})$ is the finite size particle form factor, $q_p = e n_0 V'/N_0$, n_0 is the particle density, N_0 is the total number of quasiparticles of one species, V' is the volume containing particles, and the charge on the electron is defined here as positive. The partial time derivative of the current as seen in the particle's reference frame is

$$\frac{\partial \mathbf{J}(\mathbf{x})}{\partial t} = q_p \left\{ \sum_j \left[\frac{\partial}{\partial t} \mathbf{v}_j S(\mathbf{x} - \mathbf{x}_j) + \mathbf{v}_j \frac{\partial}{\partial t} \mathbf{x}_j \cdot \frac{\partial}{\partial \mathbf{x}_j} S(\mathbf{x} - \mathbf{x}_j) \right] \right.$$

$$\left. - \sum_i \left[\frac{\partial}{\partial t} \mathbf{v}_i S(\mathbf{x} - \mathbf{x}_i) + \mathbf{v}_i \frac{\partial}{\partial t} \mathbf{x}_i \cdot \frac{\partial}{\partial \mathbf{x}_i} S(\mathbf{x} - \mathbf{x}_i) \right] \right\}. \qquad (A3)$$

The time derivative of the perpendicular component of the electron velocity may be neglected due to a guiding center massless electron approximation,

$$\frac{\partial \mathbf{J}(\mathbf{x})}{\partial t} = q_p \left\{ \sum_{j=1}^{N_0} \frac{\partial}{\partial t} \mathbf{v}_{\|j} S(\mathbf{x} - \mathbf{x}_j) - \sum_{i=1}^{n_0} \frac{\partial}{\partial t} \mathbf{v}_i S(\mathbf{x} - \mathbf{x}_i) \right.$$

$$\left. - \left[\sum_{j=1}^{N_0} \mathbf{v}_j \mathbf{v}_j \cdot \nabla S(\mathbf{x} - \mathbf{x}_j) - \sum_{i=1}^{N_0} \mathbf{v}_i \mathbf{v}_i \cdot \nabla S(\mathbf{x} - \mathbf{x}_i) \right] \right\}. \qquad (A4)$$

Next the particle equations of motion are to be utilized. The equation of motion for a point particle is given by

$$\frac{d\mathbf{v}_\alpha}{dt} = \frac{e}{m}\left(\mathbf{E} + \frac{1}{c}\mathbf{v}_\alpha \times \mathbf{B}\right).$$

The inclusion of finite size particle effects makes the equation for the ion motion

$$\frac{\partial \mathbf{v}_i}{\partial t} = \frac{d\mathbf{v}_i}{dt} = -\frac{q_p}{m_p}\frac{m}{M}\int S(\mathbf{x}' - \mathbf{x}_i)\left[\mathbf{E}(\mathbf{x}') + \frac{\mathbf{v}_i}{c}\times\mathbf{B}(\mathbf{x}')\right]d\mathbf{x}'. \qquad (A5)$$

The equation for the parallel component of the electron motion becomes

$$\frac{\partial \mathbf{v}_{\|j}}{\partial t} = \frac{d\mathbf{v}_{\|j}}{dt} = \frac{q_p}{m_p}\int S(\mathbf{x}' - \mathbf{x}_j)\mathbf{E}_\|(\mathbf{x}')d\mathbf{x}'. \qquad (A6)$$

The perpendicular electron motion is assumed to be dominated by the guiding center $\mathbf{E}\times\mathbf{B}$ motion

$$\mathbf{v}_{\perp j} = \frac{c\left[\int\mathbf{E}(\mathbf{x}')S(\mathbf{x}' - \mathbf{x}_j)d\mathbf{x}'\right]\times\left[\int\mathbf{B}(\mathbf{x}')S(\mathbf{x}' - \mathbf{x}_j)d\mathbf{x}'\right]}{\left[\int\mathbf{B}(\mathbf{x}')S(\mathbf{x}' - \mathbf{x}_j)d\mathbf{x}'\right]^2}. \qquad (A7)$$

The approximation is made that the magnetic field varies little over the region containing the finite size particle, $a/L_s \ll 1$ where L_s is a typical magnetic field shear length. The perpendicular velocity of the j'th electron can then be described as

$$\mathbf{v}_{\perp j} \simeq -c\frac{\hat{\mathbf{b}}(\mathbf{x}_j)}{B(\mathbf{x}_j)}\times\left[\int\mathbf{E}(\mathbf{x}')S(\mathbf{x}' - \mathbf{x}_j)d\mathbf{x}'\right]. \qquad (A8)$$

For the solution of Eq. (A4), we neglect $\partial\mathbf{v}_{\perp j}/\partial t$ since it is zero to first order in ω/Ω and neglect the polarization drift since it is second order in ω/Ω. Upon substitution of (A5) and (A6) into Eq. (A4) we obtain

$$\frac{\partial\mathbf{J}(\mathbf{x})}{\partial t} = \frac{q_p^2}{m_p}\sum_{j=1}^{N_0}S(\mathbf{x} - \mathbf{x}_j)\int S(\mathbf{x}' - \mathbf{x}_j)\mathbf{E}_\|(\mathbf{x}')d\mathbf{x}$$

$$+ \frac{q_p^2}{m_p}\sum_{i=1}^{n_0}S(\mathbf{x} - \mathbf{x}_i)\int S(\mathbf{x}' - \mathbf{x}_j)\left[\mathbf{E}(\mathbf{x}') + \frac{\mathbf{v}_i}{c}\times\mathbf{B}(\mathbf{x}')\right]d\mathbf{x}$$

$$+ q_p\nabla\cdot\left[\sum_{j=1}^{N_0}\mathbf{v}_j\mathbf{v}_jS(\mathbf{x} - \mathbf{x}_j) - \sum_{i=1}^{N_0}\mathbf{v}_i\mathbf{v}_iS(\mathbf{x} - \mathbf{x}_i)\right]. \qquad (A9)$$

Equation (A9) is the sum of three terms. Look at the second term. Define

$$\Lambda(\mathbf{x}) \equiv \frac{m}{M} \sum_{i=1}^{N_0} S(\mathbf{x} - \mathbf{x}_i) \int S(\mathbf{x}' - \mathbf{x}_i) \left[\mathbf{E}(\mathbf{x}') + \frac{\mathbf{v}_i}{c} \times \mathbf{B}(\mathbf{x}') \right] d\mathbf{x}. \quad (A10)$$

Fourier expand the shape factor

$$S(\mathbf{x}' - \mathbf{x}_i) = \sum_{\mathbf{k}'} S(\mathbf{k}') e^{i\mathbf{k}' \cdot (\mathbf{x} - \mathbf{x}_i)}$$

and similarly for the quantity in the brackets. Substitution back into Eq. (A10) gives

$$\Lambda(\mathbf{x}) = \frac{m}{M} \sum_{i=1}^{N_0} S(\mathbf{x} - \mathbf{x}_i)$$
$$\int \sum_{\mathbf{k}'} S(\mathbf{k}') e^{i\mathbf{k}' \cdot (\mathbf{x} - \mathbf{x}_i)} \sum_{\mathbf{k}''} \left[\mathbf{E}(\mathbf{k}'') + \frac{\mathbf{v}_i}{c} \times \mathbf{B}(\mathbf{k}'') \right] e^{i\mathbf{k}'' \cdot \mathbf{x}'} d\mathbf{x}.$$

Rearranging the exponentials

$$\Lambda(\mathbf{x}) = \frac{m}{M} \sum_{i=1}^{N_0} S(\mathbf{x} - \mathbf{x}_i)$$
$$\sum_{\mathbf{k}'} \sum_{\mathbf{k}''} S(\mathbf{k}') \left[\mathbf{E}(\mathbf{k}'') + \frac{\mathbf{v}_i}{c} \times \mathbf{B}(\mathbf{k}'') \right] e^{i\mathbf{k}' \cdot (\mathbf{x} - \mathbf{x}_i)} \int e^{i(\mathbf{k}' + \mathbf{k}'') \cdot \mathbf{x}'} d\mathbf{x}. \quad (A11)$$

Note that the Kronecker delta appears

$$\delta(\mathbf{k} - \mathbf{k}') = \frac{1}{2\pi} \int_{-\infty}^{\infty} e^{i(\mathbf{k} - \mathbf{k}') \cdot \mathbf{x}} d\mathbf{x}$$

which will eliminate the integral. Also Fourier expand $S(\mathbf{x} - \mathbf{x}_i)$.

$$\Lambda(\mathbf{x}) = \frac{m}{M} \sum_{i=1}^{N_0} \sum_{\mathbf{k}} S(\mathbf{k}) e^{i\mathbf{k} \cdot (\mathbf{x} - \mathbf{x}_i)}$$
$$\sum_{\mathbf{k}'} \sum_{\mathbf{k}''} S(\mathbf{k}') \left[\mathbf{E}(\mathbf{k}'') + \frac{\mathbf{v}_i}{c} \times \mathbf{B}(\mathbf{k}'') \right] e^{-i\mathbf{k}' \cdot \mathbf{x}_i} \delta(\mathbf{k}' + \mathbf{k}'')(2\pi)^n \quad (A12)$$

Use the delta function to collapse one sum,

$$\mathbf{A}(\mathbf{x}) = V\frac{m}{M}\sum_{i=1}^{N_0}\sum_{\mathbf{k}} S(\mathbf{k})e^{i\mathbf{k}\cdot(\mathbf{x}-\mathbf{x}_i)}$$

$$\sum_{\mathbf{k}''} S(-\mathbf{k}'')\left[\mathbf{E}(\mathbf{k}'')+\frac{\mathbf{v}_i}{c}\times\mathbf{B}(\mathbf{k}'')\right]e^{i\mathbf{k}''\cdot\mathbf{x}_i}, \qquad (A13)$$

where V is the volume containing the fields.

Since we want to get away from individual particle quantities and work on a (two dimensional) grid, collect the terms with an i dependence so that we can do a Taylor expansion about the nearest grid point.

$$\mathbf{A}(\mathbf{x}) = V\frac{m}{M}\sum_{\mathbf{k}}\sum_{\mathbf{k}} S(-\mathbf{k}'')e^{i\mathbf{k}\cdot\mathbf{x}}$$

$$\sum_{i=1}^{N_0}\left[\mathbf{E}(\mathbf{k}'')+\frac{\mathbf{v}_i}{c}\times\mathbf{B}(\mathbf{k}'')\right]e^{i(\mathbf{k}''-\mathbf{k})\cdot\mathbf{x}_i} \qquad (A14)$$

Define $\mathbf{k}' = \mathbf{k} - \mathbf{k}''$ There are two sums over i in Eq. (A14),

$$\sum_{i=1}^{N_0} e^{-i\mathbf{k}'\cdot\mathbf{x}} \quad and \quad \sum_{i=1}^{N_0}\mathbf{v}_i e^{-i\mathbf{k}'\cdot\mathbf{x}}. \qquad (A15)$$

Rewrite the sums over i as a sum over all the particles whose closest two dimensional grid point is g and then a sum over all of these two dimensional grid points,

$$\sum_{i=1}^{N_0} \rightarrow \sum_{g}\sum_{i\in g}.$$

Look at the first of the two sums in Eq. (A15). Define a quantity, A,

$$A \equiv \sum_{i=1}^{N_0} e^{-i\mathbf{k}'\cdot\mathbf{x}} = \sum_{g}\sum_{i\in g} e^{-i\mathbf{k}'\cdot\mathbf{x}}. \qquad (A16)$$

For notational convience let $\mathbf{x} \equiv (\mathbf{x}_\perp, z)$ where $\mathbf{x}_\perp = (x,y)$. Expand A in a two dimensional Taylor series about the nearest grid point,

$$A = \sum_{g}\sum_{i\in g}\sum_{l=0}^{\infty}\frac{(\mathbf{x}_{\perp i}-\mathbf{x}_{\perp g})^l}{l!}\cdot\left(\frac{\partial}{\partial\mathbf{x}_{\perp g}}\right)^l e^{-i\mathbf{k}'\cdot\mathbf{x}_{gi}} \qquad (A17),$$

where the notation of $\mathbf{x}_{gi} \equiv (\mathbf{x}_{\perp g}, z_i)$ is used.

The implementation into a computer code truncates the sum over l at the dipole term and approximates the derivative using a centered finite difference scheme, the subtracted dipole scheme (SUDS). For the two dimensional expansion this is explicitly,

$$A = \sum_{g} \sum_{i \in g} \left[1 + (\mathbf{x}_{\perp i} - \mathbf{x}_{\perp g}) \cdot \frac{\partial}{\partial \mathbf{x}_{\perp g}} \right] e^{-i\mathbf{k}' \cdot \mathbf{x}_{gi}} \qquad (A18),$$

or in expanded form,

$$A = \sum_{m,n} \sum_{i \in m,n} \left[1 + (x_i - x_m)\frac{\partial}{\partial x}\bigg|_m (y_i - y_n)\frac{\partial}{\partial y}\bigg|_n \right] e^{-ik'_x x_m} e^{-ik'_y y_n} e^{-ik'_z z_i}$$

$$(A19).$$

Note that the z dependency is not expanded and retains an i dependence. The derivatives are approximated by centered finite differences,

$$\frac{\partial}{\partial x}\bigg|_m e^{-ik'_x x_m} \simeq \frac{e^{-ik'_x x_{m+1}} - e^{-ik'_x x_{m-1}}}{x_{m+1} - x_{m-1}} = \frac{e^{-ik'_x x_{m+1}} - e^{-ik'_x x_{m-1}}}{2\Delta},$$

and similarly for y,

$$\frac{\partial}{\partial y}\bigg|_n e^{-ik'_y y_n} \simeq \frac{e^{-ik'_y y_{n+1}} - e^{-ik'_y y_{n-1}}}{y_{n+1} - y_{n-1}} = \frac{e^{-ik'_y y_{n+1}} - e^{-ik'_y y_{n-1}}}{2\Delta}.$$

Substitute this into the expression for A.

$$A = \sum_{m,n} \sum_{i \in m,n} \bigg[e^{-ik'_x x_m} e^{-ik'_y y_n} e^{-ik'_z z_i}$$

$$+ \frac{(x_i - x_m)}{2} e^{-ik'_y y_n} e^{-ik'_z z_i} \left(e^{-ik'_x x_{m+1}} - e^{-ik'_x x_{m-1}} \right)$$

$$+ \frac{(y_i - y_n)}{2} e^{-ik'_x x_m} e^{-ik'_z z_i} \left(e^{-ik'_y y_{n+1}} - e^{-ik'_y y_{n-1}} \right) \bigg]. \qquad (A20)$$

Shift the dummy indicies term by term, for example,

$$\sum_{i \in m,n} \frac{x_i - x_m}{2\Delta} e^{-ik'_y y_n} e^{-ik'_z z_i} e^{-ik'_x x_{m+1}} =$$

$$\sum_{i \in m-1,n} \frac{x_i - x_{m-1}}{2\Delta} e^{-ik'_y y_n} e^{-ik'_z z_i} e^{-ik'_x x_m}.$$

Apply this shifting to all of the four terms required in Eq. (A20).

$$
\begin{aligned}
A = \sum_{m,n} e^{-ik'_\tau x_m} e^{-ik'_\nu y_n} \Bigg[& \sum_{i \in m,n} e^{-ik'_z z_i} \\
& + \sum_{i \in m-1,n} \frac{(x_i - x_{m-1})}{2} e^{-ik'_z z_i} - \sum_{i \in m+1,n} \frac{(x_i - x_{m+1})}{2} e^{-ik'_z z_i} \\
& + \sum_{i \in m,n-1} \frac{(y_i - y_{n-1})}{2} e^{-ik'_z z_i} - \sum_{i \in m,n+1} \frac{(y_i - y_{n+1})}{2} e^{-ik'_z z_i} \Bigg].
\end{aligned} \quad (A21)
$$

The term in [ ] is the (ion) number density, n_i for the particular k_z mode.

$$
A = \sum_{m,n} e^{-ik'_\tau x_m} e^{-ik'_\nu y_n} n_i(x_m, y_n, k'_z) \quad (A22)
$$

In vector notation,

$$
A = \sum_{m,n} e^{-ik'_\perp x_g} n_i(\mathbf{x}_g, k'_z) \quad (A23)
$$

Similarly, the second summation of Eq. (A15). Define $\mathbf{D}$,

$$
\mathbf{D} \equiv \sum_{i=1}^{N_0} \mathbf{v}_i e^{-ik' \cdot \mathbf{x}} = \sum_g \sum_{i \in g} \mathbf{v}_i e^{-ik' \cdot \mathbf{x}}. \quad (A24)
$$

The approximations and expansions proceed as for A.

$$
\begin{aligned}
\mathbf{D} = \sum_{m,n} e^{-ik'_\tau x_m} e^{-ik'_\nu y_n} \Bigg[& \sum_{i \in m,n} \mathbf{v}_i e^{-ik'_z z_i} \\
& + \sum_{i \in m-1,n} \frac{(x_i - x_{m-1})}{2} \mathbf{v}_i e^{-ik'_z z_i} - \sum_{i \in m+1,n} \frac{(x_i - x_{m+1})}{2} \mathbf{v}_i e^{-ik'_z z_i} \\
& + \sum_{i \in m,n-1} \frac{(y_i - y_{n-1})}{2} \mathbf{v}_i e^{-ik'_z z_i} - \sum_{i \in m,n+1} \frac{(y_i - y_{n+1})}{2} \mathbf{v}_i e^{-ik'_z z_i} \Bigg].
\end{aligned} \quad (A25)
$$

The term in [ ] is the (ion) velocity density, $\mathbf{V}_i$ for the particular k_z mode.

$$
\mathbf{D} = \sum_{m,n} e^{-ik'_\tau x_m} e^{-ik'_\nu y_n} \mathbf{V}_i(x_m, y_n, k'_z) \quad (A26)
$$

In vector notation,

$$\mathbf{D} = \sum_{m,n} e^{-ik'_\perp \mathbf{x}_g} \mathbf{V}_i(\mathbf{x}_g, k'_z) \qquad (A27)$$

Substitute Eq. (A24) and (A27) back into Eq. (A14).

$$\mathbf{\Lambda}(\mathbf{x}) = V\frac{m}{M} \sum_{\mathbf{k}} \sum_{\mathbf{k}''} S(\mathbf{k})S(-\mathbf{k}'')e^{i\mathbf{k}\cdot\mathbf{x}} \sum_g \left\{ \mathbf{E}(\mathbf{k}'') \left[\frac{m}{M}n_i(\mathbf{x}_{\perp g}, k'_z)\right] \right.$$
$$\left. + \frac{1}{c}\left[\frac{m}{M}\mathbf{V}_i(\mathbf{x}_{\perp g}, k'_z)\right] \times \mathbf{B}(\mathbf{k}'') \right\} e^{ik'_\perp \cdot \mathbf{x}_g} \qquad (A28)$$

Recall that $\mathbf{k}' \equiv \mathbf{k} - \mathbf{k}''$ and also note that $\sum_g F(\mathbf{x}_g)e^{-ik'_\perp \cdot \mathbf{x}_g} = V_2 F(\mathbf{k}'_\perp)$, where V_2 is the area of the two dimensional grid. Substitution yields,

$$\mathbf{\Lambda}(\mathbf{x}) = VV_2\frac{m}{M} \sum_{\mathbf{k}} \sum_{\mathbf{k}'} S(\mathbf{k})S(\mathbf{k}' - \mathbf{k})$$
$$\left\{ \mathbf{E}(\mathbf{k} - \mathbf{k}')n_i(\mathbf{k}') + \frac{1}{c}\mathbf{V}_i(\mathbf{k}') \times \mathbf{B}(\mathbf{k} - \mathbf{k}') \right\} e^{i\mathbf{k}\cdot\mathbf{x}}. \qquad (A29)$$

Note that $\Lambda(\mathbf{x}) = \sum_{\mathbf{k}} \Lambda(\mathbf{k})e^{i\mathbf{k}\cdot\mathbf{x}}$ so that we may rewrite Eq. (A29) as,

$$\mathbf{\Lambda}(\mathbf{k}) = VV_2\frac{m}{M} \sum_{\mathbf{k}} \sum_{\mathbf{k}'} S(\mathbf{k})S(\mathbf{k}' - \mathbf{k})$$
$$\left\{ \mathbf{E}(\mathbf{k} - \mathbf{k}')n_i(\mathbf{k}') + \frac{1}{c}\mathbf{V}_i(\mathbf{k}') \times \mathbf{B}(\mathbf{k} - \mathbf{k}') \right\}. \qquad (A30)$$

Look at the third term of Eq. (A9).

$$q_p \nabla \cdot \left[\sum_{j=1}^{N_0} \mathbf{v}_j \mathbf{v}_j S(\mathbf{x} - \mathbf{x}_j) - \sum_{i=1}^{N_0} \mathbf{v}_i \mathbf{v}_i S(\mathbf{x} - \mathbf{x}_i) \right]$$

Define $\mathbf{\Gamma}$,

$$\mathbf{\Gamma}(\mathbf{x}) \equiv \sum_{\alpha=1}^{2N_0} \epsilon \mathbf{v}_\alpha \mathbf{v}_\alpha S(\mathbf{x} - \mathbf{x}_\alpha), \qquad (A31)$$

where

$$\epsilon_\alpha = \begin{cases} +1, & \text{if } \alpha \le N_0; \\ -1, & \text{otherwise.} \end{cases}$$

Continue as before. Expand S in a two-dimensional Taylor series about the nearest grid point and truncate at the dipole term. Use centered finite differences for the derivatives. Split up S into separate grid and particle pieces,

$$S(r) = \frac{1}{\sqrt{2\pi}a}^3 exp(-\frac{1}{2}\frac{r^2}{a^2})$$
$$= \left[\frac{1}{\sqrt{2\pi}a}^2 exp(-\frac{1}{2}\frac{x^2+y^2}{a^2})\right]\left[\frac{1}{\sqrt{2\pi}a}exp(-\frac{1}{2}\frac{z^2}{a^2})\right]$$
$$= S_2 S_z. \qquad (A32)$$

This lets us write,

$$\mathbf{\Gamma(x)} = \sum_{m,n}\sum_{\alpha \in m,n} \epsilon \mathbf{v}_\alpha \mathbf{v}_\alpha \left[1 + (x_\alpha - x_m)\frac{\partial}{\partial x}\bigg|_m + (y_\alpha - y_n)\frac{\partial}{\partial y}\bigg|_n\right]$$
$$\cdot S_2(x - x_m, y - y_n)S_z(z - z_\alpha). \qquad (A33)$$

Shift indicies as before and Fourier expand,

$$S_z(z - z_\alpha) = \sum_{k_z} S_z(k_z)exp\{ik_z(z - z_\alpha)\}.$$

These actions yield

$$\mathbf{\Gamma} = \sum_{k_z} S_z(k_z)e^{ik_z z}\sum_{m,n} S_2(x - x_m, y - y_n) \cdot \left[\sum_{\alpha \in m,n}\epsilon \mathbf{v}_\alpha \mathbf{v}_\alpha e^{-ik_z z_\alpha}\right.$$
$$+ \sum_{\alpha \in m-1,n}\epsilon \mathbf{v}_\alpha \mathbf{v}_\alpha e^{-ik_z z_\alpha}\frac{(x_\alpha - x_{m-1})}{2\Delta} - \sum_{\alpha \in m+1,n}\epsilon \mathbf{v}_\alpha \mathbf{v}_\alpha e^{-ik_z z_\alpha}\frac{(x_\alpha - x_{m+1})}{2\Delta}$$
$$+ \sum_{\alpha \in m,n-1}\epsilon \mathbf{v}_\alpha \mathbf{v}_\alpha e^{-ik_z z_\alpha}\frac{(y_\alpha - y_{n-1})}{2\Delta} - \left.\sum_{\alpha \in m,n+1}\epsilon \mathbf{v}_\alpha \mathbf{v}_\alpha e^{-ik_z z_\alpha}\frac{(y_\alpha - y_{n+1})}{2\Delta}\right].$$

$$(A34)$$

The term in [ ] is (a modified) product of electron velocities minus the (modified) product of ion velocities at each grid point. Define

$$\Psi(m, n, k_z) \equiv \langle \mathbf{v}_\alpha \mathbf{v}_\alpha \rangle_e(m, n, k_z) - \langle \mathbf{v}_\alpha \mathbf{v}_\alpha \rangle_i(m, n, k_z),$$

where $\langle\ \rangle$ denotes the modified quantity averaged to the grid points for a given k_z. Using this definition, rewrite Eq. (A34) as

$$\mathbf{\Gamma}(x,y,z) = \sum_{k_z} S_z(k_z)e^{ik_z z}\sum_{m,n}S_2(x-x_m,y-y_n)\mathbf{\Psi}(m,n,k_z),\quad (A35)$$

or

$$\mathbf{\Gamma}(\mathbf{k}) = V_2 S(\mathbf{k})\mathbf{\Psi}(\mathbf{k}). \tag{A36}$$

Look at the first term of Eq. (A9). Define

$$\Theta \equiv \sum_{j=1}^{N_0} S(\mathbf{x}-\mathbf{x}_j)\int S(\mathbf{x}'-\mathbf{x}_j)\mathbf{E}_{\parallel}(\mathbf{x}')d\mathbf{x}'. \tag{A37}$$

The procedure is similar to that followed for the second term. Comparing to Eq. (A29) and (A30) leads us to

$$\Theta(\mathbf{x}) = V\ V_2\sum_{\mathbf{k}}\sum_{\mathbf{k}'}S(\mathbf{k})S(\mathbf{k}'-\mathbf{k})\left[\mathbf{E}_{\parallel}(\mathbf{k}-\mathbf{k}')n_e(\mathbf{k}')\right]e^{i\mathbf{k}\cdot\mathbf{x}}. \tag{A38}$$

or

$$\Theta(\mathbf{k}) = V\ V_2\sum_{\mathbf{k}'}S(\mathbf{k}'-\mathbf{k})\left[\mathbf{E}_{\parallel}(\mathbf{k}-\mathbf{k}')n_e(\mathbf{k}')\right]. \tag{A39}$$

Gather equations (A29), (A35), and (A38) and substitute back into Eq. (A9) to find the partical time derivative of the current,

$$\frac{\partial}{\partial t}\mathbf{J}(\mathbf{x}) = \frac{q_p^2}{m_p}V\ V_2\sum_{\mathbf{k}}\sum_{\mathbf{k}'}S(\mathbf{k})S(\mathbf{k}'-\mathbf{k})\left[\mathbf{E}_{\parallel}(\mathbf{k}-\mathbf{k}')n_e(\mathbf{k}')\right]e^{i\mathbf{k}\cdot\mathbf{x}}$$

$$+\frac{q_p^2}{m_p}\frac{m}{M}VV_2\frac{m}{M}\sum_{\mathbf{k}}\sum_{\mathbf{k}'}S(\mathbf{k})S(\mathbf{k}'-\mathbf{k})$$

$$\left\{\mathbf{E}(\mathbf{k}-\mathbf{k}')n_i(\mathbf{k}')+\frac{1}{c}\mathbf{V}_i(\mathbf{k}')\times\mathbf{B}(\mathbf{k}-\mathbf{k}')\right\}e^{i\mathbf{k}\cdot\mathbf{x}}$$

$$-iq_p\mathbf{k}V_2\sum_{k_z}S_z(k_z)e^{ik_z z}\sum_{m,n}S_2(x-x_m,y-y_n)\mathbf{\Psi}(m,n,k_z).\ (A40)$$

In Fourier space this may be represented more compactly as,

$$\frac{\partial}{\partial t}\mathbf{J}(\mathbf{k}) = \frac{q_p^2}{m_p} V\, V_2\, S(\mathbf{k}) \sum_{\mathbf{k}'} S(\mathbf{k}' - \mathbf{k}) \left[\mathbf{E}_{\parallel}(\mathbf{k} - \mathbf{k}') n_e(\mathbf{k}')\right]$$

$$+ \frac{q_p^2}{m_p} \frac{m}{M} V V_2 \frac{m}{M} S(\mathbf{k}) \sum_{\mathbf{k}'} S(\mathbf{k}' - \mathbf{k})$$

$$\left\{ \mathbf{E}(\mathbf{k} - \mathbf{k}') n_i(\mathbf{k}') + \frac{1}{c}\mathbf{V}_i(\mathbf{k}') \times \mathbf{B}(\mathbf{k} - \mathbf{k}') \right\}$$

$$- i q_p \mathbf{k} V_2 S(\mathbf{k}) \mathbf{\Psi}(\mathbf{k}). \tag{A41}$$

The motivation is to determine $\mathbf{E}_T$ from equation (A1). The implementation into a computer program is more efficient if we instead determine $\mathbf{F}_T$, the transverse electric force. The forces which correspond to the various field components are defined

$$\mathbf{F}_T(\mathbf{k}) = V S(\mathbf{k}) \mathbf{E}_T(\mathbf{k})$$

$$\mathbf{F}_{\parallel}(\mathbf{k}) = V S(\mathbf{k}) \mathbf{E}_{\parallel}(\mathbf{k})$$

$$\mathbf{F}_L(\mathbf{k}) = V S(\mathbf{k}) \mathbf{E}_L(\mathbf{k})$$

$$\mathbf{F}_E(\mathbf{k}) = \mathbf{F}_T(\mathbf{k}) + \mathbf{F}_L(\mathbf{k})$$

$$\mathbf{F}_B(\mathbf{k}) = V S(\mathbf{k}) \mathbf{B}(\mathbf{k}).$$

Using these definitions, using a Gaussian shape factor $V S(\mathbf{k}) = exp(-k^2 a^2)$, and noting that $V_2 V = L_z$ we have

$$k^2 c^2 \frac{n_o}{V_2} e^{k^2 a^2} \mathbf{F}_T(\mathbf{k})$$

$$\left\{ \sum_{\mathbf{k}'} \left[\mathbf{F}_{\parallel}(\mathbf{k} - \mathbf{k}') n_e(\mathbf{k}') + \frac{m}{M} \mathbf{F}_E(\mathbf{k} - \mathbf{k}') n_i(\mathbf{k}') \right] \right\}_T$$

$$= \left\{ -\frac{m}{M}\frac{1}{c} \sum_{\mathbf{k}'} \mathbf{V}_i(\mathbf{k}') \times \mathbf{F}_B(\mathbf{k} - \mathbf{k}') \right\}_T + i \left[\mathbf{k} \cdot \mathbf{\Psi}\right]_T \equiv \mathcal{S}_T(\mathbf{k}). \tag{A42}$$

The right hand side of Eq. (A42) consists of known quantities and is therefore a source term which we call $\mathcal{S}$. This source term is accumulated on the grid from the particle velocities. Eq. (A42) may be expressed in matrix form as

$$[\mathcal{L}][\mathbf{F}_T] = [\mathcal{S}]$$

which has the formal solution of

$$[\mathbf{F}_T] = [\mathcal{L}]^{-1}[\mathcal{S}].$$

This inversion of $\mathcal{L}$ is prohibitively expensive to perform at every time step for the dimensions of the simulation arrays involved here. An interative procedure is adopted instead to solve Eq. (A42). This limits the simulation model to fluctuations in the fields and densities to roughly twice the backround quantities. This technique involves the separation of the $\mathbf{k}' = 0$ terms from the summations involving $\mathbf{F}_T$ and transposing the $\mathbf{k}' \neq 0$ terms to the other side of the equation in Eq. (A42). As a first approximation, these $\mathbf{k}' \neq 0$ terms are set equal to zero. A solution for $\mathbf{F}_T$ is then obtained which is then reinserted into the $\mathbf{k}' \neq 0$ terms and $\mathbf{F}_T$ obtained again with this process iterated until convergence is sufficient. This methodology is similar to the renormalization procedures used to describe weak turbulence.

There are two terms on the left hand side of equation (A42) which involve a convolution with $\mathbf{F}_T$. Look first at the term with the ion number density dependence,

$$\sum_{\mathbf{k}'} \frac{m}{M} \{\mathbf{F}_E(\mathbf{k} - \mathbf{k}')n_i(\mathbf{k}')\}_T = \left\{ \frac{m}{M} n_0 \mathbf{F}_E(\mathbf{k}) \right. $$
$$\left. + \frac{m}{M} \sum_{\mathbf{k}' \neq 0} \mathbf{F}_E(\mathbf{k} - \mathbf{k}')n_i(\mathbf{k}') \right\}_T . \quad (A43)$$

The implementations of the convolutions over $\mathbf{k}' \neq 0$ are done by a hybrid method which uses two-dimensional Fourier transformations to an x-y representation for each k_z wavenumber. This reduces the $k_x - k_y$ convolutions

into matrix multiplies with the overhead left in the Fourier transforms. This is combined with a convolution which only concerns the k_z dependencies. The evaluation of the other term is more complicated due to the fact that the parallel component of the electric force contains contributions from both the transverse and longitudinal electric forces,

$$\mathbf{F}_{\parallel}(\mathbf{x}) = \hat{\mathbf{b}}(\mathbf{x}) \left[\hat{\mathbf{b}}(\mathbf{x}) \cdot \mathbf{F}_E(\mathbf{x}) \right], \qquad (A44)$$

which both must be used to perform the convolutions,

$$\sum_{\mathbf{k}'} \left\{ \mathbf{F}_{\parallel}(\mathbf{k} - \mathbf{k}') n_e(\mathbf{k}') \right\}_T = \left\{ n_0 \mathbf{F}_{\parallel}(\mathbf{k}) + \sum_{\mathbf{k}' \neq 0} \mathbf{F}_{\parallel}(\mathbf{k} - \mathbf{k}') n_e(\mathbf{k}') \right\}_T. \qquad (A45)$$

Pulling the longitudinal terms to the right hand side, denote a new "source" term, $\mathcal{S}' = \mathcal{S}+$ new longitudinal terms,

$$\left[k^2 c^2 \frac{n_o}{V_2} e^{k^2 a^2} + \frac{m}{M} \right] \mathbf{F}_T(\mathbf{k}) + n_0 \left[(\mathbf{F}_T)_{\parallel} \right]_T$$
$$= \mathcal{S}_T(\mathbf{k}) - n_0 \left[(\mathbf{F}_L)_{\parallel} \right]_T$$
$$\sum_{\mathbf{k}' \neq 0} \left[(\mathbf{F}_L)_{\parallel} (\mathbf{k} - \mathbf{k}') n_e(\mathbf{k}') \right]_T + \frac{m}{M} \sum_{\mathbf{k}' \neq 0} \left[\mathbf{F}_E(\mathbf{k} - \mathbf{k}') n_i(\mathbf{k}') \right]_T$$
$$\equiv \mathcal{S}'. \qquad (A46)$$

Next we examine Eq. (A46) for the case where $\mathbf{B}$ is in the y-z plane and makes a angle, θ, with respect to the z axis. For a small angle,

$$\mathbf{B} \simeq B \left(\hat{z} + \frac{x}{L_s} \hat{y} \right),$$

$$sin\theta \approx \theta \approx \frac{x}{L_s} \approx \frac{L_n}{L_s},$$

$$cos\theta \approx 1 - \frac{\theta^2}{2} \approx 1 - \frac{1}{2} \left(\frac{L_n}{L_s} \right)^2.$$

Neglect terms of order (L_n/L_s) and higher, assume incompressible, and note that $k_z \ll k_x, k_y$ for our simulation parameters. Thus, only the z component of the transverse electric force is solved for with the result,

$$\left[k^2 c^2 e^{k^2 a^2} n_0 + \frac{m}{M} n_0 + n_0 \right] \mathbf{F}_{Tz}(\mathbf{k}) = \mathcal{S}'_{Tz}(\mathbf{k})$$

$$- \left[\frac{m}{M} \sum_{\mathbf{k}' \neq 0} \mathbf{F}_E(\mathbf{k} - \mathbf{k}') n_i(\mathbf{k}) + \sum_{\mathbf{k}' \neq 0} (\mathbf{F}_L)_{\parallel} (\mathbf{k} - \mathbf{k}') n_e(\mathbf{k}') \right]_{Tz} (\mathbf{k}). \quad (A47)$$

Expansion of $\mathcal{S}'_{Tz}$ and using the aforementioned approximations yields the explicit form for the solution of $\mathbf{F}_{Tz}$,

$$\mathbf{F}_{Tz}(\mathbf{k}) = \left[k^2 c^2 e^{k^2 a^2} n_0 + \frac{m}{M} n_0 + n_0 \right]^{-1} \cdot$$

$$\left\{ \left(-\frac{m}{M} \frac{1}{c} \right) \left[\left(\frac{k_x^2 + k_y^2}{k^2} \right) \left(\sum_{\mathbf{k}'} v_{iz}(\mathbf{k}') F_{By}(\mathbf{k} - \mathbf{k}') - \right. \right. \right.$$

$$\sum_{\mathbf{k}'} v_{iy}(\mathbf{k}') F_{Bz}(\mathbf{k} - \mathbf{k}') \right)$$

$$+ \left(\frac{-k_z k_x}{k^2} \right) v_{iy}(\mathbf{k}) F_{Bz} + \left(\frac{-k_z k_y}{k^2} \right) v_{iz}(\mathbf{k}) F_{Bz} \right]$$

$$+ i \left[\left(k_z - \frac{k_z^3}{k^2} \right) \langle v_z v_z \rangle + \left(k_x - \frac{k_x^3}{k^2} \right) \langle v_x v_x \rangle + \left(k_y - \frac{k_y^3}{k^2} \right) \langle v_y v_y \rangle \right]$$

$$- n_0 \left(\cos^2\theta \, F_{Lz}(\mathbf{x}) + \sin\theta \cos\theta \, F_{Ly}(\mathbf{x}) \right) (\mathbf{k})$$

$$- \sum_{\mathbf{k}' \neq 0} \left(\frac{m}{M} n_i(\mathbf{k}') + n_e(\mathbf{k}') \right) F_{Lz}(\mathbf{k} - \mathbf{k}')$$

$$- \sum_{\mathbf{k}' \neq 0} \left(\frac{m}{M} n_i(\mathbf{k}') + n_e(\mathbf{k}') \right) F_{Tz}(\mathbf{k} - \mathbf{k}') \right\}. \quad (A48)$$

The simulation code solves Eq. (A48) for the z component of the transverse electric force. The terms on the right hand side involving the transverse electric force are set to zero for the initial solution. The iterated solution is replaced into the right hand side until convergence.

REFERENCES

1. A.S. Bishop, Project Sherwood:The U.S. Program in Controlled Fusion, Addison-Wesley, Reading, Mass., 1958.

2. R.B. White, Reviews of Modern Physics, **58**, 183 (1986).

3. G. Van Hoven and M.A. Cross, Phys. Rev. **A7**, 1347 (1973).

4. J.U. Brackbill, Methods in Computational Physics, **6** 1 (1976).

5. A.A. Galeev and R.Z. Sagdeev, "Nonlinear Plasma Theory" in Reviews of Plasma Physics **7** Consultants Bureau Enterprizes, Inc. New York (1979).

6. J.M. Dawson, Rev. Mod. Phys. **55**, 403 (1983).

7. H. Alfvén, *Cosmical Electrodynamics*, (Clarendon Press, Oxford, 1950).

8. W.W. Lee and H Okuda, J. Comp. Phys. **26**, 139 (1978).

9. C.G. Darwin, Phil. Mag. **39**, 537 (1920).

10. C.W. Nielson and H.R. Lewis, in *Methods in Computational Physics*, Vol. 16, (J. Killeen, Ed., Academic Press, New York, 1976).

11. J. Busnardo-Neto, P.L. Pritchett, A.T. Lin, and J.M. Dawson, J. Comp. Phys. **23**, 300 (1977).

12. C.Z. Cheng and H. Okuda, J. Comp. Phys. **25**, 133 (1977).

13. J.L. Geary, et. al., to be published.

14. R. Howard and Z. Svestka, Solar Phys. **54**, 65 (1977).

15. P.A. Sweet, Proc. AAS-NASA Symp. on the physics of solar flares, NASA SP-50, p.409 National Aeronautics and Space Administration, Washington, D.C.

16. J.W. Dungey,Proc. AAS-NASA Symp. on the physics of solar flares, NASA SP-50, p.415 National Aeronautics and Space

Administration, Washington, D.C.

17 S.T. Wu, 1985, private communication.

18. G.I. Dimov, V.V. Zakaidakov, and M.E. Kishinevskii, Sov. J. Plasma Phys., **2**, 326 (1976).

19 T.K. Fowler and B.G. Logan, Comments Plasma Physics Controlled Fus. Res. **II**, 167 (1977).

20. Ch.P. Ritz, Roger D. Bengtson, S.J. Levenson and E.J. Powers, Phys. Fluids **27**, 2956 (1984).

21. R.W. Hockney and J.W. Eastwood, *Computer Simulation Using Particles* (McGraw-Hill, Inc., 1981).

22. C.K. Birdsall and A.B. Langdon, *Plasma Physics Via Plasma Simulation* (McGraw-Hill, Inc., 1985).

23. O. Buneman, J. Comp. Phys. **12**, 124 (1973).

24. C.G. Darwin, Phil. Mag. **39**, 537 (1920).

25. L. Landau and E. Lifshitz, *Statistical Physics"* *Part 1* (Pergamon Press, Elmsford, New York, USA, 1980) 3rd Ed.

26. N. Wiener, Acta Mathematica **55**, 117 (1930).

27. R.B. Blackman and J.W. Tukey, *The Measurement of Power Spectra From the Point of View of Communications Engineering* (Dover, 1959).

28. E. Parzen, Technometrics **3**, 167 (1961).

29. S. Ichimaru, *Basic Principles of Plasma Physics*, (W.A. Benjamin, Inc., Reading, Massachusetts, 1973).

30. T. Kamimura, T. Wagner and J.M. Dawson, Phys. Fluid **21**, 1151 (1978).

31. A.B. Langdon and C.K. Birdsall, Phys. Fluids **13**, 2115 (1970).

32. H.P. Furth, J. Killeen, and M.N. Rosenbluth, Phys. Fluids **6**

459 (1963).

33. J. M. Finn and P. K. Kaw, Phys. Fluids **20**,72 (1977).

34. P. L. Pritchett and C. C. Wu, Phys. Fluids **22**, 2140 (1979).

35. T. Tajima and J.-I.Sakai, Institute for Fusion Studies report IFSR #197 (1985).

36. B. Coppi, et al., Sov. J. Plasma Phys. **2**,533 (1976).

37. O.P. Pogutse and E.I. Yurchenko, Sov. J. Plasma Phys. **3**, 283 (1977).

38. M.N. Rosenbluth, et al., Phys. Fluids **19**,1987 (1976).

39. J.L. Johnson, C. R. Oberman, R. M. Kulsrud, and E. A. Friedman, UN Geneva Conf. *31*, 198(1958).

40. V.D. Shafranov, Sov. Phys.- Tech. Phys., **15**,175 (1970).

41. J.F. Drake and Y.C. Lee, Phys. Fluids, **20**, 1341 (1977).

42. I. Katanuma and T. Kamimura, Phys. Fluids **23**, 2500 (1980).

43. A.T. Lin, J.M. Dawson, and H. Okuda, Phys. Fluids, **17**, 1995 (1974).

44. A.B. Langdon and B. Lasinski, in *Methods of Computational Physics* (Academic), 327 (1976).

45. D.C. Barnes, T. Kamimura, J.-N. Leboeuf, E. Montalvo, T. Tajima and E. Zaidman, Eleventh International Conference on Numerical Simulation of Plasmas, Montreal (1985).

46. E. Montalvo, E. Zaidman, T. Tajima, and D.C. Barnes, Bull. Am. Phys. Soc. **29**, 1295 (1984).

47. Fadeev, V. M., Kvartskawa, I.F. and Komarov, N. N., Nucl. Fusion **5**,202 (1965).

48. Gwo-Liang Chen, University of Texas at Austin Report FRCR #240, (1981).

49. H.L. Berk, M.N. Rosenbluth, H.V. Wong, T.M. Antonsen, and D.E. Baldwin, Sov. J. Plasma Phys., **9**, 108 (1983).

50. J.A. Byers, Phys. Fluids **29**, 1547 (1986).

51. T. Tajima, J. Sakai, H. Nakajima, T. Kosugi, F. Brunel, E. Zaidman, L. Vlahos, and M.R. Kundu, Astrophysical Jounal to be published, (1986).

52. E.G. Zweibel and A.H. Boozer, Astrophysical Journal, **295** 642 ,(1985).

53. G.I. Dimov, V.V. Zakaidakov, and M.E. Kishinevshii, Sov. J. Plasma Phys. **2**, 326 (1976).

54. R. Steinolfson and T. Tajima, to be publishd; and T. Tajima, R. Steinolfson, D.C. Barnes, Z. Mikic, and D. Schnack, Bull. Amer. Astrophysical Soc. **18**, 676 (1986).

55. H. Strauss and G. VanHoven, Phys. Fluids, **27**, 2063, (1984).

VITA

Ernest Gary Zaidman was born on November 15, 1954, in Tampa, Florida, the son of Abraham Zaidman and Rose Zaidman. After completing his high school education at Henry B. Plant High School in Tampa, Florida, he entered the University of South Florida in the Fall of 1972. In May, 1975, he received the degree of Bachelor of Science in Physics and in May, 1979, he received the degree of Master of Arts in Physics. On August 7, 1977 he was married to Wendy Carol Bernstein. In September, 1978, he entered The University of Texas at Austin and has been employed as research assistant in the intervals from September, 1978 to July, 1980, and from January, 1982 to the present time. From July, 1980 to December, 1981 he was employed as a research scientist by Zycor, Inc.

Permanent Address: 307 Willet Drive

Buda, Texas 78610

This disseration was typed by Ernest G. Zaidman.